

A MEASUREMENT OF THE MASS OF THE W VECTOR BOSON
FROM $\bar{p}p \rightarrow W^\pm \rightarrow \mu^\pm \nu_\mu$ AT $\sqrt{s} = 1.8$ TEV

BY

RANDY MICHAEL KEUP

B.S., University of Wisconsin – Oshkosh, 1987
M.S., University of Illinois at Urbana-Champaign, 1988

THESIS

Submitted in partial fulfillment of the requirements
for the degree of Doctor of Philosophy in Physics
in the Graduate College of the
University of Illinois at Urbana-Champaign, 1995

Urbana, Illinois

A MEASUREMENT OF THE MASS OF THE W VECTOR BOSON
FROM $\bar{p}p \rightarrow W^\pm \rightarrow \mu^\pm \nu_\mu$ AT $\sqrt{s} = 1.8$ TEV

Randy Michael Keup, Ph.D.
Department of Physics
University of Illinois at Urbana-Champaign, 1995
Professor Tony Liss, advisor

This thesis presents a measurement of the mass of the W boson using data collected during the 1992-93 collider run at the Fermilab Tevatron with the CDF detector. A fit to the transverse mass spectrum of a sample of 3268 $W \rightarrow \mu\nu$ events from 19.7 pb^{-1} of data yields a mass of $M_W^\mu = 80.310 \pm 0.205$ (stat.) ± 0.120 (syst.) ± 0.050 (scale). This result is compared to previous measurements and current predictions.

Acknowledgements

I start by thanking all those involved in my graduate career. Thanks to my undergraduate professors and to the Illinois physics department for accepting me all those many years ago and giving me a fellowship in an attempt to convince me that physics is where the money is.

Thanks to Lee for taking me on board CDF and overseeing the whole ball o' wax here at Illinois. A special thanks to Tony for guiding my research and for trying his best to kick me out of the proverbial nest. I am glad to have had him as my advisor all these years.

To Dave and Jerry for assembling (and maintaining) the *finest* VMS cluster in the world. To Tom, Shirley, and Sue for managing the corporate arm of high-energy physics and for providing travel and sleeping accommodations whenever the need arose. To the engineering and technical division for all their work on the upgrade, and to Fred for showing me a few of the ins and outs of machining, not to mention making all manner of gadgets and removing my bumper. To Alain and all the techs and undergrads who helped build the muon upgrade, and especially to those of the lunch-time card crowd.

Thanks also to all my former comrades in arms at Illinois. To Dave, Tom, Phil, Vic, Peter, and Hovhannes for introducing me to the high-energy lifestyle and for showing me that CDF is just a front for the party industry. On that note, thanks also to the CDF band, both past and present for the countless nights of eardrum-breaking noise; and the precursor to that, Sunday afternoons in IIEPL with Andrew, Jeremy, and Dave. Speaking of diversions, there's the CDF Basketball Association: the only game

where you're penalized for committing *less* than 5 fouls. Oh, and not to forget the CDF golf outings. To Steve and Dee for feeding me from time to time and actually throwing me a birthday party.

Thanks to all those who helped in the analysis: Larry, Henry, Sarah, Aseet, Kevin, Steve, and especially David and Young-kcc. No analysis is complete without a Korean dinner.

Thanks to Tom, and recently Rob, for taking over pager duty and not complaining too loudly. Thanks to Mark, my fellow hoopster and upgrade compatriot, good luck teaching. And of course I can't leave out Andrew, who joined me in HEPL on many a weekend as we struggled to get the first drift chambers out the door; not to mention late nights in the pit, spelunking under the yokes, oscillating preamps, and on and on. It's been a fun seven years.

To Ray, Jim, and Rose for all the times at Trito's, for the cookouts, and for all the late night discussions about total nonsense. To Ray and Renée, for all the fun times and the opportunities to forget about physics for a bit. Then there's New Year's in Wisconsin with Dave, John, Sharon, Cheryl, Dan, Mike, Marsha, etc... thanks for the memories.

To my family, for their love and support and for encouraging my education; for never once saying "Physics?!?! Why would you want to do that?", and for trying to understand what exactly it is that I do. And to Hollie for blazing the trail ahead of me.

And last, but definitely not least, my loving soul mate Eva, who, knowing full well what she was getting into, still thought it worthwhile to marry me. Thank you so much for *distracting* me and showing me the subtleties of life.

I'm sure I've left out someone, but you know who you are.

This research was supported in part by the United States Department of Energy under contracts DE-AC02-76ER-01195 and DE-FG02-91ER-40677 and by the Alfred P. Sloan foundation.

CDF Collaboration for the 1992-1993 Run

F. Abe,¹³ M. G. Albrow,⁷ D. Amidei,¹⁶ J. Antos,²⁸ C. Anway-Wiese,⁴ G. Apollinari,²⁶ H. Areti,⁷
 M. Atac,⁷ P. Auchincloss,²⁵ F. Azfar,²¹ P. Azzi,²⁰ N. Bacchetta,¹⁸ W. Badgett,¹⁶ M. W. Bailey,¹⁸
 J. Bao,³⁴ P. de Barbaro,²⁵ A. Barbaro-Galtieri,¹⁴ V. E. Barnes,²⁴ B. A. Barnett,¹² P. Bartalini,²³
 G. Bauer,¹⁵ T. Baumann,⁹ F. Bedeschi,²³ S. Belreids,³ S. Belforte,²³ G. Bellettini,²³ J. Bellinger,³³
 D. Benjamin,³² J. Benlloch,¹⁵ J. Bensingler,³ D. Benton,²¹ A. Beretvas,⁷ J. P. Berge,⁷ S. Bertolucci,⁸
 A. Bhatti,²⁶ K. Biery,¹¹ M. Binkley,⁷ F. Bird,²⁹ D. Bisello,²⁰ R. E. Blair,¹ C. Blocker,²⁹ A. Bodek,²⁵
 W. Bokhari,¹⁵ V. Bolognisi,²³ D. Bortoletto,²⁴ C. Boswell,¹² T. Boulos,¹⁴ G. Brandenburg,⁹
 C. Bromberg,¹⁷ E. Buckley-Geer,⁷ H. S. Budd,²⁵ K. Burkett,¹⁶ G. Busetto,²⁰ A. Byon-Wagner,⁷
 K. L. Byrum,¹ J. Cammerata,¹² C. Campagnari,⁷ M. Campbell,¹⁶ A. Caner,⁷ W. Carithers,¹⁴
 D. Carlsmith,³³ A. Castro,²⁰ Y. Cen,²¹ F. Cervelli,²³ H. Y. Chao,²⁸ J. Chapman,¹⁶ M.-T. Cheng,²⁸
 G. Chiarelli,⁸ T. Chikamatsu,³¹ C. N. Chiou,²⁸ S. Cihangir,⁷ A. G. Clark,²³ M. Cobal,²³
 M. Contreras,⁵ J. Conway,²⁷ J. Cooper,⁷ M. Cordelli,⁸ D. Crane,¹ J. D. Cunningham,³ T. Daniels,¹⁵
 F. DeJongh,⁷ S. Delchamps,⁷ S. Dell'Agnello,²³ M. Dell'Orso,²³ L. Demortier,²⁶ B. Denby,²³
 M. Deninno,² P. F. Derwent,¹⁶ T. Devlin,²⁷ M. Dickson,²⁵ S. Donati,²³ R. B. Drucker,¹⁴ A. Dunn,¹⁶
 K. Einsweiler,¹⁴ J. E. Elias,⁷ R. Ely,¹⁴ E. Engels, Jr.,²² S. Eno,⁵ D. Errede,¹⁰ S. Errede,¹⁰ Q. Fan,²⁵
 B. Farhat,¹⁵ I. Fiori,² B. Flaughner,⁷ G. W. Foster,⁷ M. Franklin,⁹ M. Frautschi,¹⁸ J. Freeman,⁷
 J. Friedman,¹⁵ H. Frisch,⁵ A. Fry,²⁹ T. A. Fuess,¹ Y. Fukui,¹³ S. Funaki,³¹ G. Gagliardi,²³
 S. Galeotti,²³ M. Gallinaro,²⁰ A. F. Garfinkel,²⁴ S. Geer,⁷ D. W. Gerdes,¹⁶ P. Giannetti,²³
 N. Giokaris,²⁶ P. Giromini,⁸ L. Gladuey,²¹ D. Glenzinski,¹² M. Gold,¹⁸ J. Gonzalez,²¹ A. Gordon,⁹
 A. T. Goshaw,⁶ K. Goulianos,²⁶ H. Grassmann,⁶ A. Grewal,²¹ G. Gricco,²³ L. Groer,²⁷
 C. Grosso-Pilcher,⁵ C. Haber,¹⁴ S. R. Hahn,⁷ R. Hamilton,⁹ R. Handler,³³ R. M. Hans,³⁴ K. Hara,³¹
 B. Haral,²¹ R. M. Harris,⁷ S. A. Hauger,⁶ J. Hauser,⁴ C. Hawke,²⁷ J. Heinrich,²¹
 D. Cronin-Hennessy,⁶ R. Hollebeek,²¹ L. Holloway,¹⁰ A. Holscher,¹¹ S. Hong,¹⁶ G. Honk,²¹ P. Hu,²²
 B. T. Huffman,²² R. Hughes,²⁵ P. Hurst,⁹ J. Huston,¹⁷ J. Huth,⁹ J. Hylen,⁷ M. Incagli,²³
 J. Incandela,⁷ H. Iso,³¹ H. Jensen,⁷ C. P. Jessop,⁹ U. Joshi,⁷ R. W. Kadel,¹⁴ E. Kajfasz,^{7a}
 T. Kamon,³⁰ T. Kaneko,³¹ D. A. Kardelis,¹⁰ H. Kasha,³⁴ Y. Kato,¹⁹ L. Keeble,³⁰ R. D. Kennedy,²⁷
 R. Kephart,⁷ P. Kesten,¹⁴ D. Kestenbaum,⁹ R. M. Keup,¹⁰ H. Keutelian,⁷ F. Keyvan,⁴ D. H. Kim,⁷
 H. S. Kim,¹¹ S. B. Kim,¹⁶ S. H. Kim,³¹ Y. K. Kim,¹⁴ L. Kirsch,³ P. Koehn,²⁵ K. Kondo,³¹
 J. Konigsberg,⁹ S. Kopp,⁵ K. Kordas,¹¹ W. Koska,⁷ E. Kovacs,^{7a} W. Kowald,⁶ M. Krasberg,¹⁶
 J. Kroll,⁷ M. Kruse,²⁴ S. E. Kuhlmann,¹ E. Kuns,²⁷ A. T. Laasanen,²⁴ N. Labanca,²³ S. Lammel,⁴
 J. I. Lamoureux,³ F. LeCompte,¹⁰ S. Leone,²³ J. D. Lewis,⁷ P. Limon,⁷ M. Lindgren,⁴ P. M. Liss,¹⁰
 N. Lockyer,²¹ C. Loomis,²⁷ O. Long,²¹ M. Loreti,²⁰ E. H. Low,²¹ J. Lu,³⁰ D. Lucchesi,²³
 C. B. Luchini,¹⁰ P. Lukens,⁷ P. Maas,³³ K. Maeshima,⁷ A. Maghakian,²⁶ P. Maksimovic,¹⁵
 M. Mangano,²³ J. Mansour,¹⁷ M. Mariotti,²³ J. P. Marriner,⁷ A. Martin,¹⁰ J. A. J. Matthews,¹⁸
 R. Mattingly,¹⁵ P. McIntyre,³⁰ P. Melese,²⁶ A. Menzione,²³ E. Meschi,²³ G. Michail,⁹ S. Mikamo,¹³
 M. Miller,⁵ R. Miller,¹⁷ T. Mimashi,³¹ S. Miscetti,⁸ M. Mishina,¹³ H. Mitsushio,³¹ S. Miyashita,³¹
 Y. Morita,¹³ S. Moulding,²⁶ J. Mueller,²⁷ A. Mukherjee,⁷ T. Muller,⁴ P. Musgrave,¹¹ L. F. Naka,²⁹
 I. Nakano,³¹ C. Nelson,⁷ D. Neuberger,⁴ C. Newman-Holmes,⁷ L. Nodulman,¹ S. Ogawa,³¹
 S. H. Oh,⁶ K. E. Ohl,³⁴ R. Oishi,³¹ T. Okusawa,¹⁹ C. Pagliarone,²³ R. Paoletti,²³
 V. Papadimitriou,⁷ S. Park,⁷ J. Patrick,⁷ G. Pauletta,²³ M. Paulini,¹⁴ L. Pescara,²⁰ M. D. Peters,¹⁴
 T. J. Phillips,⁶ G. Piacentino,² M. Pillai,²⁵ R. Plunkett,⁷ L. Pondrom,³³ N. Produit,¹⁴
 J. Proudfoot,¹ F. Ptohos,⁹ G. Punzi,²³ K. Ragan,¹¹ F. Rimondi,² L. Ristori,²³ M. Roach-Bellino,³²
 W. J. Robertson,⁶ T. Rodrigo,⁷ J. Romano,⁵ L. Rosenson,¹⁵ W. K. Sakumoto,²⁵ D. Saltzberg,⁵
 A. Sansoni,⁸ V. Scarpine,³⁰ A. Schindler,¹⁴ P. Schlabach,⁹ E. F. Schmidt,⁷ M. P. Schmidt,³¹
 O. Schneider,¹⁴ G. F. Sciacca,²³ A. Scribano,²³ S. Segler,⁷ S. Seidel,¹⁸ Y. Seiya,³¹ G. Sganos,¹¹
 A. Sgolacchia,² M. Shapiro,¹⁴ N. M. Shaw,²⁴ Q. Shen,²⁴ P. F. Shepard,²² M. Shimojima,³¹
 M. Shochet,⁵ J. Siegrist,²⁹ A. Sill,^{7a} P. Sinervo,¹¹ P. Singh,²² J. Skarha,¹² K. Sliwa,³² D. A. Smith,²³

F. D. Snider,¹² L. Song,⁷ T. Song,¹⁶ J. Spalding,⁷ L. Spiegel,⁷ P. Sphicas,¹⁵ A. Spies,¹² L. Stanco,²⁰ J. Steele,³³ A. Stefanini,²³ K. Strahl,¹¹ J. Strait,⁷ D. Stuart,⁷ G. Sullivan,⁵ K. Sumorok,¹⁵ R. L. Swartz, Jr.,¹⁰ T. Takahashi,¹⁹ K. Takikawa,³¹ F. Tartarelli,²³ W. Taylor,¹¹ P. K. Teng,²⁸ Y. Teramoto,¹⁹ S. Tether,¹⁵ D. Theriot,⁷ J. Thomas,²⁹ T. L. Thomas,¹⁸ R. Thun,¹⁶ M. Timko,³² P. Tipton,²⁵ A. Titov,²⁶ S. Tkaczyk,⁷ K. Tollefson,²⁵ A. Tollestrup,⁷ J. Tonnison,²⁴ J. F. de Troconiz,⁹ J. Tseng,¹² M. Turcotte,²⁹ N. Turini,² N. Uemura,³¹ F. Ukegawa,²¹ G. Unal,²¹ S. van den Brink,²² S. Vejckik, III,¹⁶ R. Vidal,⁷ M. Vondracek,¹⁰ R. G. Wagner,¹ R. L. Wagner,⁷ N. Wainer,⁷ R. C. Walker,²⁵ C. H. Wang,²⁸ G. Wang,²³ J. Wang,⁵ M. J. Wang,²⁸ Q. F. Wang,²⁶ A. Warburton,¹¹ G. Watts,²⁵ T. Watts,²⁷ R. Webb,³⁰ C. Wendt,³³ H. Wenzel,¹⁴ W. C. Wester, III,¹⁴ T. Westhusing,¹⁰ A. B. Wicklund,¹ E. Wicklund,⁷ R. Wilkinson,²¹ H. H. Williams,²¹ P. Wilson,⁵ B. L. Winer,²⁵ J. Wolinski,³⁰ D. Y. Wu,¹⁶ X. Wu,²³ J. Wyss,²⁰ A. Yagil,⁷ W. Yao,¹⁴ K. Yasuoka,³¹ Y. Ye,¹¹ G. P. Yeh,⁷ P. Yeh,²⁸ M. Yin,⁶ J. Yoh,⁷ T. Yoshida,¹⁹ D. Yovanovitch,⁷ I. Yu,³⁴ J. C. Yun,⁷ A. Zanetti,²³ F. Zetti,²³ L. Zhang,³³ S. Zhang,¹⁶ W. Zhang,²¹ and S. Zucchelli²

^a Visitor

- ¹ Argonne National Laboratory, Argonne, Illinois 60439
- ² Istituto Nazionale di Fisica Nucleare, University of Bologna, I-40126 Bologna, Italy
- ³ Brandeis University, Waltham, Massachusetts 02254
- ⁴ University of California at Los Angeles, Los Angeles, California 90024
- ⁵ University of Chicago, Chicago, Illinois 60637
- ⁶ Duke University, Durham, North Carolina 27708
- ⁷ Fermi National Accelerator Laboratory, Batavia, Illinois 66516
- ⁸ Laboratori Nazionali di Frascati, Istituto Nazionale di Fisica Nucleare, I-00044 Frascati, Italy
- ⁹ Harvard University, Cambridge, Massachusetts 02138
- ¹⁰ University of Illinois, Urbana, Illinois 61801
- ¹¹ Institute of Particle Physics, McGill University, Montreal H3A 2T8, and University of Toronto, Toronto M5S 1A7, Canada
- ¹² The Johns Hopkins University, Baltimore, Maryland 21218
- ¹³ National Laboratory for High Energy Physics (KEK), Tsukuba, Ibaraki 305, Japan
- ¹⁴ Lawrence Berkeley Laboratory, Berkeley, California 94720
- ¹⁵ Massachusetts Institute of Technology, Cambridge, Massachusetts 02139
- ¹⁶ University of Michigan, Ann Arbor, Michigan 48109
- ¹⁷ Michigan State University, East Lansing, Michigan 48824
- ¹⁸ University of New Mexico, Albuquerque, New Mexico 87131
- ¹⁹ Osaka City University, Osaka 588, Japan
- ²⁰ Università di Padova, Istituto Nazionale di Fisica Nucleare, Sezione di Padova, I-35131 Padova, Italy
- ²¹ University of Pennsylvania, Philadelphia, Pennsylvania 19104
- ²² University of Pittsburgh, Pittsburgh, Pennsylvania 15260
- ²³ Istituto Nazionale di Fisica Nucleare, University and Scuola Normale Superiore of Pisa, I-56100 Pisa, Italy
- ²⁴ Purdue University, West Lafayette, Indiana 47907
- ²⁵ University of Rochester, Rochester, New York 14627
- ²⁶ Rockefeller University, New York, New York 10021
- ²⁷ Rutgers University, Piscataway, New Jersey 08854

- ²⁸ *Academia Sinica, Taiwan 11529, Republic of China*
- ²⁹ *Superconducting Super Collider Laboratory, Dallas, Texas 75237*
- ³⁰ *Texas A&M University, College Station, Texas 77843*
- ³¹ *University of Tsukuba, Tsukuba, Ibaraki 305, Japan*
- ³² *Tufts University, Medford, Massachusetts 02155*
- ³³ *University of Wisconsin, Madison, Wisconsin 53706*
- ³⁴ *Yale University, New Haven, Connecticut 06511*

Table of Contents

List of Tables	xi
List of Figures	xiv
1 Introduction	1
1.1 Historical Perspective	1
1.2 Experimental Observations	2
1.3 Precision Tests	4
1.4 Overview	5
2 Theory	7
2.1 Lowest Order Cross Section	7
2.2 W Mass Extraction	12
3 The CDF Detector	15
3.1 Overview	15
3.2 Tracking Chambers	17
3.3 Calorimeters	17
3.3.1 Central Electron Detection	18
3.4 Central Muon Detector	19
3.4.1 Central Muon Chambers	20
3.4.2 Central Muon Upgrade	23
3.4.3 Center Muon Extension	23
4 Data Sample	24
4.1 Data Acquisition	24
4.2 Muon Trigger	25
4.3 Muon Identification	27
4.4 Neutrino Identification	31
4.5 W Mass Sample	31
4.6 Calibration Samples	34

5	Momentum Measurement	37
5.1	CTC Track Reconstruction	37
5.2	CTC Calibration and Alignment	39
5.2.1	CTC Calibration	39
5.2.2	CTC Alignment	39
5.3	Absolute Momentum Scale	50
5.3.1	Determination of J/ψ Mass	50
5.3.2	Checks of the Momentum Scale	62
5.4	Momentum Resolution	63
5.5	Summary	66
6	Recoil Measurement	67
6.1	W Recoil Detection	67
6.2	Recoil Measurement Errors	68
6.3	W Recoil Calibration	70
6.4	Summary	73
7	Monte Carlo Simulation	74
7.1	Event Generation	74
7.1.1	Leading-order Production and Decay	74
7.1.2	W Transverse Momentum	75
7.2	Detector Simulation	77
7.2.1	Trigger Simulation	77
7.2.2	Momentum Resolution	78
7.2.3	Recoil Simulation	79
7.3	Comparison of Simulation and Data	81
7.4	Summary	85
8	Backgrounds and Radiative Corrections	86
8.1	Backgrounds	86
8.2	Radiative Corrections	91
8.3	Summary	95
9	W Mass Fit	96
9.1	Fitting Algorithm	96
9.2	Tests of the Method	100
9.3	Fitting the Data	100
9.4	Corrections	105
9.5	Checks of the Fitting Method	106
9.6	Summary	111

10 W Mass Uncertainties	113
10.1 Itemization of Uncertainties	113
10.2 Summary	124
11 Conclusion	125
11.1 Results	125
11.2 Future Prospects	128
Appendix	131
A Construction and Testing of the CMP	131
A.1 Principle of Operation	132
A.2 Design	132
A.3 Electronics	137
A.4 Chamber Construction	137
A.5 Testing and Performance	141
B Extrapolation from $M_{J/\psi}$ to M_W	147
B.1 Curvature Error	147
B.2 Curvature Expansion	149
Bibliography	152
Vita	159

List of Tables

1.1	Some previously published W mass measurements. Not all of the above measurements are independent. The mode is the decay channel of the W used in the measurement.	3
3.1	Summary of calorimeter energy resolutions. PEM and PIIA are the endcap calorimeters and FEM and FIIA are the forward/backward calorimeters. The symbol \oplus signifies that the constant term is added in quadrature in the resolution.	19
4.1	Criteria used to select the $W \rightarrow \mu\nu$ sample.	31
4.2	Criteria used to select the $Z \rightarrow \mu\mu$ sample.	36
5.1	Systematic uncertainties on the measurement of the J/ψ mass, used to set the momentum scale for muons from W decays. The tabulation includes the uncertainty incurred when extrapolating from tracks associated with J/ψ decays to those associated with W decays.	52
5.2	Measured masses of the Υ and Z resonances compared to the published values. The first uncertainty on the corrected value is from statistics. The second is the uncertainty from the momentum scale. The systematic uncertainties were not determined except for the Z where the systematic uncertainty is 50 MeV/ c^2 (see Section 5.4).	63
5.3	Summary of uncertainties in measuring the Z mass.	65
6.1	Summary of systematic uncertainties on $\langle u_{\parallel} \rangle$ and M_W incurred from the identification and removal of the muon.	70
7.1	Variation of the mean and RMS deviations of u_{\parallel} and u_{\perp} with the p_T^W scale factor, r . The nominal value of r corresponds to the intersection of $\text{RMS}(u_{\perp})$ from the data and $\text{RMS}(u_{\perp})$ from the simulation. The uncertainty corresponds to the point when the difference between data and simulation equals the uncertainty on $\text{RMS}(u_{\perp})$ from the data (0.1 GeV).	76

7.2	Variation of the means and RMS deviations of u_{\parallel} and u_{\perp} with the maximum allowed $ \vec{u} $ for data and simulation. The uncertainties are statistical only.	85
8.1	Summary of backgrounds. The number of events are for the signal region of $65 < M_T < 100$. The separate totals are for backgrounds that are included in the simulation ($W \rightarrow \tau\nu$ and $Z \rightarrow \mu\mu$) and for backgrounds that are applied as a post-fit correction to the W mass (all others). . .	91
9.1	Corrections to the fitted W mass due to the effects of radiative decays. The last entry is the unconstrained fit to both M_W and Γ_W	106
9.2	Variation of the fitted mass as the lower edge of the M_T fitting region is changed. The mass shifts are relative to M_W^{FIT} . The uncertainty is an estimate of the statistical independence between the fitted mass and M_W^{FIT}	107
9.3	Variation of the fitted mass as the upper edge of the M_T fitting region is changed. The mass shifts are relative to M_W^{FIT} . The uncertainty is an estimate of the statistical independence between the fitted mass and M_W^{FIT}	107
9.4	Shifts in M_W^{FIT} as the fit type is changed from the transverse mass spectrum to a fit using p_T^{μ} or p_T^{ν} . The uncertainties reflect the independent statistical uncertainty between these fits and the M_T fit.	108
9.5	Shifts in the fitted W mass as the selection cuts are changed from the nominal ($ \vec{u} < 20$ GeV) to ones covering a different subset of $ \vec{u} $. The shifts are assigned an uncertainty due to the independent statistical uncertainty. The shifts for the two subsets are expected to be almost completely anti-correlated.	108
10.1	Summary of systematic uncertainties in the W mass measurement in the muon channel. All uncertainties are rounded to the nearest 5 MeV/ c^2 . The uncertainties are added in quadrature to obtain the totals. The last column indicates which uncertainties are common to the electron channel analysis.	114
10.2	Variation in the W mass and width as the momentum resolution (see Equation 5.8) is varied from the nominal value by one and two standard deviations. The change in the W width is for the simultaneous fit to both mass and width.	115
10.3	Variation of the RMS of u_{\parallel} and u_{\perp} and the fitted mass and width shifts with the scale factor, r . The mass shift is for the fixed-width fit. The width shift is for a simultaneous fit to both the mass and width.	116

10.4	Dependence of the W charge asymmetry and the W mass on the PDF [40] choice. The Monte Carlo statistical uncertainty is ~ 15 MeV/ c^2 . MRS D' is the default choice of the current analysis. MRS B is the default choice of the previously published CDF W mass measurement [9]. . . .	119
10.5	Variation in the fitted W mass as the W width is constrained to other than the nominal value. The entries correspond to the ~ 2.5 and ~ 5.0 standard deviation points in Γ_W	121
10.6	Summary of backgrounds. The number of events are for the signal region of $65 < M_T < 100$. The separate totals are for backgrounds that are included in the simulation ($W \rightarrow \tau\nu$ and $Z \rightarrow \mu\mu$) and for backgrounds that are applied as a post-fit correction to the W mass (all others). . .	123
B.1	Table of curvature error terms and their contributions the error on the J/ψ and W masses. Top: The values of the four lowest-order coefficients. The value of ϵ_1 will be obtained from the momentum scale normalization and is expected to be small ($< 10^{-3}$). The value of ϵ_3 is extracted from this exercise. Middle: The average values of curvature terms in the expansion for both the J/ψ and W . Bottom: Term-by-term evaluation of Equation B.9 both in fractional mass error and in MeV/ c^2 for the J/ψ and W	151

List of Figures

1.1	Radiative corrections to the W propagator involving the top quark (left) and the Higgs boson (right).	4
1.2	The curves are from a calculation [14] of the dependence of the W boson mass on the top quark mass in the Standard Model using several Higgs masses. The band on each curve is the uncertainty obtained by folding in quadrature uncertainties on $\alpha(M_Z^2)$, the Z mass, and $\alpha_s(M_Z^2)$	5
2.1	Lowest order W production and kinematic diagrams.	8
2.2	The subprocess differential cross section is sharply peaked at half the W mass. The divergence disappears after integrating over \hat{s}	10
2.3	W production diagrams of $\mathcal{O}(\alpha_s)$. Time increases to the right.	11
2.4	Diagram of the transverse components of a W event. The neutrino momentum is not directly measured, but is inferred from momentum balance of \vec{u} and \vec{p}_T^μ . The component of \vec{u} parallel to the lepton direction is $u_{\parallel} = (\vec{u} \cdot \vec{p}_T^\mu)/p_T^\mu$. (It is labelled with a minus sign to emphasize the point that if it lies opposite of \vec{p}_T^μ , then it is a negative quantity.) The perpendicular component, u_{\perp} , is also a signed quantity where the sign is taken from an arbitrary convention, i.e. positive is always clockwise from p_T^μ	13
3.1	Upper: Elevation view of one quadrant of the CDF detector. The interaction point is lower left. Lower: Isometric view of CDF. Note the rectangular nature the central muon upgrade detector.	16
3.2	A diagram of the end plate of the CTC showing the slots for wires. Axial and stereo layers alternate. The long slots are axial layers and the short ones are stereo.	18
3.3	The number of hadronic absorption lengths as a function of θ . Total central muon coverage extends to about 40°	20
3.4	The muon coverage in the η - ϕ plane showing the individual coverage of each muon system. The small ϕ gaps in CMU are the spaces between wedges. The two large ϕ gaps in CMU are non-functioning chambers. The η extent of the CMP is not uniform because it is rectangular and not cylindrical.	21

3.5	Upper: Cross section of a CMU module showing radial alignment of alternate wires. The time difference is used at the trigger level to obtain a crude momentum measurement. The module subtends 5° in ϕ . Lower: Cross section of the CMP. The chambers form a rectangular box around the detector.	22
4.1	Data collection history over the run. The efficiency (right) is defined as recorded/delivered.	25
4.2	Diagram of the CDF data acquisition system. Three levels of triggers are followed by three separate output paths designed to optimize the collection of low-rate, high-momenta processes such as $W \rightarrow \mu\nu$ decays.	26
4.3	The identification of muons. The momentum, p_T^μ , is measured by the CTC. The muon loses energy in the calorimeter (E^{HAD} and E^{EM}). The extrapolated CTC track must match with the track in the muon chambers (Δx).	28
4.4	The match in the r - ϕ plane between the extrapolated CTC track and the CMU track segment. The arrows indicate the selection cut of 2 cm.	29
4.5	Left: Energy distribution in the CEM tower(s) traversed by the muon from W decay. The cut is at 2 GeV. Right: The same distribution for the CHA where the cut is at 6 GeV.	30
4.6	The transverse momentum spectrum of inclusive high- p_T muons.	30
4.7	The z distribution of VTX-reconstructed vertices closest to the origin of the muon track. The arrows indicate the selection cut of 60 cm.	32
4.8	Left: The impact parameter distribution for $W \rightarrow \mu\nu$ candidates. Right: The z vertex match to the origin of the track (z_o). The arrows indicate the cut values.	33
5.1	Diagram showing the effect of layer rotation on the measured momentum. With an ideal alignment, the momentum of a positron, p_+ , equals the momentum of an electron, p_- , if they have the same energy. Rotated layers produce a shift in the measured momentum: up(down) for positive charges, down(up) for negative charges ($p'_+ \neq p'_-$).	41
5.2	Deviation of wires ($r\Delta\phi$) from their nominal positions as a function of radius. Recall that each end of the wire is allowed to rotate independently. Circles are one end of the CTC ($z = +150$ cm) and triangles are the other end ($z = -150$ cm).	43
5.3	Transformations of the CTC. Upper Left: Translation of the CTC (a). Upper Right: Scaling the CTC by (b) $r \rightarrow \beta r$ and (c) $\rho \rightarrow \beta(\phi)\rho$. Middle: Rotations in (d) r - ϕ and (e) r - z . Lower: Skewing the CTC in r - z by (f) tilting the endplates and (g) conically deforming the endplates.	44
5.4	Variation of the J/ψ mass with $\Delta \cot \theta$ before and after the correction of Equation 5.1. (see Equation 5.4 for the mass dependence on $\cot \theta$).	47

5.5	The variation in ϕ of the difference in E/p between electrons and positrons. The shaded area indicates the expected variation from the $25\ \mu\text{m}$ RMS scatter of the wire guide rods (see Section 5.2.2).	48
5.6	The variation in $\cot\theta$ of the difference in E/p between electrons and positrons.	48
5.7	The distribution of E/p , after all corrections, for positives and negatives. The tail on the right is caused by energy loss from brehmmstrahlung. This tail is used to measure the amount of material between the beam and the CTC. The difference in the means of these two distributions is consistent with zero to better than a part in 10^3	49
5.8	The dimuon mass spectrum from the data, points, near the J/ψ mass in a $200\ \text{MeV}/c^2$ window. Upper: The curve is a Gaussian fit with a linear background in a $100\ \text{MeV}/c^2$ window. The arrows indicate the fit region. Lower: The curve is a Monte Carlo simulation including radiative effects.	51
5.9	The shift in the fit J/ψ mass as the true decay vertex moves away from the constraining vertex. While the mass for diverging tracks shifts substantially from that for converging tracks, the average remains close to zero.	54
5.10	The number of photon conversions to electron-positron pairs as a function of radius from the beamline. The major features of the CDF detector are labeled. The amount and type of material in the CTC inner wall is precisely know, allowing one to calibrate the other sources of material. The dashed line is the background.	55
5.11	Upper: The variation of the measured J/ψ mass with $\cot\theta_{\mu^+} + \cot\theta_{\mu^-}$ both with (open) and without (solid) the magnetic field map. Lower: The variation of the measured J/ψ mass with $\Sigma z^2 = z_{\mu^+}^2 + z_{\mu^-}^2$ where z is measured at a radius of $100\ \text{cm}$	57
5.12	The measured J/ψ mass versus $\Delta\cot\theta$. Upper: Before scaling $\cot\theta$. Lower: After scaling $\cot\theta$. The fit value at the kinematic point of $\Delta\cot\theta = 0$ is the same (within statistics) before and after scaling.	58
5.13	Variation of the measured J/ψ mass with time.	59
5.14	Variation of the measured J/ψ mass with the average $1/p_T^2$ of the two muons. The muons from W decays would lie in first bin of this plot ($0.001\ (\text{GeV}/c)^{-2}$). The average for J/ψ decays is $0.14\ (\text{GeV}/c)^{-2}$. The upper plot is before the $\cot\theta$ scaling; the lower plot is after. The slope in the lower plot is a factor of two smaller.	61
5.15	Invariant mass distribution of dimuon pairs near the Υ masses. The first three resonances can easily be distinguished. The curve is a sum of three gaussians and a quadratic background.	62
5.16	The dimuon mass spectrum near the Z mass. The arrows indicate the fit region of 76 to $106\ \text{GeV}/c^2$	64

6.1	Left: The average energy, E_u , in the towers bordering the towers traversed by the muon. Right: The number of towers traversed by the muon. The average is ~ 1.5	69
6.2	Scatter plot of $ \vec{u} $ versus p_T^Z . The diagonal line is $ \vec{u} = p_T^Z$ and indicates a systematic undermeasurement of $ \vec{u} $	71
6.3	Top: The distribution of $ \vec{u} $ for the data. Bottom: Distributions of u_{\parallel} and u_{\perp}	72
7.1	The initial p_T^W spectrum used in the W event simulation. The spectrum is derived from 555 $Z \rightarrow ee$ events.	77
7.2	The Level-2 muon trigger efficiency as a function of track p_T (GeV/c). The dotted lines indicate $\pm 1\sigma$ uncertainty in the slope of a linear fit.	78
7.3	Composition in the transverse plane of Z events used in the look-up table. Note that \vec{u} is decomposed relative to \vec{p}_T^Z as opposed to \vec{p}_T^W as in the case of the W . This is because the muon directions in the Z event and in the W event from the simulation are uncorrelated and it is meaningless to associate them in any way. After the Z event is transferred to the simulation \vec{u} is resplit into u_{\parallel} and u_{\perp}	80
7.4	Top: The distribution of $ \vec{u} $ for the data and simulation. The roughness of the simulation is due to the finite number of $Z \rightarrow ee$ events used to model the recoil response. Bottom: Distributions of u_{\parallel} and u_{\perp} . The small discrepancy between data and simulation in u_{\parallel} is only a little over one standard deviation and is covered by the uncertainty in the p_T^W scale factor, r	82
7.5	Upper: Data and simulation $\langle u_{\parallel} \rangle$ as a function of the muon p_T . Lower: The residuals of the data minus the simulation.	83
7.6	Upper: Data and simulation $\langle u_{\parallel} \rangle$ as a function of M_T . Lower: Data and simulation $\langle u_{\parallel} \rangle$ as a function of $ \vec{u} $	84
8.1	Transverse mass distributions of background processes present in the $W \rightarrow \mu\nu$ sample.	87
8.2	The CTC tracking efficiency as a function of η . The uncertainties are $\pm 10\%$, i.e. $c \pm 0.1$	88
8.3	Simulated M_T distribution including backgrounds. The $Z \rightarrow \mu\mu$ and $W \rightarrow \tau\nu$ backgrounds are also plotted separately to compare with the $W \rightarrow \mu\nu$ signal. The arrows indicate the fit region.	92
8.4	Top: Initial-state radiation diagrams. The photon is emitted from an incoming quark and is uncorrelated with the muon direction. Bottom: Final-state radiation and the $W\gamma$ vertex. Final-state radiation is responsible for most of the radiative effects.	93

8.5	Radiative and non-radiative lineshapes and the residual of them in percent. The residual is the difference divided by the area under the radiative distribution.	94
8.6	The cosine of the angle between the photon and the muon for radiative events. The y -axis is logarithmic.	95
9.1	Left: Lineshapes at various values of M_W for a fixed Γ_W . Right: Lineshapes at various values of Γ_W for a fixed M_W	99
9.2	The results of fitting simulated data samples of 10,000 events generated at a mass of 80.12 GeV/c ² and a width of 2.064 GeV. Top: The distribution of fitted masses (Left) and the distribution of uncertainties (Right). Bottom: The distribution of fitted widths (Left) and the corresponding uncertainties (Right).	101
9.3	Top: The ℓ polynomial surface resulting from the unconstrained fit to the W mass sample. Unfortunately, the ℓ data points cannot be overlaid. Bottom: The 1- σ ($\Delta\ell = 0.5$) and 2- σ ($\Delta\ell = 2.0$) contours in the M_W - Γ_W plane for the unconstrained fit to the data. The dashed line indicates the constrained fit line. The minimum ℓ on this line is the best fit value, M_W^{FIT}	102
9.4	The transverse mass distribution for data and simulation. The simulation does not include radiative corrections or small backgrounds. The arrows indicate the fit region.	103
9.5	The distribution of fitted masses (Left) and uncertainties (Right) for the constrained fit. The mean uncertainty agrees with that returned for the W mass sample.	104
9.6	The $-\ell$ curve for a one-dimensional fitter. The curve is a quadratic to demonstrate that ℓ fits well to a parabola.	105
9.7	Upper: Muon p_T spectrum for the W mass sample compared to simulation. Lower: Neutrino p_T spectrum compared to simulation. The soft edge at ~ 30 GeV/c is due to the M_T window of $65 < M_T < 100$ GeV/c ² . Note that the mass value used for the simulation comes from a fit to M_T , and not to the distributions shown.	109
9.8	Transverse mass spectra of W mass subsamples compared to the Monte Carlo simulation using a mass value of M_W^{FIT} . Upper: $ \vec{u} < 5$ GeV. Lower: $5 < \vec{u} < 20$ GeV.	110
9.9	The transverse mass spectra of W^+ and W^-	111

10.1	The correlation between ΔM_W (MeV/c ²) and ζ using various PDFs, where $\Delta M_W = M_W^{\text{PDF}} - M_W^{\text{MRS D}'}$. Three M_T regions are chosen for fitting, Top: $60 < M_T^W < 100$ GeV/c ² , Middle: $65 < M_T^W < 100$ GeV/c ² , and Bottom: $70 < M_T^W < 100$ GeV/c ² . The nominal fitting region is $65 < M_T^W < 100$ GeV/c ² (Middle). The solid lines are bounds of different behavior between PDFs. The dashed lines indicate $ \zeta = 2$. The uncertainty on the W mass is half of ΔM_W between points A and B.	120
11.1	Previously published W masses and this measurement compared to the LEP and SLAC predictions.	127
11.2	The data point is the combined CDF W mass measurement of 80.41 ± 0.18 GeV/c ² and a top quark mass of 176 ± 13 GeV/c ² [60]. The curves are from a calculation [14] of the dependence of the W boson mass on the top quark mass in the minimal Standard Model using several Higgs masses. The band on each curve is the uncertainty obtained by folding in quadrature uncertainties on $\alpha(M_Z^2)$, M_Z , and $\alpha_s(M_Z^2)$	129
A.1	Cross section of a single stack of chambers showing dimensions and major features.	133
A.2	An exploded view of a CMP chamber showing the endplates, wire support, and field-shaping pads. The scale is not exactly correct in this figure.	134
A.3	Left: The electric field values within the chamber. Horizontal specifies the long direction and vertical the short direction. Right: The electric field values along the horizontal at the center of the chamber. The values are from a solution of the potential problem, using a simultaneous over-relaxation method.	135
A.4	Top: The electric field lines within a CMP chamber. Bottom: The equipotential lines within the chamber.	136
A.5	The pre-amplifier electronics for a CMP chamber. This corresponds to four chambers (one stack).	138
A.6	Chamber production progress up through the first stage of construction.	139
A.7	The variation of the width of finished field-shaping pads. The step in the middle reflects the replacement of the cutting blades.	140
A.8	Distribution of breakdown voltages for the field-shaping pads. The pads are tested by applying a voltage between the copper strips and an aluminum plate to which the pad is pressed against. The pad is designed to nominally hold $\sim 10,000$ Volts in this configuration. The peak at ~ 2000 V is due to flawed pads, while the peak at 7000 V is due in part to some amount of integration beyond the last bin. The pads	141
A.9	The measured wire tensions in CMP chambers. The nominal tension was 250 g.	142

A.10	Left: Gas leak rates at the test pressure of 2 PSI above atmosphere. The operating pressure is a small fraction of a PSI (~ 0.01 PSI). Right: Anode dark currents at a voltage of 5600 V (200 V above operating voltage).	142
A.11	Left: Efficiency of one half of a CMP chamber. Only half the chamber overlaps the rest of the stack. Right: Position resolution of a chamber.	143
A.12	The measured position resolutions for all the constructed chambers.	144
A.13	The measured drift velocity for a typical chamber. The expected drift velocity is between 45 and 50 mm/ μ s.	144
A.14	The energy in the tower traversed by the muon for those with a CMP coincidence required (SOLID), and those without a CMP coincidence (DASHED). The later clearly shows the hadronic contamination (a real muon should peak at ~ 2 GeV).	145
A.15	Left: The position resolution of the CMP chambers as measured in W events. Right: The CMP-CTC matching distribution from the W mass sample. This width is consistent with that expected from multiple coulomb scattering.	146

Chapter 1

Introduction

1.1 Historical Perspective

No thesis would be complete without the traditional historical perspective, and so I begin. The birth of particle physics arguably occurred when Democritus theorized that all matter was composed of tiny indivisible “atoms”. Centuries later, it became obvious that there were different kinds of these atoms and the periodic table was proposed by Mendeleev. Various ideas about the atom floated around until Thompson’s 1897 discovery of the electron and, subsequently, Rutherford’s famous scattering experiment of 1911 in which the atom was determined to consist of a tiny, dense core of positive charge surrounded by a halo of orbiting electrons. This of course led to the development of quantum mechanics and eventually quantum electrodynamics (QED).

On a slightly different front, the observation of nuclear β decay produced a quandary in physics, namely, the non-conservation of energy. The speculation by Pauli in 1933, and later confirmation by Cowan and Reines, of the neutrino solved this predicament and, coupled with the discovery of the neutron, led to the idea of the weak nuclear force. This new force however did not fit into the neat and tidy theory of QED and it is here where the “Standard Model” enters the picture.

In the mid 1960's, Glashow, Weinberg and Salam developed a theory to combine the electromagnetic and weak interactions under one roof [1]. By utilizing an approach [2] in which a symmetric field in the Lagrangian is expanded around a nonzero minimum (spontaneously broken symmetry), they created a theory which was renormalizable (well behaved) and could contain massive gauge bosons which is one method of achieving the short range interaction characteristic of the weak nuclear force. This theory has since become known as the Standard Model of the electroweak interactions and consists of 6 leptons, 6 quarks, 4 gauge bosons which mediate the electromagnetic and weak (electroweak) interactions, and a symmetry breaking Higgs particle. The leptons and quarks are grouped into 3 generations.

$$\begin{array}{l}
 \textit{Leptons} \quad \left(\begin{array}{c} e \\ \nu_e \end{array} \right) \quad \left(\begin{array}{c} \mu \\ \nu_\mu \end{array} \right) \quad \left(\begin{array}{c} \tau \\ \nu_\tau \end{array} \right) \\
 \\
 \textit{Quarks} \quad \left(\begin{array}{c} u \\ d \end{array} \right) \quad \left(\begin{array}{c} c \\ s \end{array} \right) \quad \left(\begin{array}{c} t \\ b \end{array} \right)
 \end{array}$$

The gauge bosons consist of the photon (γ), the W^\pm , and the Z^0 , of which only the photon is massless. The standard model, however, also contains a large number of independent parameters including the electromagnetic and weak coupling constants, the weak mixing angle θ_W , and the masses of the fermions. This plentiful supply of arbitrary parameters is one reason for the continued search for a grander unification.

1.2 Experimental Observations

One great success of the electroweak (EWK) theory was the discovery of the predicted gauge bosons at the predicted masses. In 1983, these massive particles were found at the CERN SPS collider by both the UA1 detector, which measured $81 \pm_5^5$ GeV/c² for the

Experiment	Reference	Mode	Mass (GeV/c ²)
UA1-83	[3]	$e\nu$	81 ± 5
UA2-83	[4]	$e\nu$	80_{-6}^{+10}
UA1-84	[5]	$\mu\nu$	81_{-7}^{+6}
UA1-86	[6]	$e\nu$	83.5 ± 2.9
UA2-87	[7]	$e\nu$	80.2 ± 1.5
UA1-89	[8]	$\mu\nu$	81.8 ± 6.5
UA1-89	[8]	$\tau\nu$	$89 \pm 3 \pm 6$
CDF-89	[9]	$e\nu$	80.0 ± 4.1
UA2-90	[10]	$e\nu$	80.53 ± 0.49
CDF-90	[11]	$e\nu, \mu\nu$	79.91 ± 0.39
UA2-92	[12]	$c\nu$	80.36 ± 0.37

Table 1.1: Some previously published W mass measurements. Not all of the above measurements are independent. The mode is the decay channel of the W used in the measurement.

W mass [3], and by the UA2 detector, which found the W mass to be 80_{-6}^{+10} GeV/c² [4]. Since the 1989 turn-on of both the Large Electron-Positron (LEP) collider at CERN and the Stanford Linear Collider (SLC), the uncertainty on the Z mass has been reduced to less than a part in 10^4 (compared to several parts in 10^3 for the W), enabling truly precision tests of the EWK theory. A summary of measurements of the W mass is given in Table 1.1. Until LEP II comes online in 1996, the W remains solely in the domain of proton machines, since, to leading order, electron-positron accelerators must produce them in pairs to conserve charge.

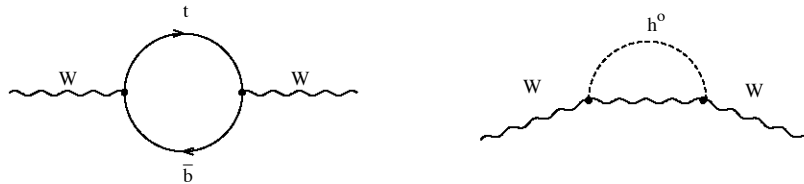


Figure 1.1: Radiative corrections to the W propagator involving the top quark (left) and the Higgs boson (right).

1.3 Precision Tests

The mass of the W, M_W , provides a test of the EWK theory through its relation to other EWK parameters. At Born-level, the W mass can be written as

$$M_W^2 = \frac{\pi\alpha}{\sqrt{2}G_F \sin^2 \theta_W}, \quad (1.1)$$

where α and G_F are the QED coupling constant and the Fermi constant and θ_W is the weak mixing angle. This equation is the result of a leading-order calculation where α is taken to be a constant. Radiative corrections to the W propagator (Figure 1.1) result in a slight modification to Equation 1.1,

$$M_W^2 = \frac{\pi\alpha_0}{\sqrt{2}G_F \sin^2 \theta_W} \frac{1}{(1 - \Delta r)}. \quad (1.2)$$

Here α_0 is $\alpha(Q^2 = 0)$ and the Q^2 dependence of alpha has been placed into the $1/(1 - \Delta r)$ term [13] which can further be split up into an “electromagnetic” term and a “weak” term. At a Q^2 corresponding to the W mass squared, the electromagnetic correction is dominated by logarithmic dependences on M_W and accounts for about a 7% increase in M_W over the leading order equation. The weak correction is a few percent and dominated both by a term which is quadratic in the top quark mass (Figure 1.2) and to a lesser extent by a logarithmic dependence on the mass of the

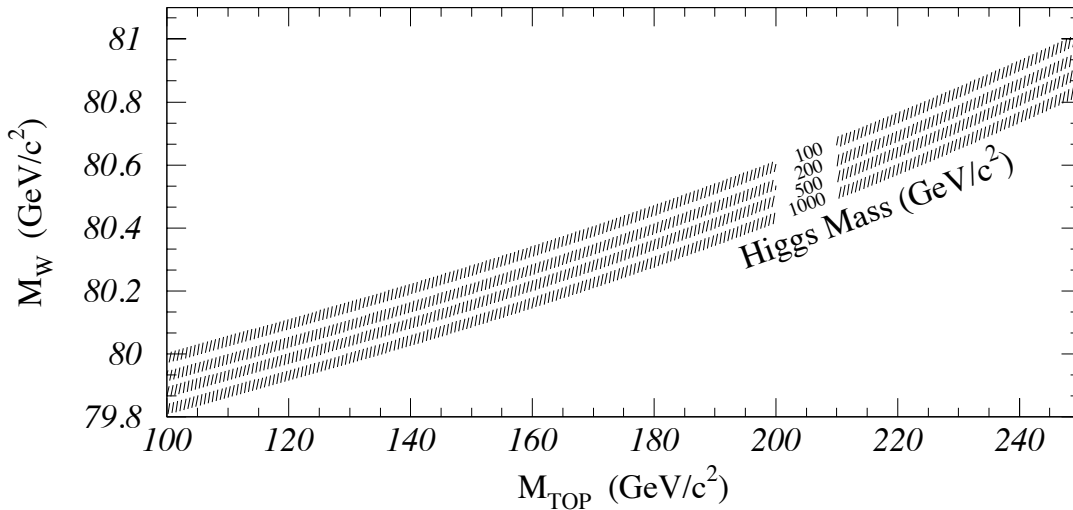


Figure 1.2: The curves are from a calculation [14] of the dependence of the W boson mass on the top quark mass in the Standard Model using several Higgs masses. The band on each curve is the uncertainty obtained by folding in quadrature uncertainties on $\alpha(M_Z^2)$, the Z mass, and $\alpha_s(M_Z^2)$.

Higgs. This relationship between masses introduced by the loop corrections, provides a sensitive test of the theory [16] and hence drives the goal of a precision W mass measurement.

1.4 Overview

In Chapter 2, a calculation of the lowest-order cross section for W production is presented. Combined with this is a determination of which kinematic variables are most sensitive to the mass of the W and a brief description of the method for extracting the W mass. In Chapters 3 and 4, the detector, data acquisition, and event selection are described. Chapters 5 and 6 detail the momentum and recoil measurements. Chapters 7, 8, and 9 describe the event simulation, the backgrounds, which are included in

the event simulation, and the fitting algorithm. Finally, the systematic uncertainties and conclusions are presented in Chapters 10 and 11.

As seen in Table 1.1, the best previous measurements of the W mass have uncertainties of order $400 \text{ MeV}/c^2$. The goal of this analysis is to reduce the uncertainty to $200 \text{ MeV}/c^2$, a factor of two improvement over previous measurements. With an expected statistical uncertainty of $150\text{-}200 \text{ MeV}/c^2$, the systematic uncertainty must be kept to $\sim 100 \text{ MeV}/c^2$; therefore, an attempt is made to keep individual systematic errors less than $50 \text{ MeV}/c^2$.

Chapter 2

Theory

The determination of the mass of the W vector boson is similar to the determination of the energy of an excited state of say the Hydrogen atom, H . The W boson decays to a muon and a neutrino; the excited II' decays to II and a photon. The energy of the muon (and neutrino) is related to the energy (or mass) of the W in the same way that the photon energy is related to the energy of II' . To determine the energy of II' , a distribution of energies of the photons is made and the mean and the width determine the energy and lifetime of the excited state, H' . In like manner, a distribution of the energies¹ of the muon determine the mass of the W . Since the W bosons are produced in $\bar{p}p$ collisions, and since this production alters the energy distribution of the muon, the decay process must be combined with the production process. This combination is the cross section.

2.1 Lowest Order Cross Section

The lowest order Feynman diagram for the production and subsequent decay of a W is shown in Figure 2.1. The incoming particles are the constituent quarks of the proton

¹ Although the term energy is used in this qualitative comparison to the Hydrogen atom, in practice, the momentum of the muon is used.

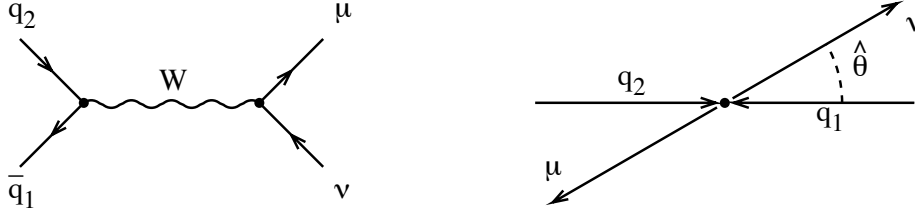


Figure 2.1: Lowest order W production and kinematic diagrams.

and antiproton and the outgoing particles are the muon and neutrino. Since the quarks are bound within the proton and antiproton, this diagram represents only a subprocess which must be summed over all quark species and weighted with appropriate parton distribution functions². The matrix element for this subprocess is

$$\mathcal{M} = \frac{G_F}{\sqrt{2}} M_W^2 V_{q_1 q_2} \frac{\bar{v}(q_1) \gamma^\alpha (1 - \gamma_5) u(q_2) \bar{u}(\nu) \gamma_\alpha (1 - \gamma_5) v(\mu)}{\hat{s} - M_W^2 + i \hat{s} \Gamma_W / M_W}. \quad (2.1)$$

Here M_W and Γ_W are the mass and width of the W , G_F is the Fermi constant, $V_{q_1 q_2}$ is the $q_1 q_2$ term in the Kobayashi-Maskawa mixing matrix and \hat{s} is the total energy squared in the subprocess center of mass. Note that the energy-dependent form of the propagator is used[17]. The u 's, v 's and γ 's are the usual Dirac wavefunctions and matrices. The mass of the muon has been ignored in this and all subsequent calculations. Squaring the matrix element and summing/averaging over final/initial spins gives

$$\sum_{spins} \overline{|\mathcal{M}|^2} = 4 |V_{q_1 q_2}|^2 \left(\frac{G_F M_W^2}{\sqrt{2}} \right)^2 \frac{\hat{s}^2 (1 + \cos \hat{\theta})^2}{(\hat{s} - M_W^2)^2 + \hat{s}^2 \Gamma_W^2 / M_W^2} \quad (2.2)$$

²The incident quarks do not in general have equal and opposite momenta in the lab frame, i.e. the subprocess center-of-mass frame is not the laboratory (detector) frame. The momentum distributions of the quarks, relative to their proton bag, are described by parton distribution functions.

where $\hat{\theta}$ is the polar angle of the muon in the center of mass frame. The differential cross section for this subprocess is then

$$\frac{d\hat{\sigma}}{d\cos\hat{\theta}}(q_1q_2 \rightarrow \mu\nu) = \frac{|V_{q_1q_2}|^2}{8\pi} \left(\frac{G_F M_W^2}{\sqrt{2}} \right)^2 \frac{\hat{s}(1 + \cos\hat{\theta})^2}{(\hat{s} - M_W^2)^2 + \hat{s}^2 \Gamma_W^2 / M_W^2}, \quad (2.3)$$

and the total cross section is

$$\hat{\sigma}(q_1q_2 \rightarrow \mu\nu) = \frac{|V_{q_1q_2}|^2}{3\pi} \left(\frac{G_F M_W^2}{\sqrt{2}} \right)^2 \frac{\hat{s}}{(\hat{s} - M_W^2)^2 + \hat{s}^2 \Gamma_W^2 / M_W^2}. \quad (2.4)$$

Writing the differential cross section in terms of the total cross section leads to

$$\frac{d\hat{\sigma}}{d\cos\hat{\theta}}(q_1q_2 \rightarrow \mu\nu) = \frac{3\hat{\sigma}}{8}(1 + \cos\hat{\theta})^2. \quad (2.5)$$

The presence of $\hat{\theta}$ in this equation requires a measurement of the 4 momenta of both the muon and neutrino; however, direct neutrino measurements are not tractable. Additionally, one would like a sharply peaked distribution where the peak is sensitive to the mass of the W . The above differential cross section in $\cos\hat{\theta}$ is neither sharply peaked nor sensitive to M_W which necessitates the use of some other variable for a viable measurement. The variables that can be used are the transverse and longitudinal momentum components of the muon, p_T^μ and p_L^μ , and the transverse momentum of the neutrino, p_T^ν , which is determined by requiring transverse momentum balance (see Section 2.2). Transverse and longitudinal are defined with respect to the beam direction. The longitudinal momentum component of the muon is not very useful because of the longitudinal boost received from the parton distribution functions. In addition, requiring longitudinal momentum balance in the same way as the transverse components does not work since a large fraction of the total energy in the event is directed along the beamline and is not detected. This leaves only the transverse components of momentum.

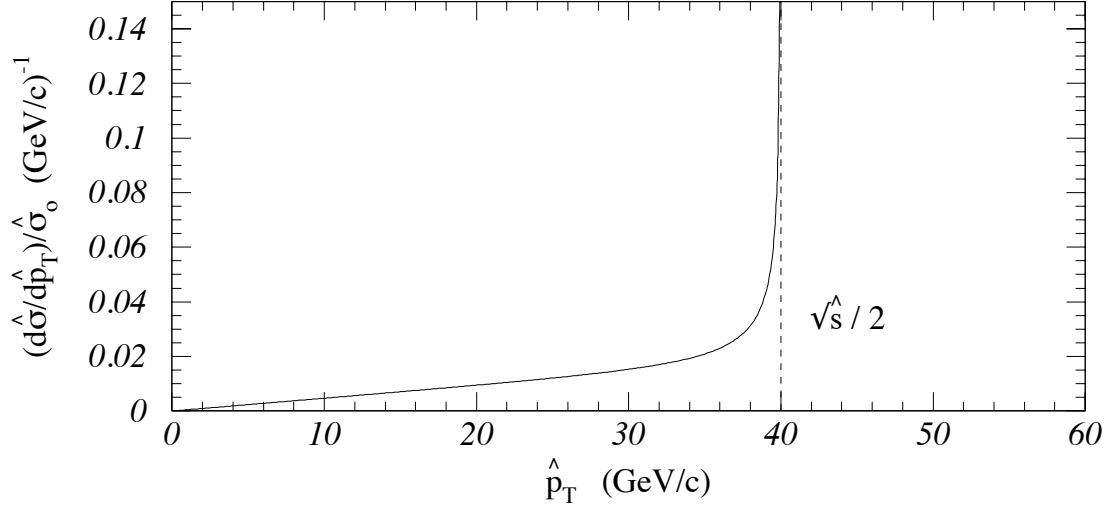


Figure 2.2: The subprocess differential cross section is sharply peaked at half the W mass. The divergence disappears after integrating over \hat{s} .

The first approach is to convert the cross section in $\cos \hat{\theta}$ to a cross section in p_T^μ . The lowest-order diagram results in $p_T^\mu = p_T^\nu = \hat{p}_T$ and

$$\hat{p}_T = \frac{1}{4} \hat{s} \sin^2 \hat{\theta}. \quad (2.6)$$

The Jacobian for the transformation from $\hat{\theta}$ to p_T is

$$\frac{d \cos \hat{\theta}}{d \hat{p}_T^2} = -\frac{2}{\hat{s}} \left(1 - \frac{4 \hat{p}_T^2}{\hat{s}}\right)^{-\frac{1}{2}}, \quad (2.7)$$

leading to the differential cross section

$$\frac{d \hat{\sigma}}{d \hat{p}_T^2} = \frac{\hat{\sigma}}{\hat{s}} \frac{3}{2} \frac{(1 - 2 \hat{p}_T^2 / \hat{s})}{(1 - 4 \hat{p}_T^2 / \hat{s})^{1/2}}, \quad (2.8)$$

which satisfies the criteria of being sharply peaked and sensitive to M_W ; the peak is at $\hat{p}_T = \frac{1}{2} M_W$ (Figure 2.2). If the universe was strictly a leading-order place,

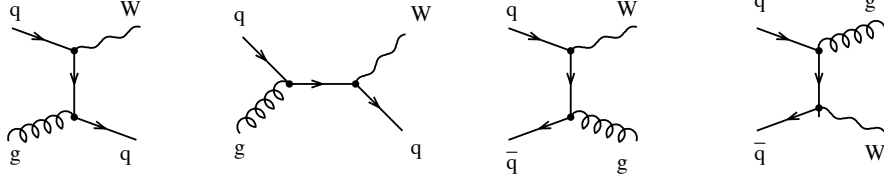


Figure 2.3: W production diagrams of $\mathcal{O}(\alpha_s)$. Time increases to the right.

Equation 2.8 would be a perfect solution. Unfortunately, higher-order diagrams give the W a transverse momentum from initial state gluon radiation and gluon compton scattering (See Figure 2.3). This p_T^W smears out the sharp Jacobian peak and causes a loss of sensitivity to M_W .

Another approach, which is less sensitive to the p_T of the W , is to use the transverse mass [18] of the lepton-neutrino pair instead of the transverse momentum of the lepton. Transverse mass is defined as

$$M_T^2(\mu, \nu) = (|\vec{p}_T^\mu| + |\vec{p}_T^\nu|)^2 - (\vec{p}_T^\mu + \vec{p}_T^\nu)^2, \quad (2.9)$$

and ranges from 0 when the muon and neutrino are entirely longitudinal, to M_W when they are entirely transverse. The transverse mass is less sensitive to p_T^W than the lepton p_T because under a Lorentz boost, these two quantities transform as

$$M_T' = M_T + \mathcal{O}\left(\left[\frac{p_T^W}{E_T^W}\right]^2\right) + \dots \quad (2.10)$$

$$p_T' = p_T + \mathcal{O}\left(\frac{p_T^W}{E_T^W}\right) + \dots \quad (2.11)$$

More importantly, unlike the lepton p_T distribution, the endpoints are not affected by p_T boosts of the W leaving the sensitivity to M_W intact³.

³The maximum value M_T can be is M_W . This is independent of p_T^W .

Returning to the leading-order differential cross section and transforming from p_T to M_T using $M_T = 2|\vec{p}_T^\mu| = 2|\vec{p}_T^\nu|$, the differential cross section becomes

$$\frac{d\hat{\sigma}}{dM_T^2} = \frac{\hat{\sigma}}{\hat{s}} \frac{3}{8} \frac{(2 - M_T^2/\hat{s})}{(1 - M_T^2/\hat{s})^{1/2}}. \quad (2.12)$$

To get from the subprocess frame to the lab frame, one must sum over quark species and integrate over quark momenta, weighting the subprocess cross section with the parton distribution functions,

$$d\sigma(p\bar{p} \rightarrow \mu\nu X) = \frac{K}{3} \sum_{q_1, q_2} \int_0^1 dx_1 \int_0^1 dx_2 q_1(x_1, \hat{s}) q_2(x_2, \hat{s}) d\hat{\sigma}(q_1 q_2 \rightarrow \mu\nu) \quad (2.13)$$

Here the factor of $1/3$ is the average over initial quark colors, K is a constant that corrects the cross section for non-leading-order effects, and q_1, q_2 are the quark distribution functions evolved up to $Q^2 = \hat{s}$.

2.2 W Mass Extraction

Figure 2.4 shows the detected transverse momentum components of a W event, with the exception of the neutrino which is not seen. The beamline is into the page. The $\vec{p}_{\bar{p}p}$ component in this figure, $\vec{p}_{\bar{p}p}$, results from the breakup of the proton and antiproton and should be symmetrically distributed in azimuthal angle. The observed distribution of $\vec{p}_{\bar{p}p}$ has a mean of zero and an RMS width⁴ that is typically ~ 3 GeV. The recoil component, \vec{p}_{recoil} , is from the hadrons that are recoiling against the W transverse momentum, i.e. from the hadronization of the outgoing quark or gluon in Figure 2.3. These two components are lumped together and called \vec{u} , since there is no way to experimentally distinguish between them. Sections 6 and 7.2.3 discuss the measurement and calibration/simulation of \vec{u} . From momentum conservation, \vec{p}_T^μ and \vec{u} are combined

⁴The reason it has a non-zero width is that some of the hadrons are undetected; thus, the net momentum becomes non-zero.

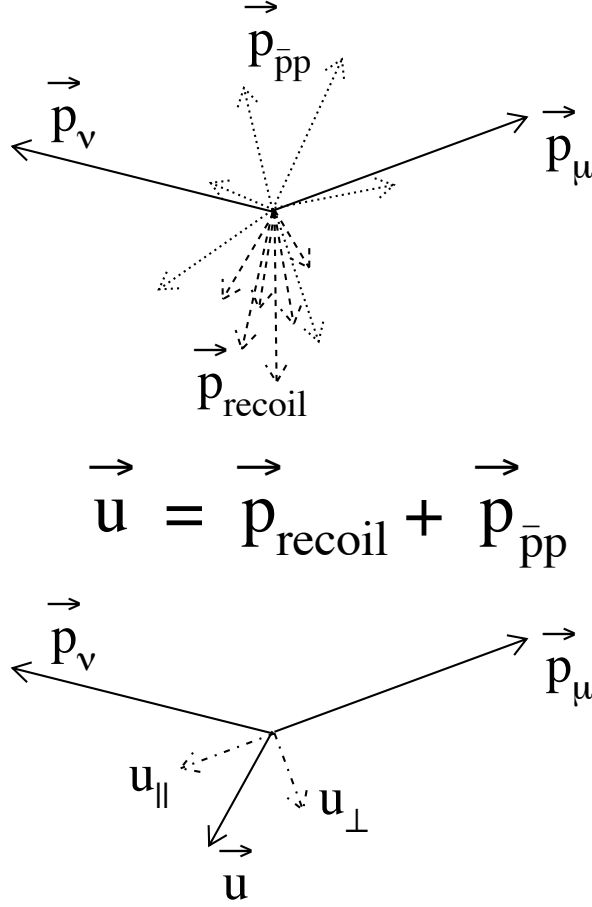


Figure 2.4: Diagram of the transverse components of a W event. The neutrino momentum is not directly measured, but is inferred from momentum balance of \vec{u} and \vec{p}_T^μ . The component of \vec{u} parallel to the lepton direction is $u_{\parallel} = (\vec{u} \cdot \vec{p}_T^\mu) / p_T^\mu$. (It is labelled with a minus sign to emphasize the point that if it lies opposite of \vec{p}_T^μ , then it is a negative quantity.) The perpendicular component, u_{\perp} , is also a signed quantity where the sign is taken from an arbitrary convention, i.e. positive is always clockwise from p_T^μ .

to obtain $\vec{p}_T^\nu = -\vec{u} - \vec{p}_T^\mu$ and subsequently M_T as defined above. When $|\vec{u}| \ll p_T^\mu$, the transverse mass is approximated by

$$M_T \approx 2p_T^\mu + u_{\parallel} \tag{2.14}$$

where u_{\parallel} is defined in Figure 2.4. Because of this direct relation, it is important to determine not only the effects of event selection criteria on u_{\parallel} , but also how well the Monte Carlo simulation reproduces those effects. Given that an event-by-event measurement of M_T is possible, the mass of the W , M_W , is extracted by performing a log-likelihood fit of simulation M_T distributions to the data (see Sections 7 and 9).

Chapter 3

The CDF Detector

3.1 Overview

The Collider Detector at Fermilab (CDF) [19] is a 5000 ton, azimuthally and forward-backward symmetric, magnetic detector designed to study $\bar{p}p$ collisions at Fermilab's Tevatron. The magnetic spectrometer consists of tracking devices inside a 3-m diameter, 5-m long superconducting solenoidal magnet which operates at 1.4116 T. The detector is divided into a central region ($30^\circ < \theta < 150^\circ$), end-plugs ($10^\circ < \theta < 30^\circ$, $150^\circ < \theta < 170^\circ$), which form the pole pieces for the solenoidal magnet, and forward regions ($2^\circ < \theta < 10^\circ$, $170^\circ < \theta < 178^\circ$). The calorimeters are constructed with a projective tower geometry, with towers subtending approximately 0.1 in pseudorapidity¹, η , by 15° in ϕ (central) or 5° in ϕ (plug and forward). Each tower consists of an electromagnetic calorimeter followed by a hadronic calorimeter at larger radius. Muon chambers are placed outside the central region and toroidal steel magnets and chambers provide additional muon coverage on each end. An elevation view of one quarter of the CDF detector is shown in Figure 3.1 along with an isometric view of the full detector.

¹Pseudorapidity (η) is defined as $\eta \equiv -\ln(\tan(\theta/2))$, where θ is the polar angle relative to the proton-beam direction.

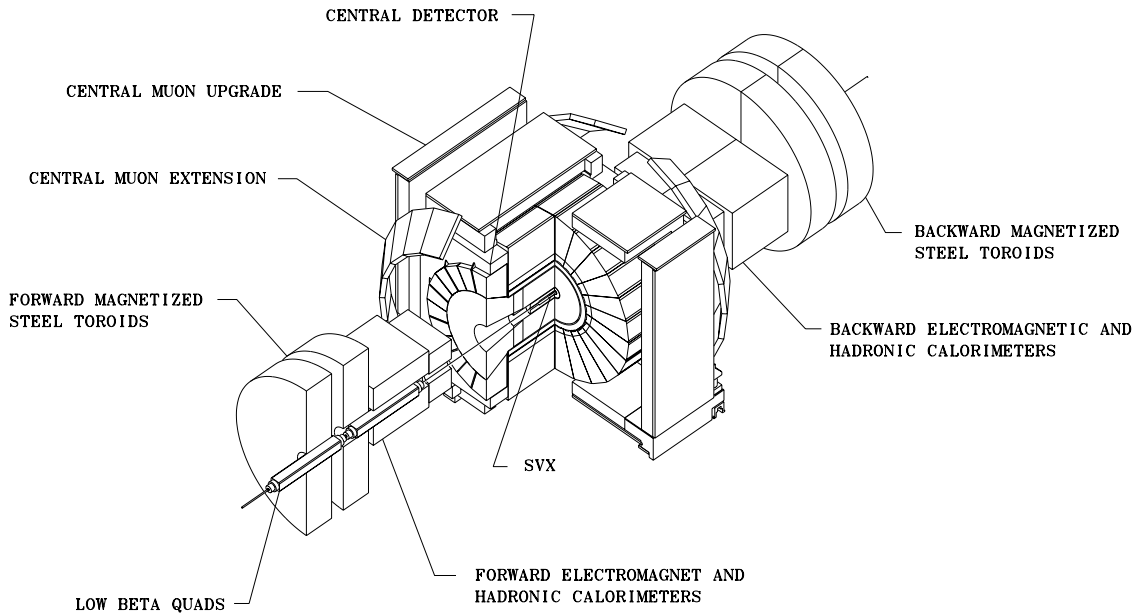
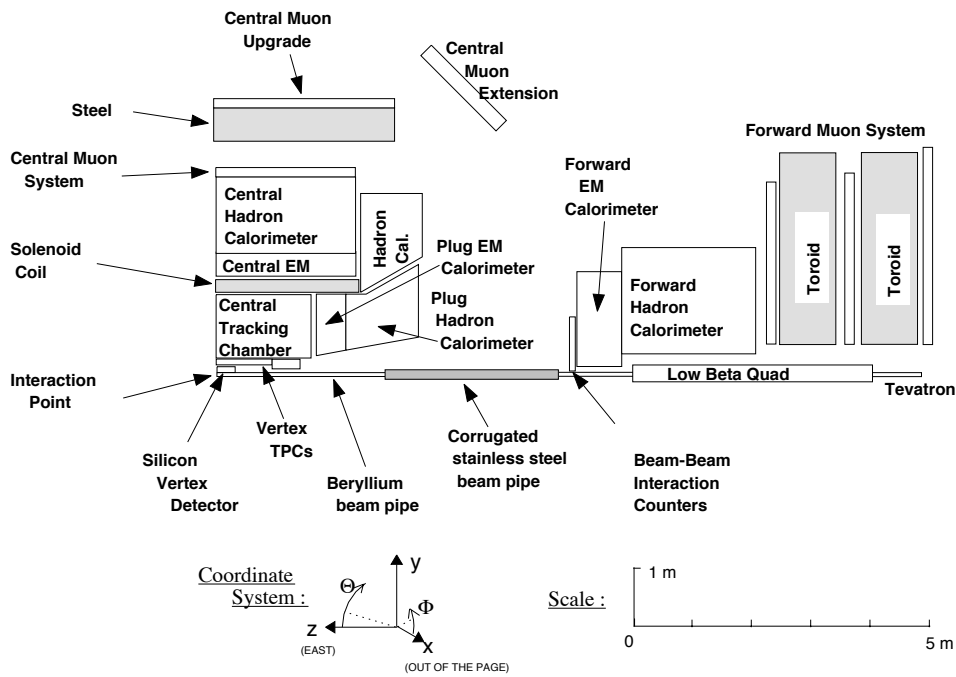


Figure 3.1: Upper: Elevation view of one quadrant of the CDF detector. The interaction point is lower left. Lower: Isometric view of CDF. Note the rectangular nature the central muon upgrade detector.

3.2 Tracking Chambers

The inner tracking system of CDF consists of the silicon vertex detector (SVX) [20], the vertex time projection Chambers (VTX) [21], and the central tracking chamber (CTC) [22]. The SVX is a four-layer silicon microstrip detector located directly outside the 1.9-cm radius beryllium beampipe. The four layers are at radii of 3.0, 4.2, 5.7, and 7.9 cm from the beamline. The SVX provides a precise measurement of impact parameter, but has only $\sim 60\%$ acceptance along z . Because of this, it is used to determine the r - ϕ beam position for each $\bar{p}p$ store. This beam position can be extrapolated beyond the SVX coverage and is used as additional information to augment the CTC. Outside the SVX is the VTX, which provides r - z tracking information out to a radius of 22 cm for $|\eta| < 3.25$. In this analysis, it is used to define the z position of the interaction vertex, which, when combined with the r - ϕ beam position, provides another point for the track fit (see below). Outside the VTX is the CTC which is a 3.2-meter long cylindrical drift chamber with 84 sampling layers, organized in 5 axial and 4 stereo “super-layers” (Figure 3.2). Axial super-layers have 12 radially separated layers of sense wires, all parallel to the z axis; these measure the r - ϕ position of a track. Stereo super-layers have 6 sense wire layers with a $\sim 3^\circ$ stereo angle; these measure a combination of r - ϕ and z information. Axial and stereo information is combined to form a 3-dimensional track using standard small-angle stereo techniques [22]. The stereo angle direction alternates at each stereo super-layer to resolve ambiguity.

3.3 Calorimeters

Outside the tracking chambers, in radius, are the electromagnetic and hadronic calorimeters which cover 2π in azimuth and from -4.2 to 4.2 in pseudorapidity (η). The central calorimeter, is constructed as 24 wedges in ϕ for each half of the detector. Each wedge has 10 electromagnetic towers (CEM) [23], which use lead as the absorber.

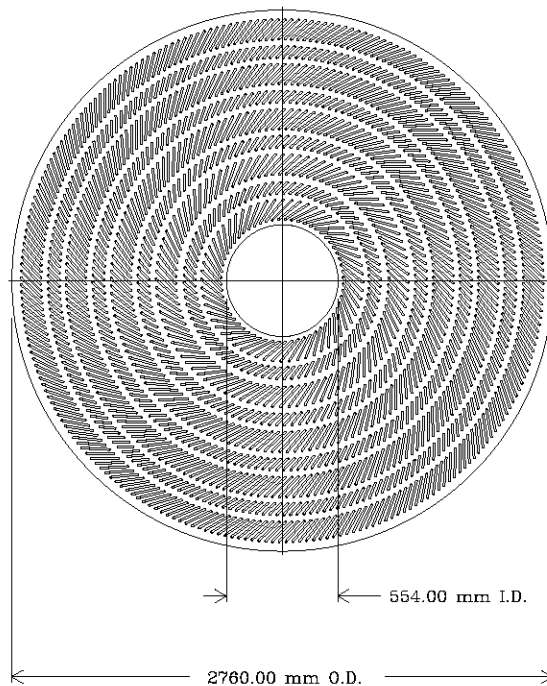


Figure 3.2: A diagram of the end plate of the CTC showing the slots for wires. Axial and stereo layers alternate. The long slots are axial layers and the short ones are stereo.

ber and 12 hadronic towers (CHA and WHA) [24], which use steel as the absorber. Gas-based electromagnetic and hadronic calorimeters (PEM, PHA, FEM, FHA) [25], extend the η coverage to $|\eta| < 4.2$ and together with the CHA and CEM are used to measure the recoil energy, \vec{u} . The resolutions of the calorimeters are parameterized as $(\sigma_E/E)^2 = (\alpha/\sqrt{E})^2 + (\kappa)^2$ and are summarized in Table 3.1.

3.3.1 Central Electron Detection

The energies of central electrons, used in the alignment of the CTC (see Section 5.2.2) and in the determination of the W mass in the electron channel², are measured

²Details of the $W \rightarrow e\nu$ analysis, including the CEM calibration, can be found in [26, 27].

Calorimeter	Energy Resolution
CEM	$13.7\%/\sqrt{E_T} \oplus 2\%$
CHA	$50\%/\sqrt{E_T} \oplus 3\%$
CHA	$75\%/\sqrt{E} \oplus 4\%$
PEM	$22\%/\sqrt{E} \oplus 2\%$
PHA	$106\%/\sqrt{E} \oplus 6\%$
FEM	$26\%/\sqrt{E} \oplus 2\%$
FHA	$137\%/\sqrt{E} \oplus 3\%$

Table 3.1: Summary of calorimeter energy resolutions. PEM and PHA are the endcap calorimeters and FEM and FHA are the forward/backward calorimeters. The symbol \oplus signifies that the constant term is added in quadrature in the resolution.

from the electromagnetic shower produced in the central electromagnetic calorimeter (CEM) [23]. A proportional chamber measures the electron shower position (both the $r\Delta\phi$ distance from the tower center and the z position) at a depth of ~ 6 radiation lengths.

3.4 Central Muon Detector

Outside the CHA are two sets of muon detectors: the central muon chambers (CMU) [28], and the central muon upgrade chambers (CMP) [29], separated by ~ 60 cm of steel. The additional steel allows the two muon detectors to be used in coincidence to improve the signal-to-noise by reducing the number of non-muons penetrating both detectors. Figure 3.3 shows the number of hadronic absorption lengths between the center of the detector and the muon detectors as a function of θ . The central muon extension chambers (CMX) increase the muon coverage in η from 0.6 to 1.0. The η - ϕ coverage of the muon detectors is shown in Figure 3.4.

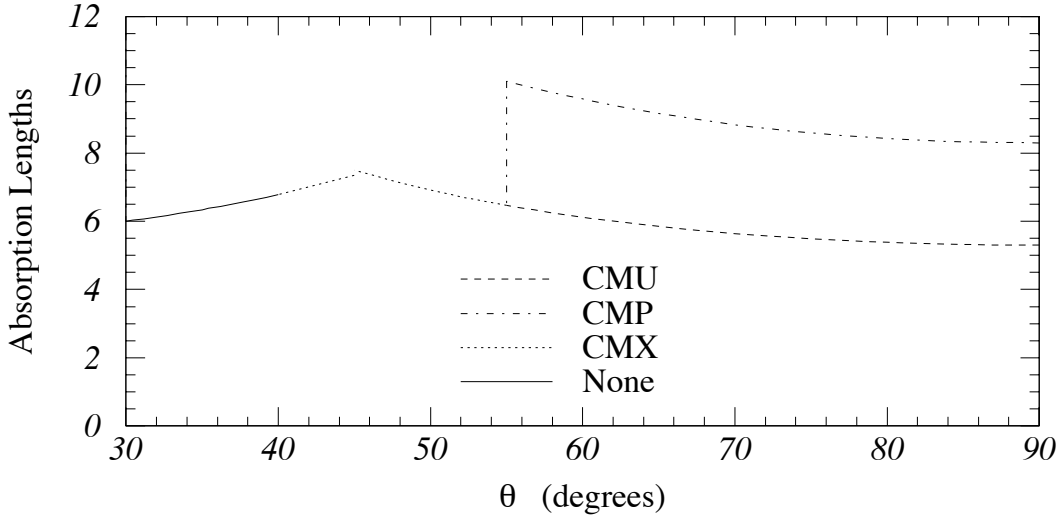


Figure 3.3: The number of hadronic absorption lengths as a function of θ . Total central muon coverage extends to about 40° .

3.4.1 Central Muon Chambers

The inner muon chambers (CMU) consist of four layers of drift cells (Figure 3.5) covering the region $|\eta| < 0.6$. The drift cell wires are parallel to the z axis and alternate layers are radially aligned providing a crude momentum measurement. The chambers are arranged into 24 “wedges” in ϕ for each half of the detector ($-0.6 < \eta < 0$ and $0 < \eta < 0.6$). Muon tracks in the CMU are reconstructed using time-to-distance relationships in the drift (ϕ) direction, and charge division in the longitudinal (z) direction. Resolutions of $250 \mu\text{m}$ in the drift direction and 1.2 mm in z are determined from cosmic-ray studies [28]. Clusters of hits in at least three layers are found separately in the r - ϕ and r - z planes. These two sets of clusters are merged and a linear fit is performed generating three-dimensional track segments.

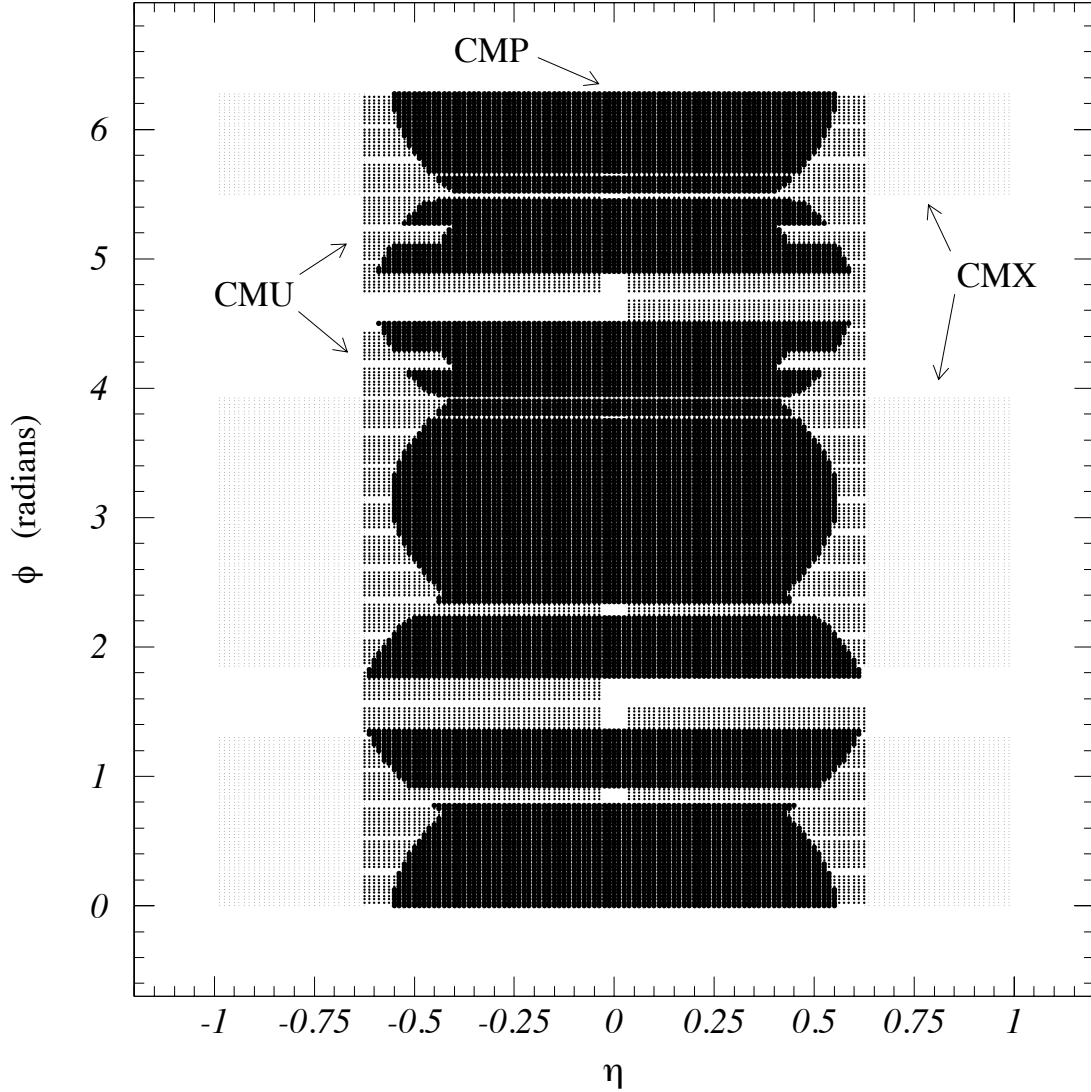


Figure 3.4: The muon coverage in the η - ϕ plane showing the individual coverage of each muon system. The small ϕ gaps in CMU are the spaces between wedges. The two large ϕ gaps in CMU are non-functioning chambers. The η extent of the CMP is not uniform because it is rectangular and not cylindrical.

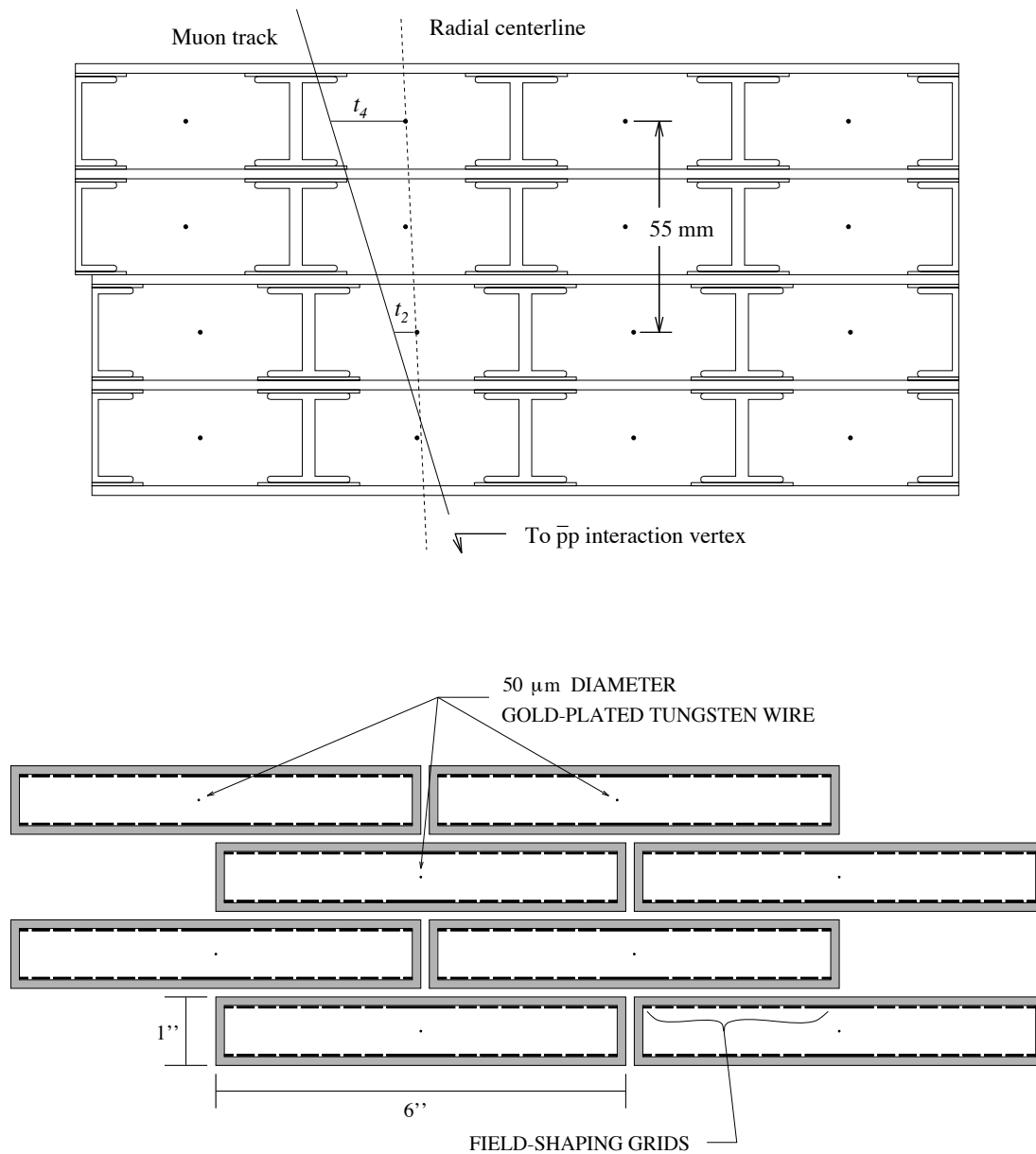


Figure 3.5: Upper: Cross section of a CMU module showing radial alignment of alternate wires. The time difference is used at the trigger level to obtain a crude momentum measurement. The module subtends 5° in ϕ . Lower: Cross section of the CMP. The chambers form a rectangular box around the detector.

3.4.2 Central Muon Upgrade

The CMP are also composed of four layers of drift cells, but in a staggered geometry (Figure 3.5), and covering on average the region $|\eta| < 0.5$. This results in a reduced geometrical acceptance for muons when used in coincidence with the CMU (see Figure 3.4); however, the gain in signal-to-noise more than compensates. See Appendix A for a full discussion of the CMP.

3.4.3 Center Muon Extension

The CMX is similar in chamber design to the CMP, but functions like the CMU in that the wires are radially aligned with the interaction point enabling them to be used in the trigger. Because the CMX is unshielded from both the beamline (see Figure 3.1) and the forward calorimeters, it is subject to a spray of low-energy particles emanating from interactions of small-angle³ particles from the $\bar{p}p$ collision with both the beampipe and the forward calorimeters. This spurious source of signals results in a large rate which must be artificially lowered introducing systematic errors into any analysis attempting to use the CMX. As a result, the data sample for this W mass measurement (see Section 4.5) does not include muons traversing the CMX detector.

³Here small-angle is with respect to the beamline, i.e. small θ .

Chapter 4

Data Sample

During the 1992-1993 run, CDF collected data corresponding to an integrated luminosity¹ of 20.7 pb^{-1} (Figure 4.1). From this was removed 1 pb^{-1} of data corresponding to unstable conditions in either the detector or the accelerator.

4.1 Data Acquisition

The CDF data acquisition system consists of a three-level trigger followed by a three-way storage mechanism (Figure 4.2). The crossing rate of proton and antiproton bunches in the Tevatron is 286 kHz, with a mean interaction rate of 0.6 interactions per crossing at a luminosity of $3.6 \times 10^{30} \text{ cm}^{-2} \text{ sec}^{-1}$, typical of the data used in this measurement. The first two levels of the trigger [30] consist of dedicated electronics with separate data paths from the data readout system. The third level [31], which occurs after the event information is digitized and stored, uses a farm of Silicon Graphics computers to reconstruct the event. The overall rejection factors for each of the three levels are typically 600, 100, and 4, respectively. Events that pass level 3 are written

¹The total amount of data, or integrated luminosity, $\int \mathcal{L} dt$, as it is usually called, is expressed in units of inverse cross section. To convert to numbers of events, simply multiply by the cross section of the process of interest. Multiplying the instantaneous luminosity, \mathcal{L} , by some cross section gives the rate for that process.

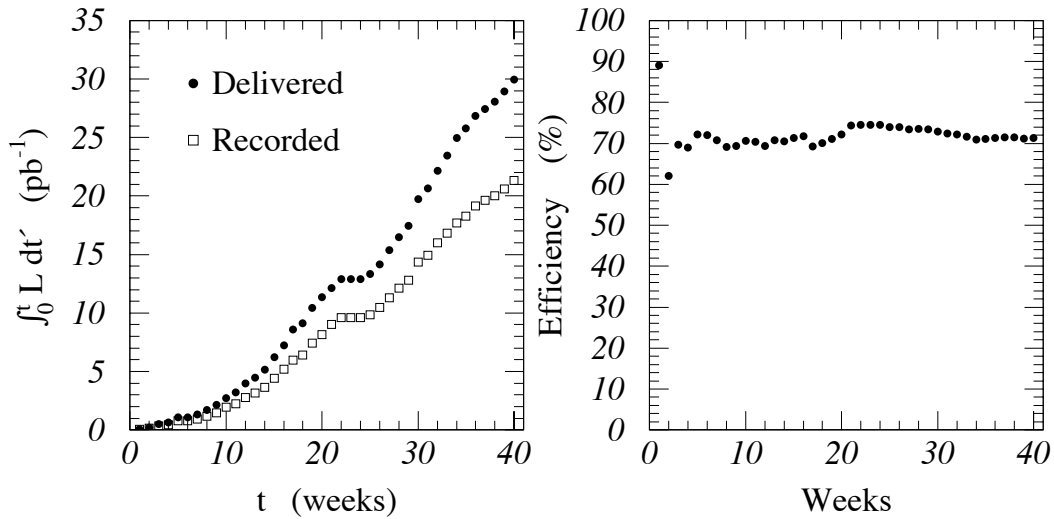


Figure 4.1: Data collection history over the run. The efficiency (right) is defined as recorded/delivered.

to one or more of three output paths by a VAX computer that controls the overall flow of data. The main output path is stored on 8 mm magnetic tape and contains the bulk of the data. A special “express” path receives a small subset of rare events such as $W \rightarrow \mu\nu$ and top quark candidates. This path is written to disk and quickly made available to the experimental collaboration. A third path is reserved for higher-rate processes that are not output to the main data path.

4.2 Muon Trigger

The level-1 muon trigger [32] uses timing information from the CMU to detect the presence of a high- p_T muon and requires a coincidence hit in the CMP if the muon should have traversed it. At level 2, information about the ϕ coordinate of the muon from the level-1 muon trigger is combined with CTC track information from the Central Fast Tracker (CFT) [33]. The CFT looks in the r - ϕ plane for hit patterns in the CTC consistent with a high- p_T particle. The particle moves through a magnetic field;

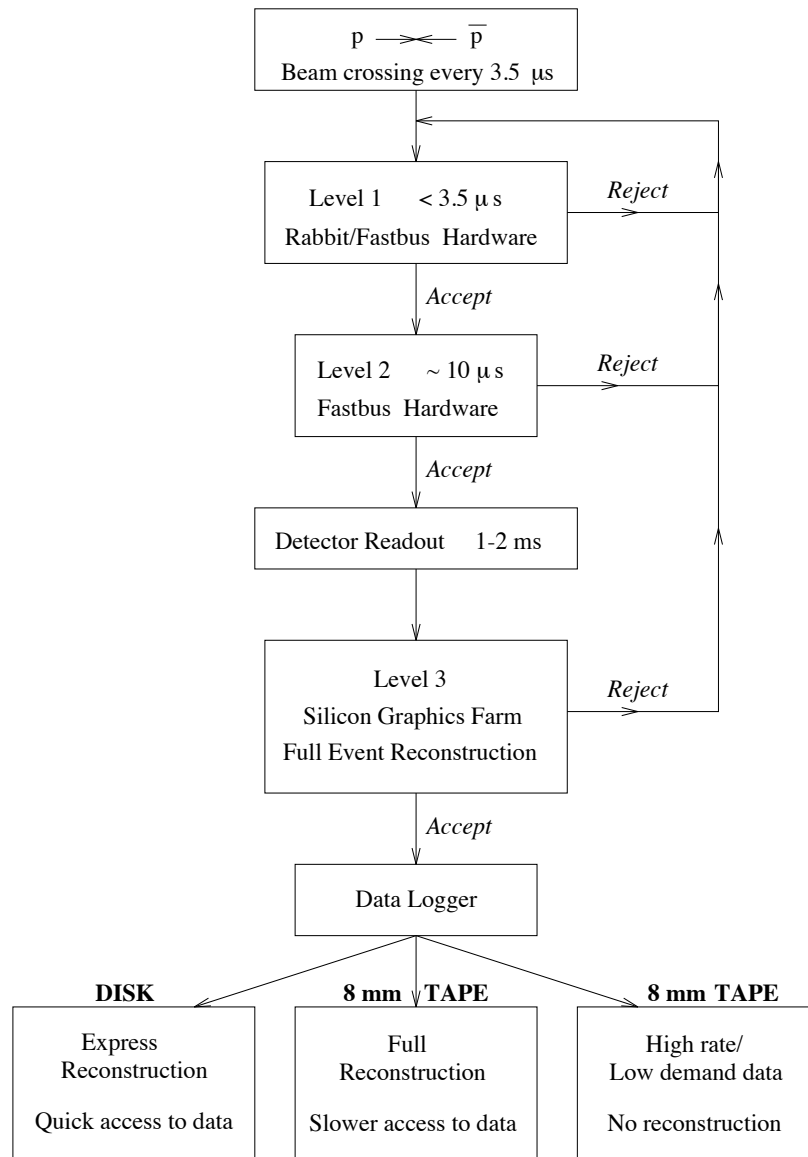


Figure 4.2: Diagram of the CDF data acquisition system. Three levels of triggers are followed by three separate output paths designed to optimize the collection of low-rate, high-momenta processes such as $W \rightarrow \mu\nu$ decays.

thus, the curvature of the track depends on the particle's momentum, i.e. an infinite momentum particle produces a straight track. If a CFT candidate track exists within 5° in ϕ of the muon, the muon level-2 trigger is satisfied. The level-3 high- p_T muon trigger fully reconstructs the event and searches for a muon candidate with:

- $p_T^\mu > 18 \text{ GeV}/c$
- CMU $|\Delta x| < 5 \text{ cm}$
- CMP $|\Delta x| < 10 \text{ cm}$
- $E^{\text{HAD}} < 6.0 \text{ GeV}$

The second item is equivalent to a ϕ match between the hits in the muon chamber and the CTC track and the third item refers to the energy measured in the CHA tower that the muon traversed. Both of these are discussed in the next section. If the event passes level 3 it is stored and later reprocessed by the offline reconstruction algorithm which is identical to the level-3 trigger algorithm except for improved calibration information.

4.3 Muon Identification

The identification of a high- p_T muon is shown in Figure 4.3. After the offline reconstruction program, the muon candidate must pass the following selection cuts:

- $p_T^\mu > 18 \text{ GeV}/c$
- CMU $|\Delta x| < 2 \text{ cm}$
- $E^{\text{HAD}} < 6.0 \text{ GeV}$
- $E^{\text{EM}} < 2.0 \text{ GeV}$

These are similar to the level-3 trigger requirements² with the exception of the electromagnetic (EM) energy cut which was left out of the trigger to prevent biasing analyses which use EM energy information. The muon must have a CTC-measured p_T^μ greater

²Even though the same program is used, quantities calculated offline are better than those calculated in level 3 due to improved calibration constants which take a few days to determine.

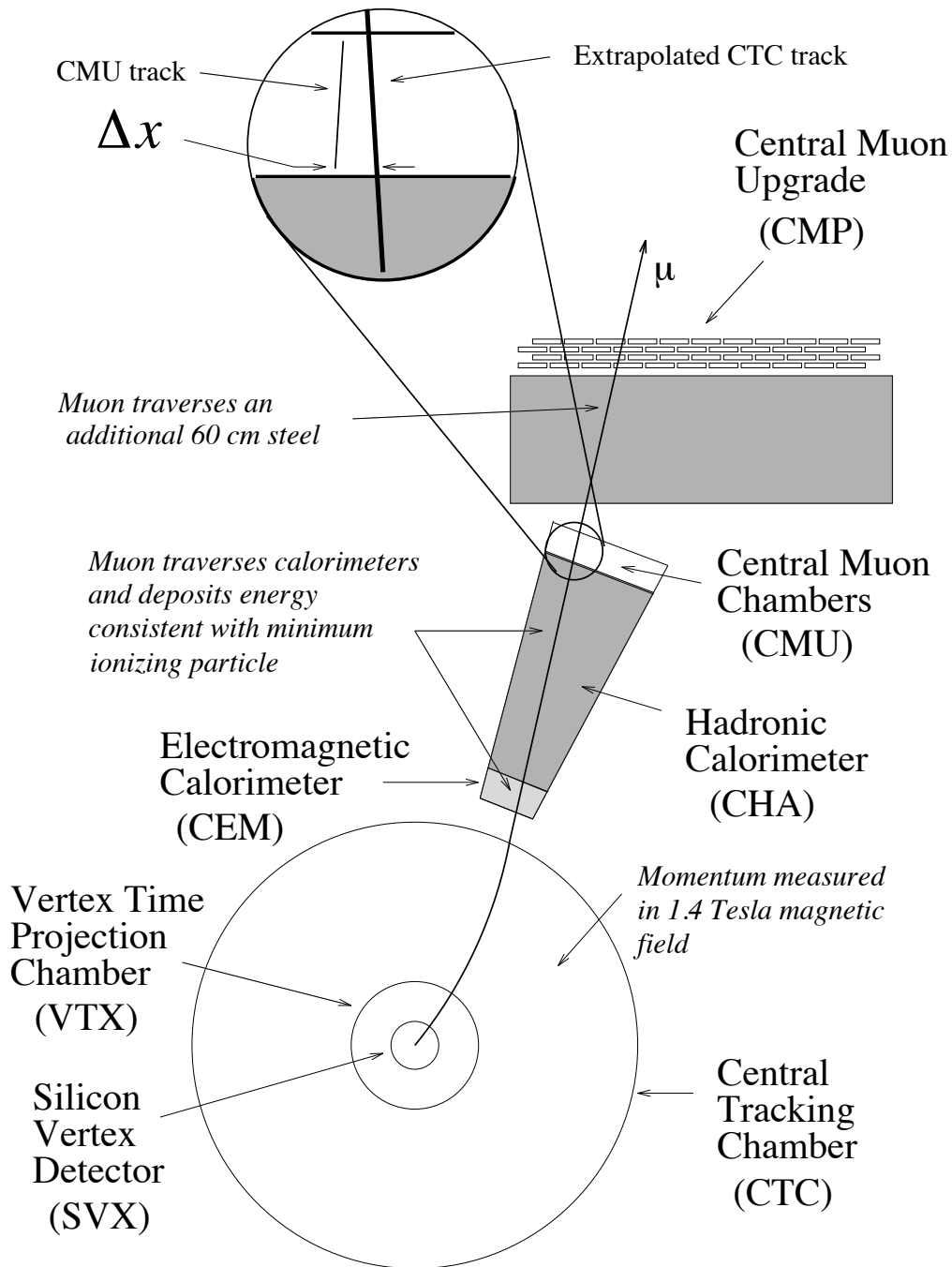


Figure 4.3: The identification of muons. The momentum, p_T^μ , is measured by the CTC. The muon loses energy in the calorimeter (E^{HAD} and E^{EM}). The extrapolated CTC track must match with the track in the muon chambers (Δx).

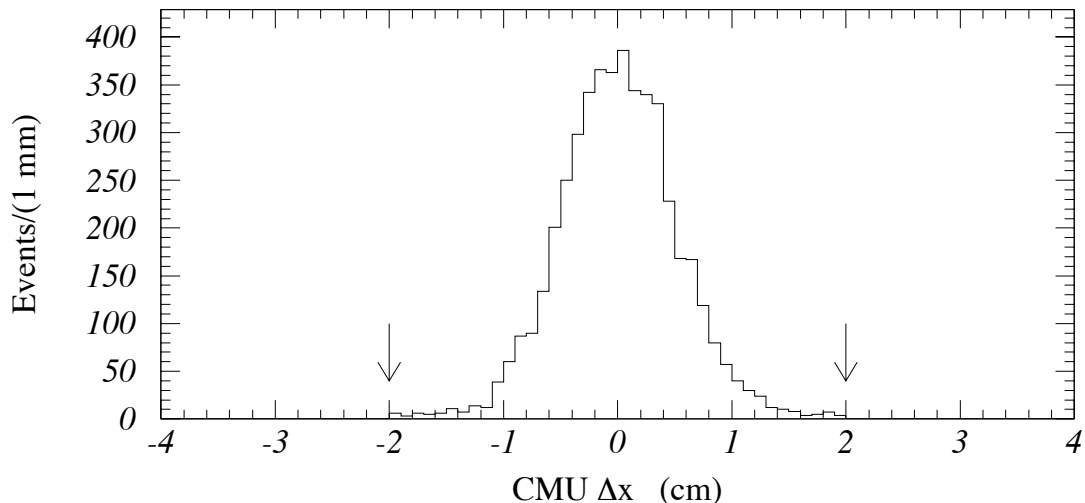


Figure 4.4: The match in the r - ϕ plane between the extrapolated CTC track and the CMU track segment. The arrows indicate the selection cut of 2 cm.

than 18 GeV/c. The CTC track is extrapolated to the muon chambers (CMU) through the electromagnetic and hadronic calorimeters consisting of approximately five hadronic absorption lengths of material. The extrapolated muon trajectory is required to match to a track segment in the CMU (see Section 3.4.1). to within 2 cm in the r - ϕ plane. The RMS spread of this distribution (Figure 4.4) is 0.5 cm, which is consistent with a multiple scattering contribution of 0.3 cm and the CMU alignment. The muon is also required to have left an energy deposit in the calorimeters consistent with that of a “minimum-ionizing” particle³. The energy in the CEM tower(s) traversed by the muon, which is 0.3 GeV on average, must be less than 2 GeV and the energy in the CHA tower(s), which is 2 GeV on average, must be less than 6 GeV. Figure 4.5 shows these energy distributions for the W mass sample. The p_T^μ distribution for this sample is shown in Figure 4.6.

³This is a somewhat qualitative description to distinguish them from hadrons which give up all their energy in the calorimeter; since, strictly speaking, a muon with $p_T > 18$ GeV/c is somewhere on the relativistic rise of the dE/dx curve [34].

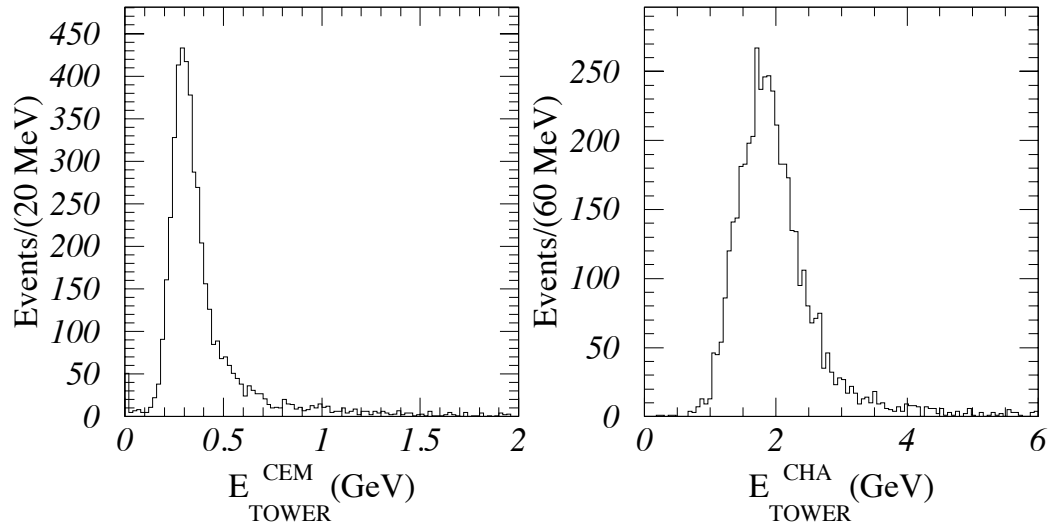


Figure 4.5: Left: Energy distribution in the CEM tower(s) traversed by the muon from W decay. The cut is at 2 GeV. Right: The same distribution for the CHA where the cut is at 6 GeV.

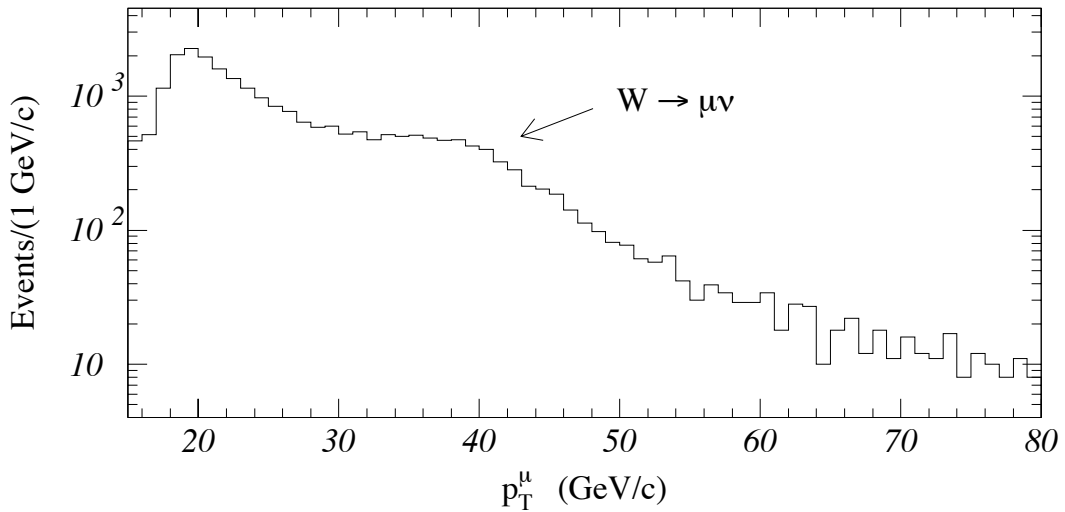


Figure 4.6: The transverse momentum spectrum of inclusive high- p_T muons.

Selection cut	Events Remaining
Initial sample	11748
$ z_{\text{vertex}} < 60$ cm	11127
$p_T^\mu > 25$ GeV/c	7612
$p_T^\nu > 25$ GeV	6797
$ d_o < 0.2$ cm	6155
$ z_{\text{vertex}} - z_{\text{track}} < 2$ cm	5754
No other tracks with $p_T > 10$ GeV/c	4972
No jets with $E_T > 30$ GeV	4839
$ \vec{u} < 20$ GeV	4663
Fit region: $65 < M_T < 100$ GeV/c ²	3268

Table 4.1: Criteria used to select the $W \rightarrow \mu\nu$ sample.

4.4 Neutrino Identification

A W event requires the presence of a high- p_T neutrino to accompany the high- p_T muon. The presence of a neutrino is determined from the missing transverse energy in the event (the balance of $\vec{u} + \vec{p}_T^\mu$). If this missing energy is greater than 18 GeV, then the event contains a neutrino candidate. The exact calculation of the missing transverse energy is given in Chapter 6.

4.5 W Mass Sample

The W mass sample is selected from the “express” data path. In Table 4.1, the selection criteria and the corresponding number of events removed are listed. The event sample selection for the $W \rightarrow \mu\nu$ mass measurement is intended to produce a sample with low background and with well-understood muon and neutrino kinematics. The sample starts with 11748 events which pass the muon and neutrino identification criteria.

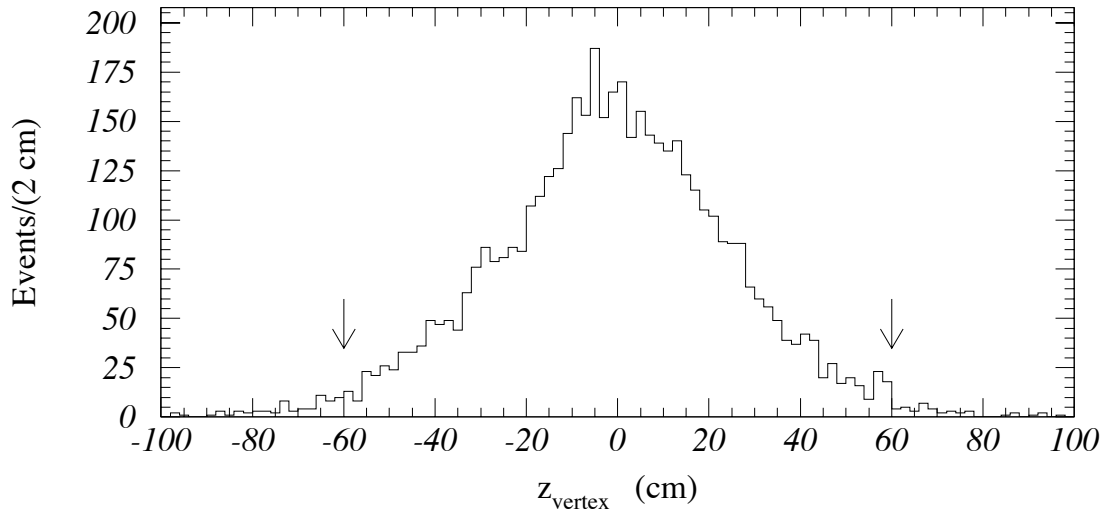


Figure 4.7: The z distribution of VTX-reconstructed vertices closest to the origin of the muon track. The arrows indicate the selection cut of 60 cm.

The event vertex is required to be within 60 cm in z of the origin of the detector coordinates (Figure 4.7). Since there may be more than one reconstructed vertex in the event, either from real overlapping $\bar{p}p$ collisions or from misreconstruction by the VTX, the one closest to the origin of the muon track is used. The z -vertex cut eliminates events where the projective nature of the calorimeters is useless resulting in a systematic mismeasurement of p_T^ν (see Chapter 6), and where particles may escape through the gap between the central and forward calorimeters also leading to an error in p_T^ν .

The transverse momenta of the leptons, p_T^μ and p_T^ν , are required to be greater than 25 GeV/c. This reduces some backgrounds which decrease with increasing p_T (see Chapter 8 and Figure 8.1), while retaining most of the W events which increase with increasing p_T and peak at ~ 40 GeV/c (recall Figure 2.2).

For two reasons, a great deal of care is taken to remove cosmic rays: they decrease slowly with p_T and may be noticeably present above the Jacobian peak where the mass determination is more sensitive to backgrounds; and neither their flux nor the

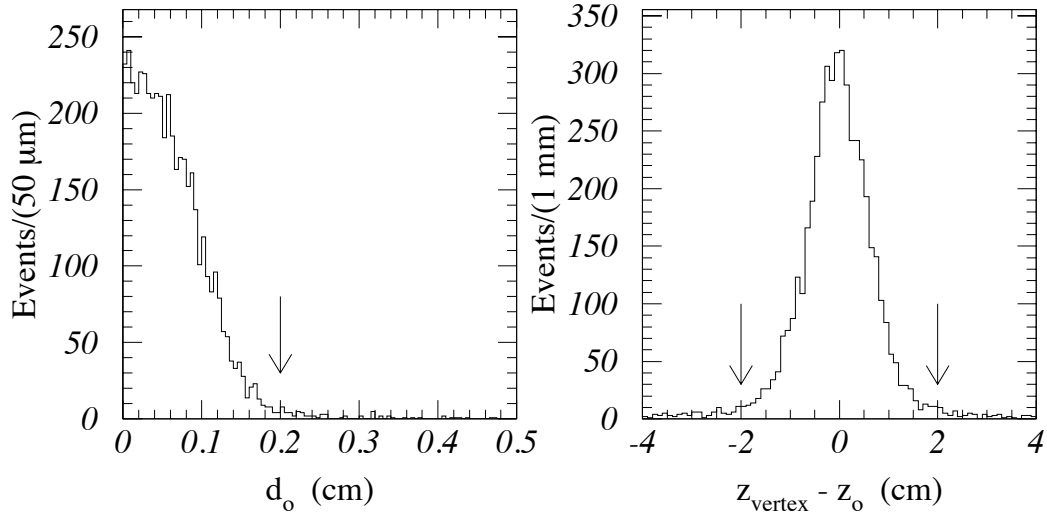


Figure 4.8: Left: The impact parameter distribution for $W \rightarrow \mu\nu$ candidates. Right: The z vertex match to the origin of the track (z_o). The arrows indicate the cut values.

efficiency for detecting them is well known making them difficult to model effectively. Cosmic rays are uncorrelated with the event vertex; thus, the following two cuts are applied. First, the muon track must satisfy $|d_o| < 0.2$ cm, where d_o is the r - ϕ impact parameter with respect to the origin of the detector⁴. Second, the muon track must satisfy $|z_{\text{vertex}} - z_{\text{track}}| < 2$ cm, where z_{track} and z_{vertex} are the z position of the muon track and of the vertex closest to the muon track, respectively. Figure 4.8 shows these distributions. These criteria also remove muons which come from decay-in-flight. Additional cosmic rays and backgrounds from $Z \rightarrow \mu\mu$, which, because of the higher mass of the Z , also do not decrease rapidly with p_T , are reduced by rejecting events with any additional track with $p_T > 10$ GeV/ c . Because cosmic rays are uncorrelated with the events they overlap, the timing information from the CTC, which assumes they are part of the event, can result in either a poor quality track or no track at all,

⁴The r - ϕ beam position and the origin of the detector differ by ~ 0.03 cm. Making this cut with respect to the beam position instead of the origin causes no significant change.

neither of which are removed by the previous additional track requirement. The first case, where one of the two tracks is poorly reconstructed, is looked for by relaxing the criteria used to search for tracks within 2° in ϕ of back-to-back with the muon track. The second case, no track at all, is found by using both the muon detector and the calorimeter opposite in ϕ of the muon track. No events are removed by the poor quality back-to-back track requirement of the first case, indicating that little cosmic ray background remains in the sample. The second case is used to estimate the remaining cosmic ray background which is discussed in Chapter 8.

To further reduce the background from heavy-flavor decays and jets⁵ faking muons, events with a jet with $E_T > 30$ GeV and events with recoil energy $|\vec{u}| > 20$ GeV are rejected. In addition these criteria yield a sample that is easier to simulate, and also keep the events with the best resolution on the transverse mass⁶. The final W sample contains 4663 events, of which 3268 are in the region $65 < M_T < 100$ GeV/ c^2 .

4.6 Calibration Samples

Several data samples are used in calibrating the W mass measurement, as described in Chapters 5, 6, and 7.

$W \rightarrow e\nu$ This data sample is used both in the alignment of the CTC (see Chapter 5) and in the W mass determination from electrons [26, 27]. The selection criteria are described in the references.

⁵A jet is defined as a cluster of energy in the calorimeter within a cone of 0.7 ($\sqrt{\Delta\eta^2 + \Delta\phi^2} < 0.7$). Physically it is the collection of particles resulting from the hadronization of an outgoing quark or gluon.

⁶Since the lepton is measured with a better resolution than the recoil, the ideal event cut would be $|\vec{u}| = 0$ GeV. This would, however, result in zero events and so a compromise is struck.

$Z \rightarrow ee$ This data sample is used to calibrate the calorimeter response to the recoil from the W , \bar{u} (see Chapters 6 and 7.2.3). The selection criteria are described in references [26] and [27].

$J/\psi \rightarrow \mu\mu$ This data sample is used to determine the absolute momentum scale (see Chapter 5). Muons are allowed from all the central muon detectors (CMU, CMP, and CMX) in contrast to the W mass sample which allows only CMU or CMU/CMP. This increases the range of η sampled by the muons thereby increasing the sampled region of the CTC allowing a better determination of systematic errors in the momentum measurement. The initial $J/\psi \rightarrow \mu\mu$ sample is taken from a low- p_T data sample and has the following criteria applied to both muons:

- $p_T^\mu > 1.5 \text{ GeV}/c$
- CMU $\Delta x \ \chi^2 < 16$
- CMU $\Delta z \ \chi^2 < 16$
- CMP $\Delta x \ \chi^2 < 16$
- CMX $\Delta x \ \chi^2 < 16$
- $|z_{vertex}| < 60 \text{ cm}$
- $2800.0 < M_{\mu\mu} < 3400.0 \text{ MeV}/c^2$

The χ^2 cuts are similar to the Δx cut in the W mass sample but take into account multiple scattering by the muon⁷. A sample of $\sim 120,000$ dimuon events is left.

$\Upsilon \rightarrow \mu\mu$ This sample is used to check the momentum scale (see Section 5.3.2) and is chosen with the same cuts as the J/ψ sample except the mass window is moved to $9.0 < M_{\mu\mu} < 11.0 \text{ GeV}/c^2$. This sample contains $\sim 15,000$ events.

⁷The relation between χ^2 and Δx is $\chi^2 = (\Delta x)^2 / \sigma_{MS}^2$ where σ_{MS} is the expected uncertainty in the extrapolated track position due to multiple coulomb interactions in the calorimeter.

Criterion	Events Remaining
Initial sample	1181
$ Z_{\text{vertex}} < 60$ cm	1083
First muon $p_T^\mu > 25$ GeV/c	966
Second muon $p_T^\mu > 25$ GeV/c	928
Second muon traverses all CTC layers	750
$ d_0 < 0.2$ cm for both muon tracks	493
$ z_{\text{vertex}} - z_{\text{track}} < 2$ cm for both muon tracks	415
Two muons not consistent with a cosmic-ray	408
No other tracks with $p_T > 10$ GeV/c	385
No jets with $E_T > 30$ GeV	377
$ \vec{u} < 20$ GeV	359
$76 < M_Z < 106$ GeV/c ²	330

Table 4.2: Criteria used to select the $Z \rightarrow \mu\mu$ sample.

$Z \rightarrow \mu\mu$ This sample is also used to check the momentum scale and in addition to measure the momentum resolution. The cuts and events remaining are summarized in Table 4.2. To maximize the number of $Z \rightarrow \mu\mu$ events, one of the two muons is not required to have a track segment in the muon chambers, increasing the acceptance. The only requirements are that it deposited energy in the calorimeters consistent with that of a high- p_T muon, and that it traversed all the wire layers of the CTC. This latter requirement ensures that both the $W \rightarrow \mu\nu$ and $Z \rightarrow \mu\mu$ samples will have the same momentum resolution, because the momentum resolution depends on the number of CTC layers used in the fit⁸. The jet and recoil-energy cuts are applied to the $Z \rightarrow \mu\mu$ data to reproduce the CTC environment of the $W \rightarrow \mu\nu$ data. Again, this ensures the same momentum resolution in the two samples.

⁸The second muon is not required to have traversed the muon detectors which would have guaranteed that it had traversed all the layers of the CTC.

Chapter 5

Momentum Measurement

This chapter covers five topics: An overview of CTC track reconstruction, the calibration of the CTC drift times, the alignment of the CTC, the determination of the absolute momentum scale using the mass of the J/ψ as a normalization point, and the extraction of the momentum resolution of high- p_T muons from the width of the Z . The momentum measurement is a critical item since not only does it dominate the measurement of transverse mass (recall Equation 2.14), but it is the source of most other calibrations, including the CEM energy calibration used in the electron channel W mass measurement.

5.1 CTC Track Reconstruction

The CTC is operated in a nearly (to within $\sim 1\%$) uniform axial magnetic field enabling charged particle momentum measurements. In a uniform field, charged particles follow a helical trajectory. This trajectory is what the CTC measures directly. The helix is parameterized by: curvature, c (inverse diameter of the circle in r - ϕ); impact parameter, d_0 (distance of closest approach to $r = 0$); ϕ_0 (azimuthal direction at point of closest approach to $r = 0$); z_0 , the z position at the point of closest approach to $r = 0$; and $\cot \theta$, where θ is the polar angle. Nonuniformities in the magnetic field

cause small deviations from a helical trajectory but are absorbed into the five helix parameters by the fitting algorithm. Of these five parameters, the ones which potentially cause systematic errors, either in the W mass measurement, or in the calibration data samples, are curvature and angles. The coordinates of the origin of the track, d_0 and z_0 , do not directly enter into any mass calculation. The possibility of systematic uncertainties in ϕ is eliminated by the condition that ϕ and $\phi + 2\pi$ are physically the same point¹. In this chapter, limits are derived on systematic errors in curvature and $\cot \theta$, with particular emphasis on the former since in the regime of the W decay products it is the dominant error term.

The momentum resolution is improved by using the measured interaction vertex as an additional point in the track fit (“beam-constraint”). Since the momentum resolution scales as $\sim 1/\ell^2$, where ℓ is the distance over which the fit occurs, the beam-constraint offers a factor of two improvement. The z location of the interaction point is determined by the VTX for each event with a precision of 1 mm. The distribution of these interaction points, shown in Figure 4.7, has an RMS spread of 25–30 cm, depending on accelerator conditions. The r - ϕ location of the beam axis is much more stable and, as stated earlier, is measured by the SVX as a function of z with a precision of 10 μm . The beam axis is tilted with respect to the CTC axis by a slope of $\sim 400 \mu\text{m}$ per meter.

The measured momentum of a particle must be corrected for energy lost in the material traversed before entering the CTC. For muons, the dominant loss mechanism is ionization. The correction for this energy loss is negligible for muons from W decay, but is significant for those used in the determination of the J/ψ mass, to which the momentum scale is normalized (see Section 5.3).

¹If one claims an error in ϕ such that $\phi \rightarrow \epsilon\phi$, one is faced with the impossibility of one physical point, say $\phi = 0 = 2\pi$, being split into two separate points, $\phi = 0$ and $\phi = \epsilon 2\pi$

5.2 CTC Calibration and Alignment

5.2.1 CTC Calibration

The CTC calibration determines the relationship between the measured drift time and a position relative to the sense wire. Averaged over ϕ , calibration errors do not contribute directly as a systematic error in momentum. They enter as an apparent shift in the wire positions, equivalent to an alignment error, but one which may vary with momentum (see Section 5.2.2). This is one potential source of non-linearity in the momentum scale; however, since the linearity will be explicitly checked later, the calibration is described only briefly.

Calibration of the drift properties is done in several steps. First, periodic electronic pulsing gives relative time offsets for each channel. Second, on-line reconstruction of $\bar{p}p$ data is used to track variations in the drift properties of each super-layer and additional corrections for non-uniformity in the drift trajectories are made based on this data. Finally, a global time offset is found by combining information from all tracks originating from a common vertex. The end result is a drift-distance resolution of 170 (outer layers) to 220 μm (inner layers), to be compared with $\sim 120 \mu\text{m}$ expected from diffusion alone, and $\sim 200 \mu\text{m}$ resolution expected from test chamber results.

5.2.2 CTC Alignment

Throughout this section, averaging over ϕ is relied upon to eliminate many errors; however, the trigger is not perfectly uniform in phi, resulting in slight differences in the ϕ distributions of the various data samples. Each potential ϕ dependent error is verified to be small; but after this, it is dropped from further consideration until the end when ϕ dependence is checked explicitly.

The alignment consists of three parts. First, a limit is set on the single wire alignment, i.e. the displacements of individual wires from the nominal CTC construction

positions. Second, a layer alignment is performed, which consists of the coherent rotation about the z axis of all wires in a cylindrical layer. Third, corrections are applied directly to the helix parameters (global alignment) to remove residual misalignments left by the layer alignment.

5.2.2.1 Single Wire Alignment

In ϕ , CTC super-layers are divided into “cells,” with each axial (sterco) cell consisting of 12 (6) sense wires (recall Figure 3.2). Both sense and field-shaping wires are positioned by precision guide rods attached to each endplate. Each cell has one rod for the sense wires (anodes), and two rods shared with the neighboring cells for the field-shaping wires (cathodes). Each guide rod was surveyed before being used and the wire positions were held to a tolerance of $\sim 10 \mu\text{m}$, leading to a conservative limit on the RMS scatter of $10\mu\text{m}/\sqrt{12}$, or $< 3 \mu\text{m}$. Averaged over ϕ , these random displacements in individual wire positions result in resolution broadening, but introduce no systematic error. The positions of the guide rods were surveyed optically before assembling and stringing the chamber. An RMS scatter of $\sim 25 \mu\text{m}$ was found. This scatter of guide rod locations is much larger than the scatter of individual wires within the guides. In addition, error in the guide position is correlated over many wires whereas errors in the groove positions affect each wire independently. Thus, a $25 \mu\text{m}$ cell-wide scatter is used as the baseline when checking the ϕ dependence of the alignment.

5.2.2.2 Layer Alignment

The layer alignment consists of a z -dependent correction to the ϕ position of the wires in a layer. The mechanical model is an independent rotation of each layer, independently at each endplate, while keeping the radius fixed resulting in two parameters per layer minus one overall phase for a total of 167 parameters. Since the alignment is expected to

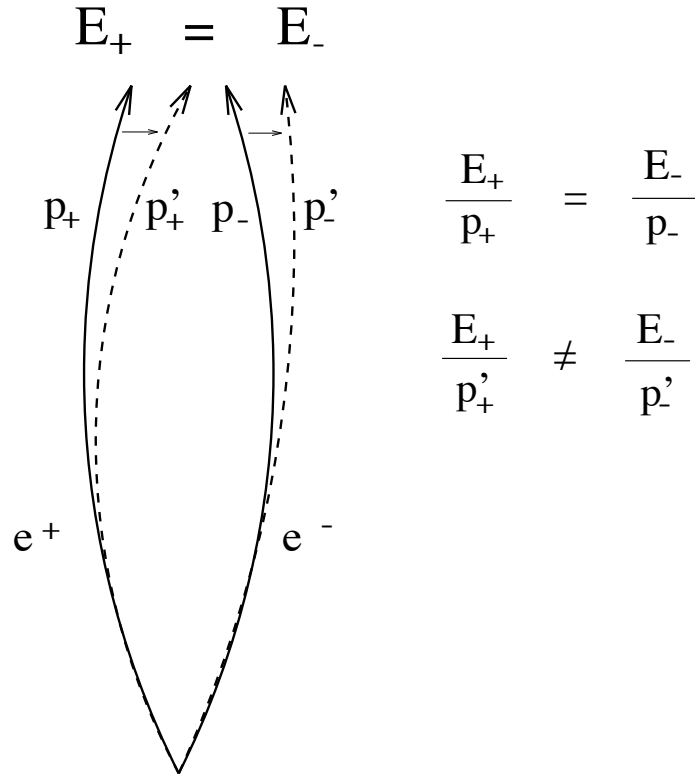


Figure 5.1: Diagram showing the effect of layer rotation on the measured momentum. With an ideal alignment, the momentum of a positron, p_+ , equals the momentum of an electron, p_- , if they have the same energy. Rotated layers produce a shift in the measured momentum: up(down) for positive charges, down(up) for negative charges ($p'_+ \neq p'_-$).

absorb systematic calibration errors, this mechanical model is not taken too seriously; in particular no constraint is imposed on the implied distortion of the wire guide rods.

The alignment is performed by requiring a positron and electron of the same energy as measured by the CEM to have the same momentum as measured by the CTC. This takes advantage of the charge-independent response of the CEM to electrons. This approach is termed an “ E/p alignment” since the average ratio of E/p for electrons and positrons is constrained to be equal (Figure 5.1). Note that it is *not* necessary for the CEM energy to be correct, only that it be charge-independent.

A sample of >10,000 electrons with $E_T > 18$ GeV is used to do the alignment. The helix parameters (Section 5.1) are constrained to:

- Originate from the primary vertex (in z) as identified by the VTX
- Originate from the beam spot (in r - ϕ)
- Have $p_T = \alpha E_T$, where p_T is from the CTC and E_T is from the CEM. The scale factor α is used to bypass the absolute CEM energy scale, which is unknown at this point in the calibrations.

All five parameters are adjusted to meet these constraints, but to a good approximation z_0 and d_0 are fixed by the beam-constraint, and curvature is set by the $p_T = \alpha E_T$ requirement. Only $\cot \theta$ and ϕ_0 are left as the two free parameters for which the track is refit. Using the new helix parameters, the residual (expected drift distance minus measured drift distance) is calculated at each layer. An average is taken over many events, separately for positives and negatives. An incorrect alignment results in a splitting of the residuals between electrons and positrons. The difference between the two residuals gives the misalignment. The procedure is iterated until all layers are stable to $0.1 \mu\text{m}$. The measured deviation of each layer from its nominal position is shown in Figure 5.2.

Returning to the basic idea of equal momenta for equal energies, there are many physical deformations that can be applied to the CTC which would still allow this on average. This fact implies several degrees of freedom which are not pinned down by the alignment procedure and leaves open two sources of systematic errors: real, mechanical displacement of the wires; or an introduction of errors by the alignment procedure because it can't constrain the other degrees of freedom. Possible transformations are discussed below (Figure 5.3).

Offset The origin of the CDF coordinate system is arbitrary, so any overall offset (Figure 5.3a) has no affect.

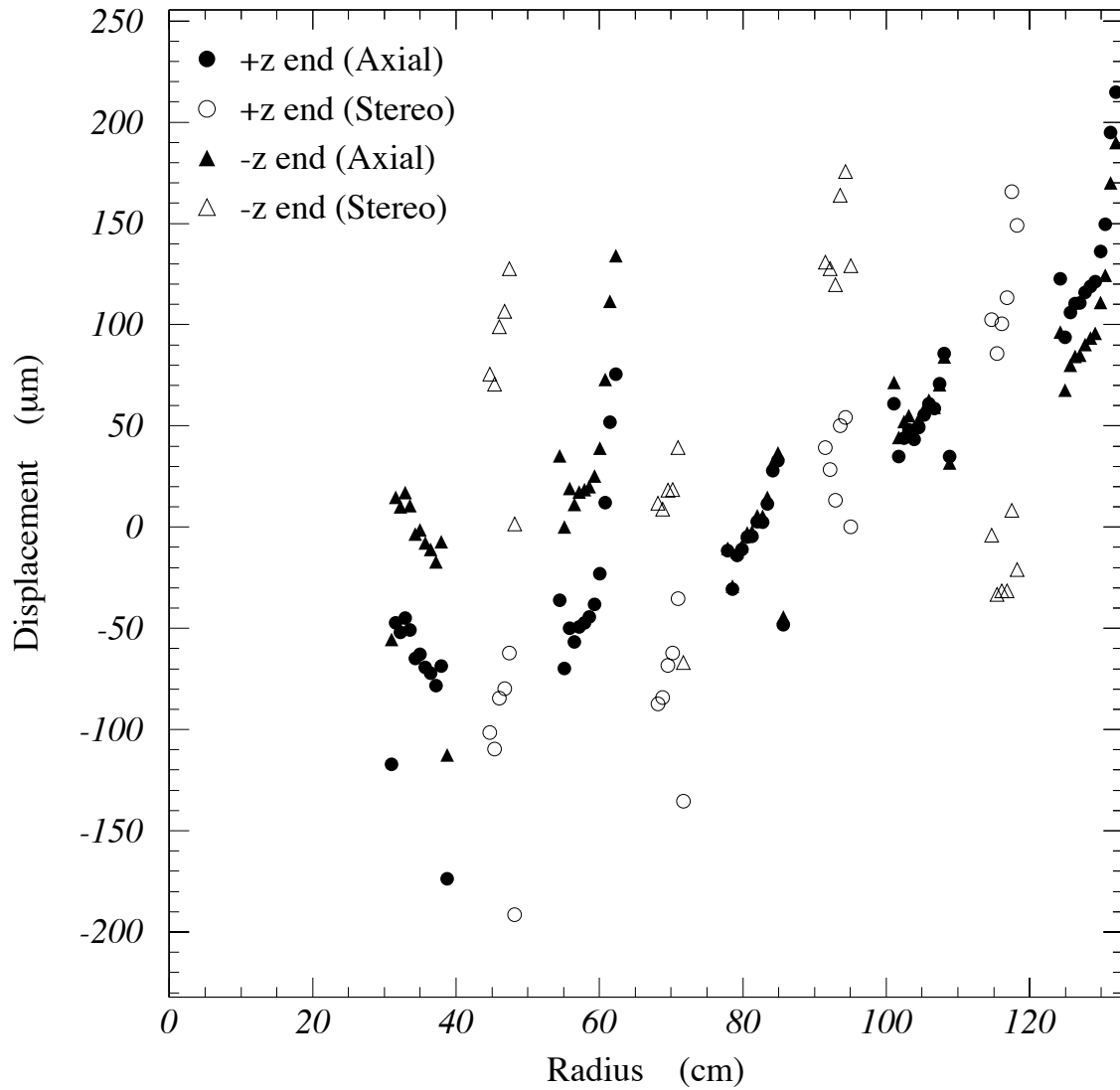


Figure 5.2: Deviation of wires ($r\Delta\phi$) from their nominal positions as a function of radius. Recall that each end of the wire is allowed to rotate independently. Circles are one end of the CTC ($z = +150$ cm) and triangles are the other end ($z = -150$ cm).

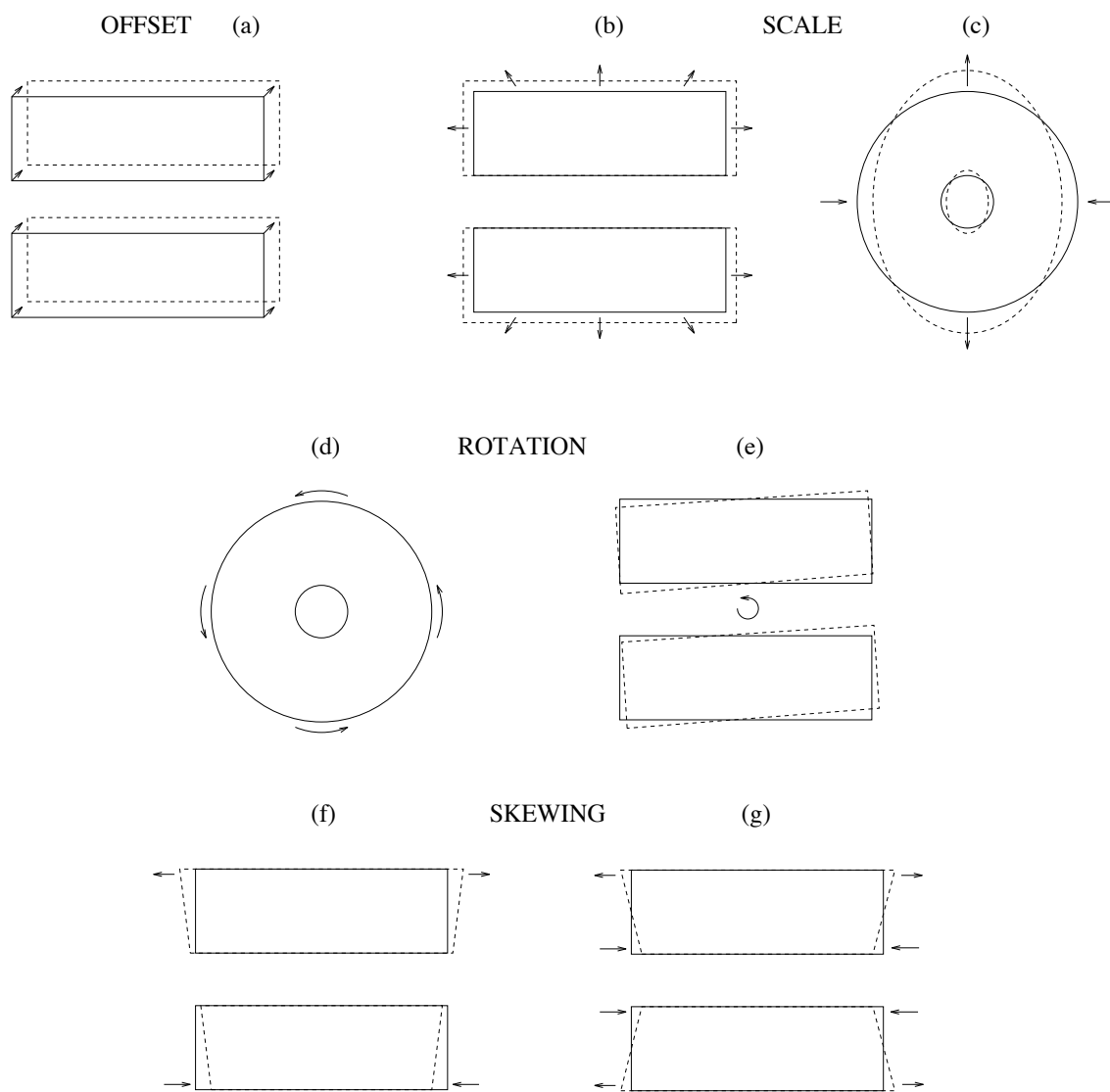


Figure 5.3: Transformations of the CTC. Upper Left: Translation of the CTC (a). Upper Right: Scaling the CTC by (b) $r \rightarrow \beta r$ and (c) $\rho \rightarrow \beta(\phi)\rho$. Middle: Rotations in (d) r - ϕ and (e) r - z . Lower: Skewing the CTC in r - z by (f) tilting the endplates and (g) conically deforming the endplates.

Scale A global scale factor on the size of the CTC (Figure 5.3b) scales the curvature and therefore momentum and is absorbed in the momentum-scale calibration.

The scale in z is set, via the z_0 component of the beam constraint, by the VTX. The VTX was aligned to the CTC and hence shares the same origin. The scale, however, is set by the length of the VTX modules, which were surveyed to a precision of $\sim 200 \mu\text{m}$ over a 150 cm length. The potential scale error is a part in 10^4 . Since z enters into mass calculations only via $\cot \theta$, and the potential error from skew is larger (see below), the z -scale error is ignored.

The endplate of the CTC could be elongated such as to map a circle in r - ϕ to an ellipse (Figure 5.3c). This is similar to a ϕ dependent scale on momentum and $\cot \theta$; however, the cylindrical symmetry of the CTC at the time of construction rules out the introduction of any significant systematic distortion of this kind. Furthermore, recall that averaging over ϕ serves to eliminate any systematic effects.

Rotation A overall rotation in ϕ (Figure 5.3d) has no effect since the orientation of $\phi = 0$ is arbitrary.

A tilt to the CTC axis relative to the magnetic field axis, i.e. a rotation in the r - z plane (Figure 5.3e), does affect momenta. The alignment procedure intrinsically keeps the z axis fixed, and so cannot introduce (or remove) this error. The affect of such a tilt would be a coupling between curvature, ϕ_0 , and $\cot \theta$. No such behavior has been found and since averaging over ϕ removes this effect, it is ignored.

Skew Skew in the r - z plane implies a tilt of one or both endplates (Figure 5.3f). This was checked by optical survey of the endplates before stringing. Distortion of this kind occurring after construction is unlikely from the cylindrical symmetry of the chamber and in addition, the presence of a distortion would result in a scale error on z which again can be limited by the VTX (see Scale above).

Since all tracks emanate from near the center of the CTC (± 60 cm; recall Figure 4.7), another form of skew is possible which does not result in a scale error on z and can be pictured as a conical distortion of the endplates (Figure 5.3g). This leads to a scale error only on $\cot \theta$ and thus cannot be ruled out by the VTX. If the distortion is not the same at both endplates, $\cot \theta$ also has an offset which varies linearly with z_0 . These distortions could occur after construction and so cannot be ruled out by the optical survey. It is difficult to dis-entangle such a skew from the alignment required to avoid charge-dependent curvature. Since an error of this kind is possible, it will need to be looked for separately. Therefore, no attempt was made to prevent the layer alignment from contributing to the skew; instead, both the real skew and any artifact from the alignment are removed as part of the global alignment.

5.2.2.3 Global Alignment

After the above procedure, a scale error on $\cot \theta$ is left as the only alignment effect that is not zero when averaged over ϕ . The large sample of $J/\psi \rightarrow \mu\mu$ events is used to measure this, and a correction is applied directly to the helix parameters. The statistical uncertainty on the layer positions can also leave residual charge asymmetry. This asymmetry is determined from $W \rightarrow e\nu$ events and again, corrections are applied directly to the helix parameters.

Figure 5.4 shows the measured J/ψ mass as a function of $\Delta \cot \theta$ of the two muons. Details of the J/ψ mass measurement are given in Section 5.3. The variation is minimized by adjusting $\cot \theta$ as

$$(\cot \theta)_{\text{corrected}} = 0.999 \cot \theta. \quad (5.1)$$

The beam position, initially measured run-by-run using the SVX, is corrected for a $25 \mu\text{m}$ offset corresponding to a misalignment between the CTC and SVX. This is

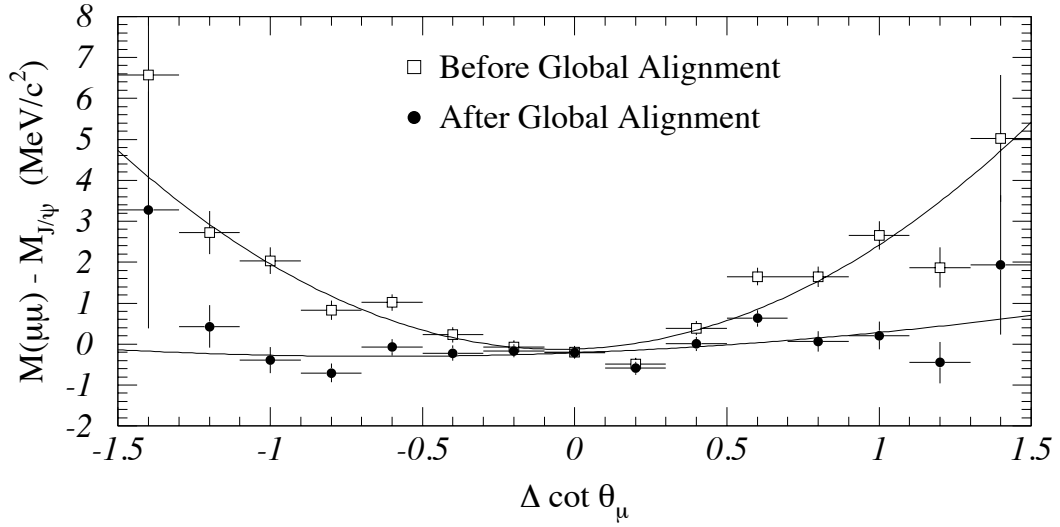


Figure 5.4: Variation of the J/ψ mass with $\Delta \cot \theta$ before and after the correction of Equation 5.1. (see Equation 5.4 for the mass dependence on $\cot \theta$).

implemented as

$$\left(\frac{1}{p_t}\right)_{\text{corrected}} = \frac{1}{p_t} - 0.00025q \sin(\phi_0 + 3.6\text{rad}) \quad (5.2)$$

where $q = \pm 1$ is the charge and ϕ_0 is in radians. Figure 5.5 shows the difference in E/p for positrons and electrons vs ϕ before and after the global alignment.

A residual, θ -dependent charge asymmetry is left after the layer alignment and is reduced by applying the correction

$$\left(\frac{1}{p_t}\right)_{\text{corrected}} = \frac{1}{p_t} - 0.00035q(\cot \theta + z_{\text{vertex}}/187\text{cm}) \quad (5.3)$$

where $q = \pm 1$ is the charge and z_{vertex} is measured in centimeters. Figure 5.6 shows the difference in E/p for positrons and electrons versus $\cot \theta$ before and after the global alignment. Figure 5.7 shows the E/p distribution after all corrections. The difference

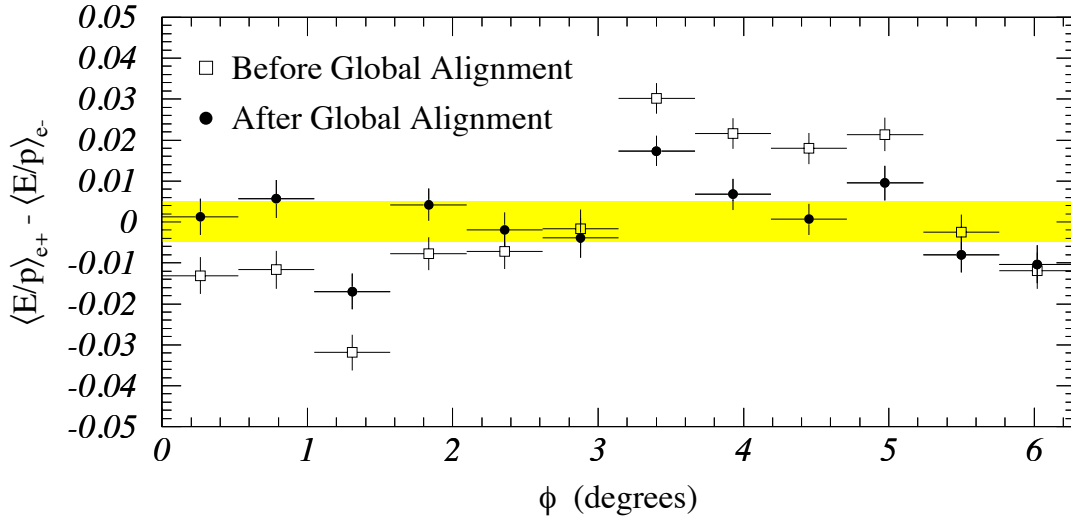


Figure 5.5: The variation in ϕ of the difference in E/p between electrons and positrons. The shaded area indicates the expected variation from the $25\ \mu\text{m}$ RMS scatter of the wire guide rods (see Section 5.2.2).

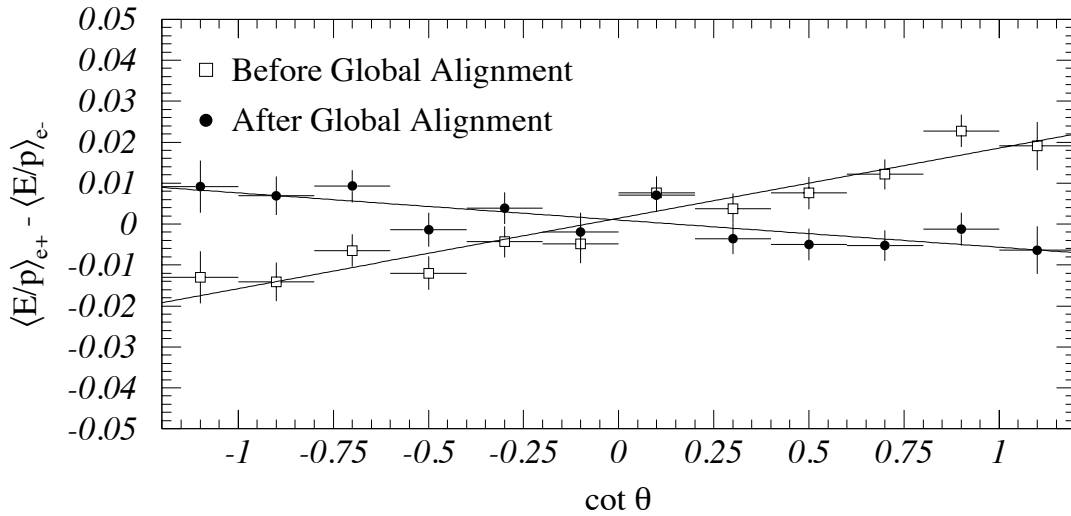


Figure 5.6: The variation in $\cot \theta$ of the difference in E/p between electrons and positrons.

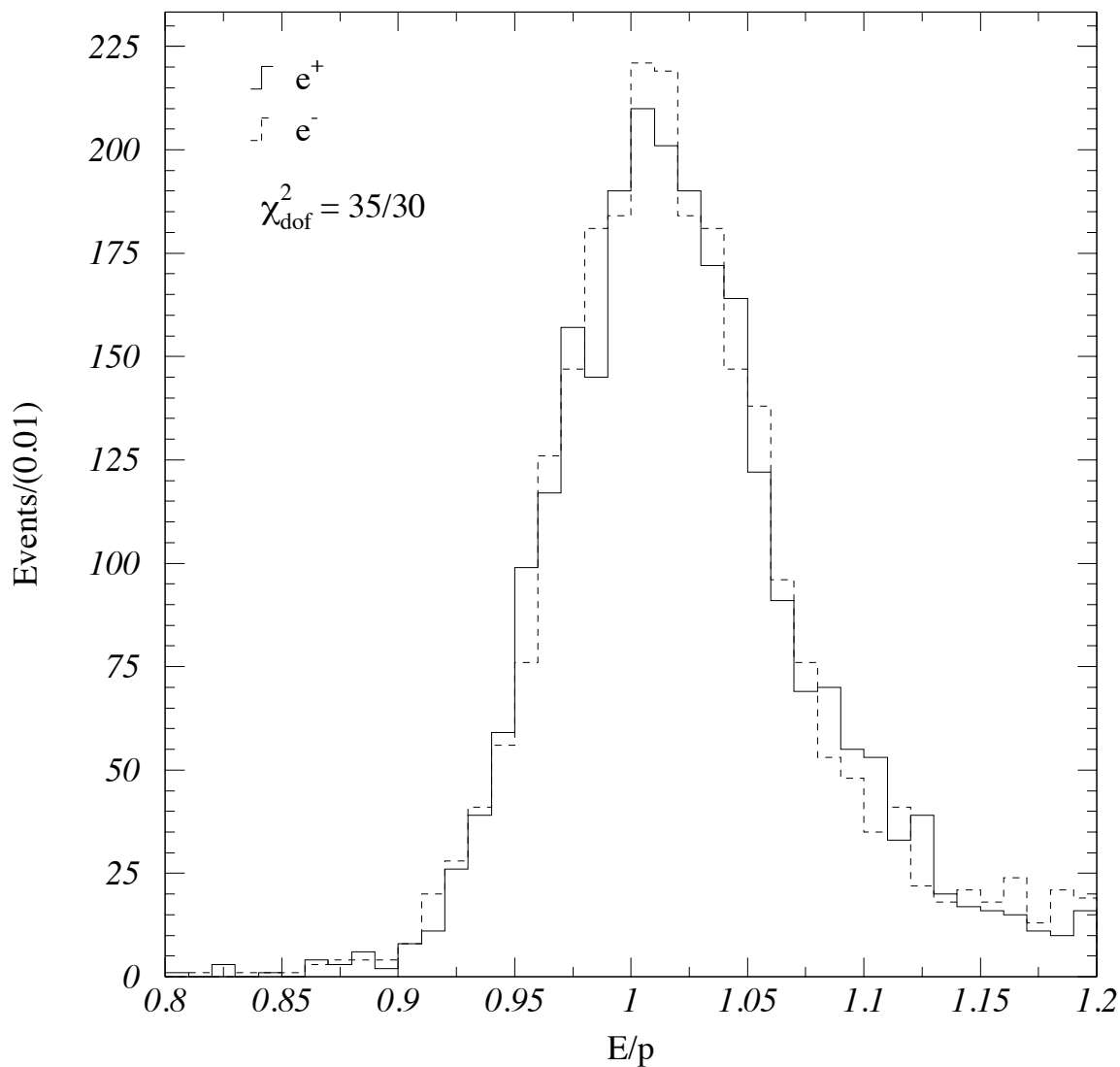


Figure 5.7: The distribution of E/p , after all corrections, for positives and negatives. The tail on the right is caused by energy loss from brehmmstrahlung. This tail is used to measure the amount of material between the beam and the CTC. The difference in the means of these two distributions is consistent with zero to better than a part in 10^3 .

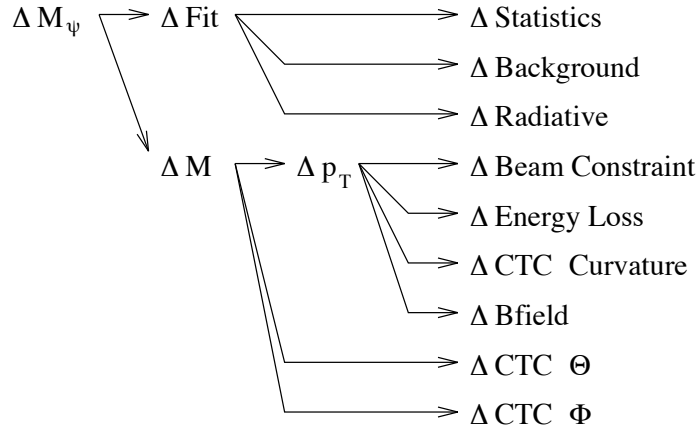
between positives and negatives is less than one part in 10^3 which is taken as the upper limit on the average misalignment.

5.3 Absolute Momentum Scale

The momentum scale is determined by normalizing the observed $J/\psi \rightarrow \mu\mu$ peak to the world-average mass [35]. The masses of the first three lowest states of the Υ and the mass of the Z boson function as checks.

5.3.1 Determination of J/ψ Mass

The invariant mass spectrum of 60,000 muon pairs from J/ψ decay is shown in Figure 5.8. The J/ψ mass measurement consists of determining individual event masses (the invariant mass of the muon pair; see Equation 5.4) and fitting the resulting distribution. The uncertainty in the measured J/ψ mass can be broken down into these sources:



The values of these uncertainties are given in Table 5.1 with the exception of the following: the systematic error in ϕ , which, as stated earlier, cannot exist when averaged over all of ϕ since 0 and 2π are the same point; and the error in curvature which is

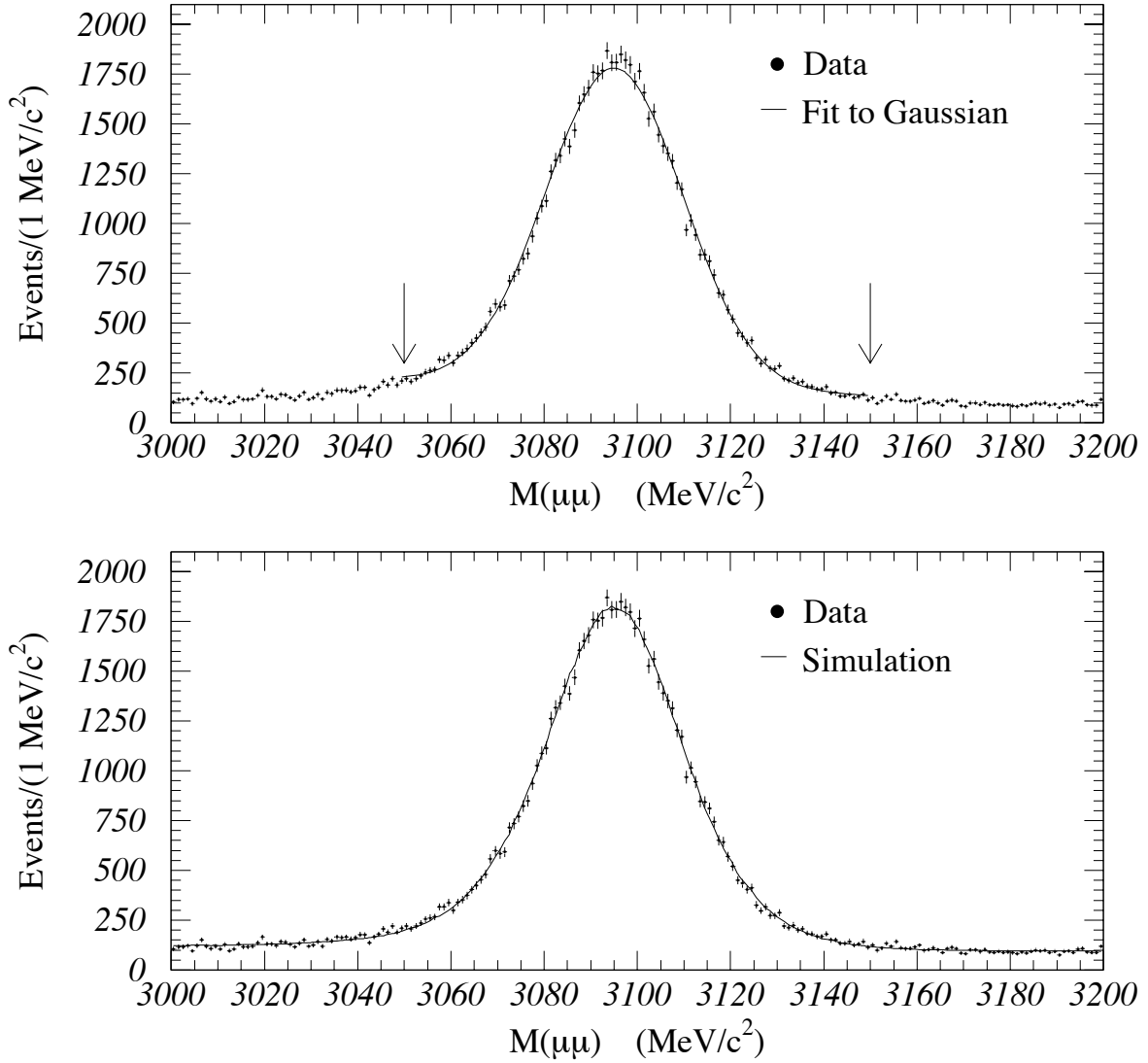


Figure 5.8: The dimuon mass spectrum from the data, points, near the J/ψ mass in a $200 \text{ MeV}/c^2$ window. Upper: The curve is a Gaussian fit with a linear background in a $100 \text{ MeV}/c^2$ window. The arrows indicate the fit region. Lower: The curve is a Monte Carlo simulation including radiative effects.

Effect	Uncertainty (MeV/c ²)
Statistics	0.1
Background	0.1
Radiative decay	0.2
Beam-constraint	0.3
Muon energy loss before tracking	1.2
Residual field non-uniformity	0.6
Opening polar angle effect	—
Time variation	0.5
Uncertainty in World-Average $M_{J/\psi}$	0.1
Extrapolation from $M_{J/\psi}$ to M_W	0.9
TOTAL	1.7

Table 5.1: Systematic uncertainties on the measurement of the J/ψ mass, used to set the momentum scale for muons from W decays. The tabulation includes the uncertainty incurred when extrapolating from tracks associated with J/ψ decays to those associated with W decays.

discussed, along with the extrapolation to the W mass, in Appendix B. Additional uncertainties are included in the table to account for an unexplained time variation and the extrapolation from the momenta characteristic of J/ψ decay to the momenta of muons from W decay. The latter relates only to the use of the J/ψ mass as a normalization point; however, it is expressed in terms of an uncertainty on the J/ψ mass. The entries in the table are described below in the order they appear.

Statistics The J/ψ data are fit with a Gaussian plus a linear background in a 100 MeV/c² window centered on the world-average mass. The kinematic point at which the mass is obtained is described later in this section under the Polar Opening Angle uncertainty. The fit determines the mean with a statistical accuracy of 0.1 MeV/c². Fits using wider windows yield shifts in the mass consistent with expected shifts due to the radiative tail.

Background The error in the measured J/ψ mass due to the uncertainty in the background shape is estimated by fitting both linear and quadratic background shapes to the data. It is found to be less than $0.1 \text{ MeV}/c^2$.

Radiative Decay The measured mass must be corrected for QED radiative effects in J/ψ decay. The correction is determined using Monte Carlo simulation (see Figure 5.8) to be $0.56 \pm 0.20 \text{ MeV}/c^2$.

Beam Constraint Since a significant fraction of J/ψ mesons come from decays of B mesons, which decay some distance from the primary vertex, the measured J/ψ peak may be shifted by the application of the beam constraint (Figure 5.9). This is checked for, along with any other error contributions from the beam-constraint, by observing the shift in the J/ψ mass between a fit using the beam constraint and a fit that only constrains the two muons to originate from the same point. A difference of $0.3 \text{ MeV}/c^2$ is seen and is taken as an uncertainty.

Muon Energy Loss The momentum of each muon is corrected for energy loss in the material traversed by the muon prior to the CTC (Section 5.1). This correction corresponds to a shift in the measured J/ψ mass of $3.7 \text{ MeV}/c^2$. The amount of material is measured in radiation lengths from the high tail of the E/p distribution for W electrons (Figure 5.7) and is checked by counting the number of photon conversions to electron-positron pairs as a function of position in the detector (Figure 5.10). For a given radiation length, the muon energy loss is dependent on the type of material. The uncertainty introduced into the measured J/ψ mass is calculated from the uncertainty in the number of radiation lengths and from the uncertainty in the type of material and is determined to be $1.2 \text{ MeV}/c^2$.

Residual Field Non-Uniformity The variations of the magnetic field both in magnitude and direction are small within the CTC active volume; $|\vec{B}(\vec{r}) - B(0) \hat{z}|/B(0)$

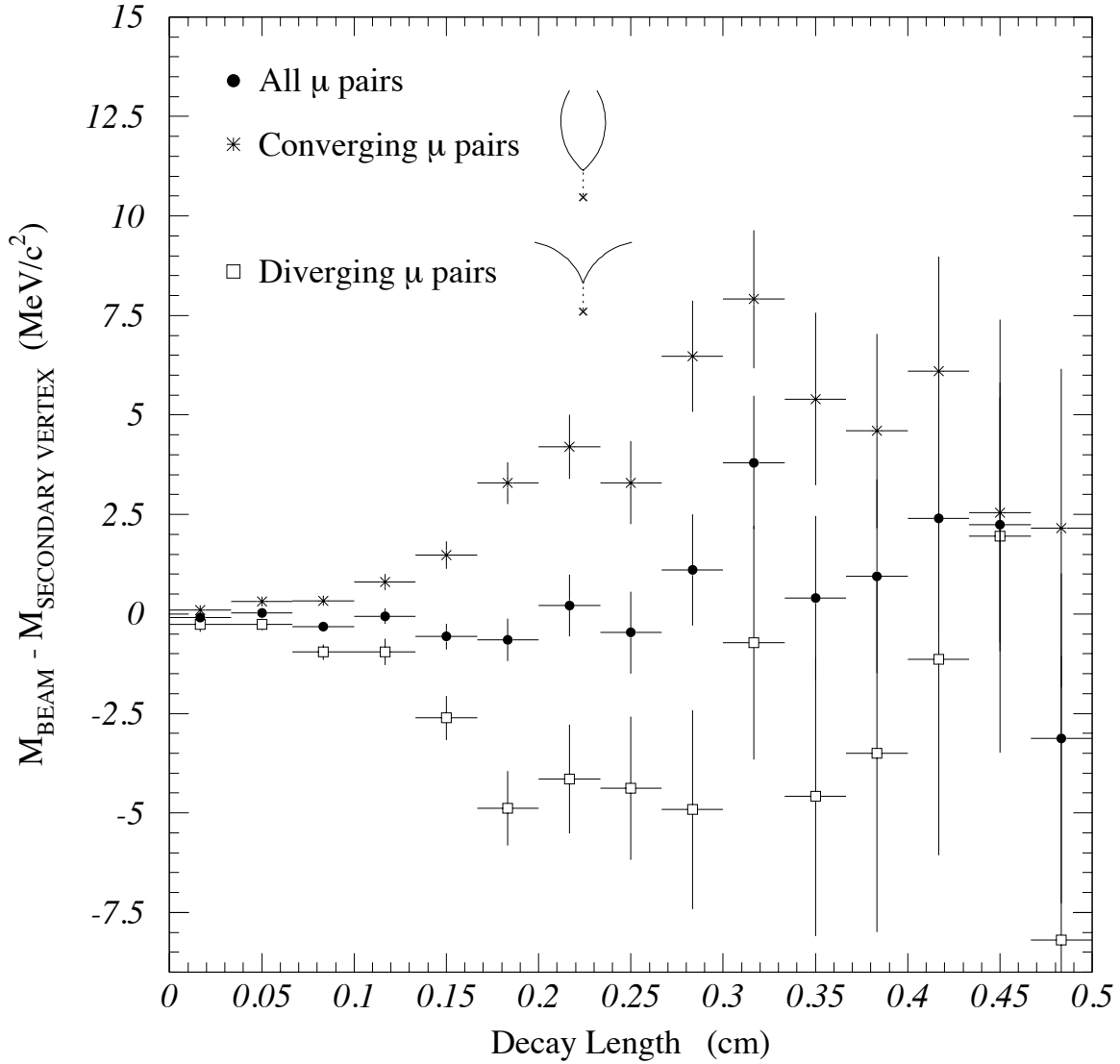


Figure 5.9: The shift in the fit J/ψ mass as the true decay vertex moves away from the constraining vertex. While the mass for diverging tracks shifts substantially from that for converging tracks, the average remains close to zero.

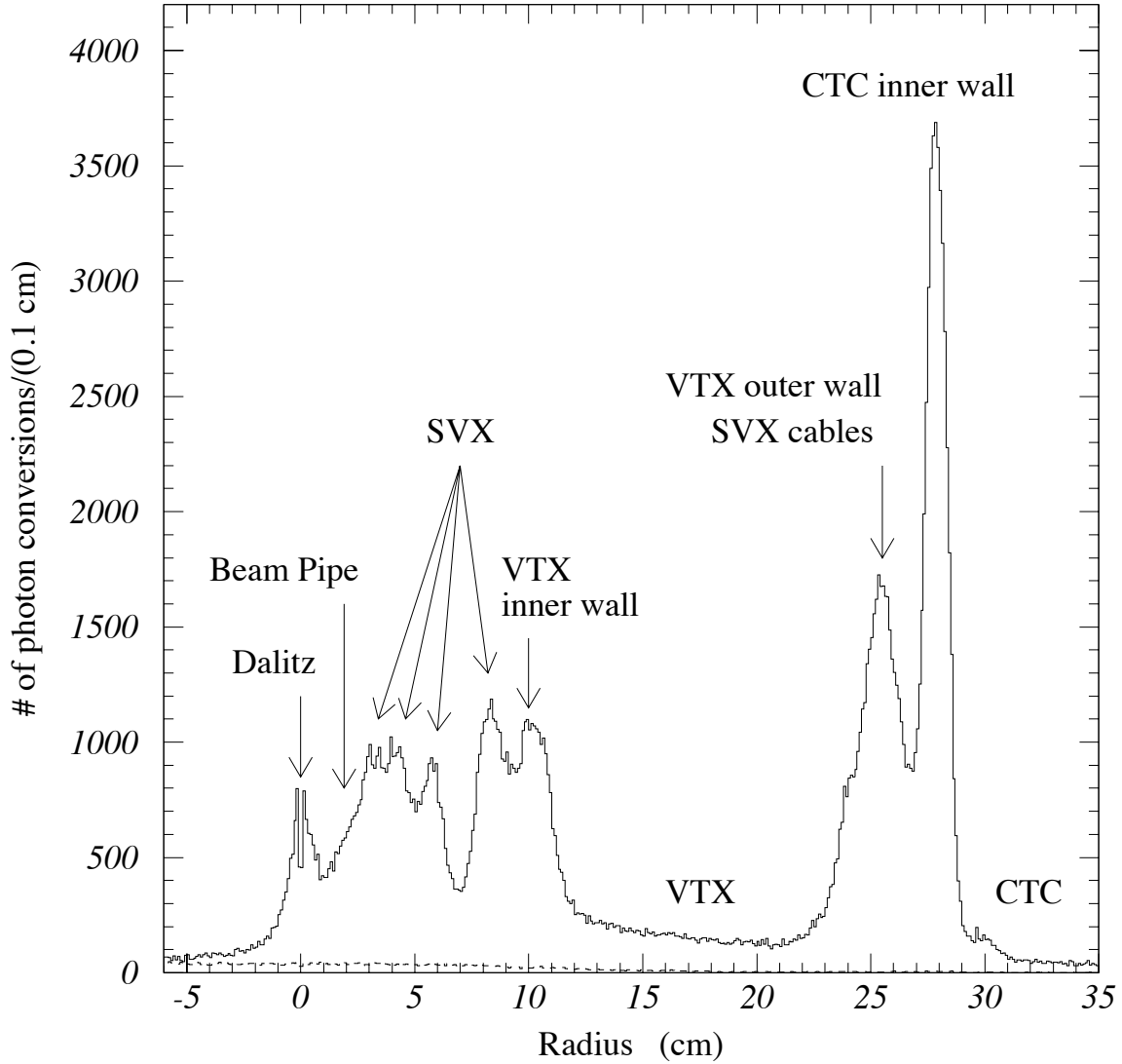


Figure 5.10: The number of photon conversions to electron-positron pairs as a function of radius from the beamline. The major features of the CDF detector are labeled. The amount and type of material in the CTC inner wall is precisely know, allowing one to calibrate the other sources of material. The dashed line is the background.

is, at most, a few percent occurring at the outer radius of the endplates of the CTC (see Figure 5.11). In 1986, the magnetic field was mapped using a rotating search coil at a solenoid current of 5000 A with a few additional points at 4500 A [36]. However, during the data-taking period, the solenoid current was 4650 A. Due to saturation in the iron return yoke, the magnetic field is not exactly proportional to the solenoid current. Using a model of the iron structure and its saturation properties, the 5000 A data have been extrapolated to 4650 A. As a check, a similar extrapolation to 4500 A is made and the agreement is consistent within the measurement uncertainties of 2×10^{-4} T. The largest deviation from a simple scaling by 4650/5000 is less than 0.3%, occurring near the outer edge in radius and z of the CTC. The correction to $\int \vec{B} \cdot d\vec{\ell}$ is almost always less than 0.1% as shown in Figure 5.11. Because the field is symmetric in z , residual non-uniformities are looked for in the variation of the J/ψ mass with $\Sigma z^2 = z_{\mu+}^2 + z_{\mu-}^2$, where z is the track position at a radius of 100 cm². The mass is plotted as a function of Σz^2 in Figure 5.11 and the data are fit to a line. The difference across the fit region is 0.6 MeV/c², which is taken as an uncertainty on the J/ψ mass.

Polar Opening Angle Recall that before applying Equation 5.1, a dependence of the measured J/ψ mass on the opening polar angle ($\Delta \cot \theta$) between the two muons was observed (Figure 5.12). Because the purpose here is to extract a momentum scale, this sensitivity to angular systematics must be reduced. Writing invariant mass (ignoring the muon mass) in terms of $\cot \theta$,

$$M^2 = 2p_{t1}p_{t2} \left[\sqrt{1 + \cot^2 \theta_1} \sqrt{1 + \cot^2 \theta_2} - \cot \theta_1 \cot \theta_2 - \cos \Delta \phi \right], \quad (5.4)$$

one notes that when $\cot \theta_{\mu+} = \cot \theta_{\mu-}$, the invariant mass is not dependent on $\cot \theta$.

²The point in a track most sensitive to magnetic field variations is at a radius of 100 cm.

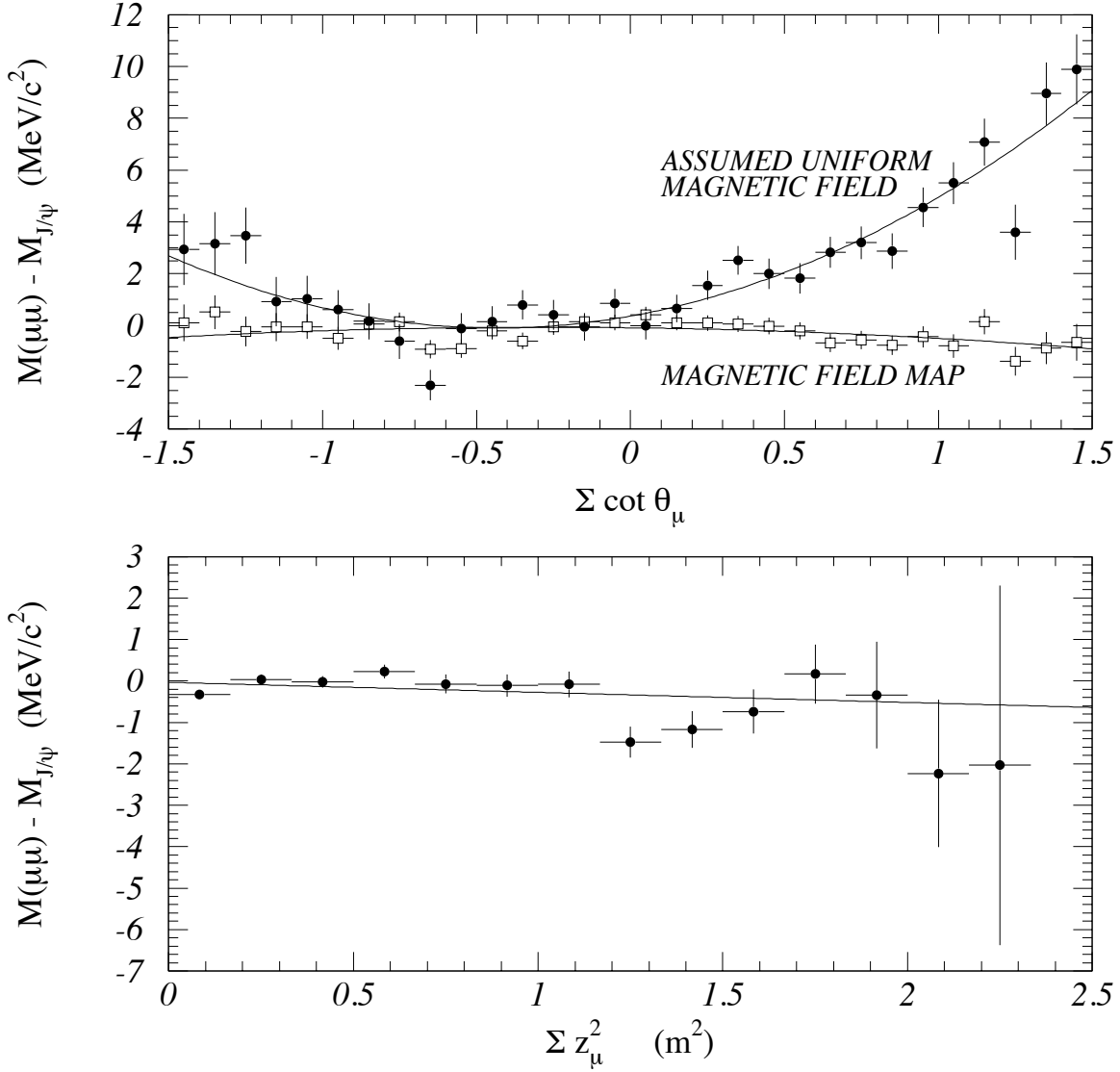


Figure 5.11: Upper: The variation of the measured J/ψ mass with $\cot \theta_{\mu+} + \cot \theta_{\mu-}$ both with (open) and without (solid) the magnetic field map. Lower: The variation of the measured J/ψ mass with $\Sigma z^2 = z_{\mu+}^2 + z_{\mu-}^2$ where z is measured at a radius of 100 cm.

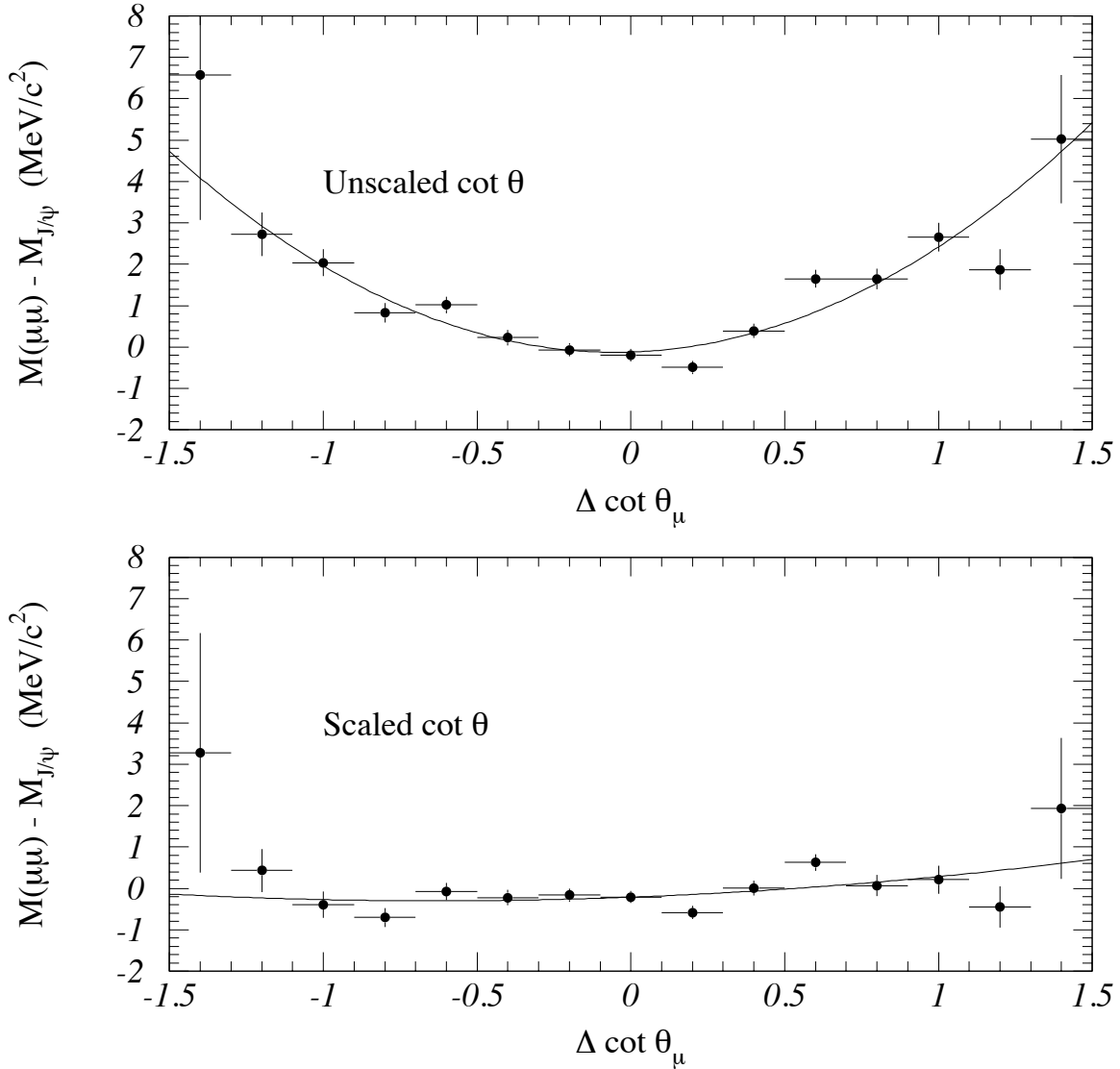


Figure 5.12: The measured J/ψ mass versus $\Delta \cot \theta$. Upper: Before scaling $\cot \theta$. Lower: After scaling $\cot \theta$. The fit value at the kinematic point of $\Delta \cot \theta = 0$ is the same (within statistics) before and after scaling.

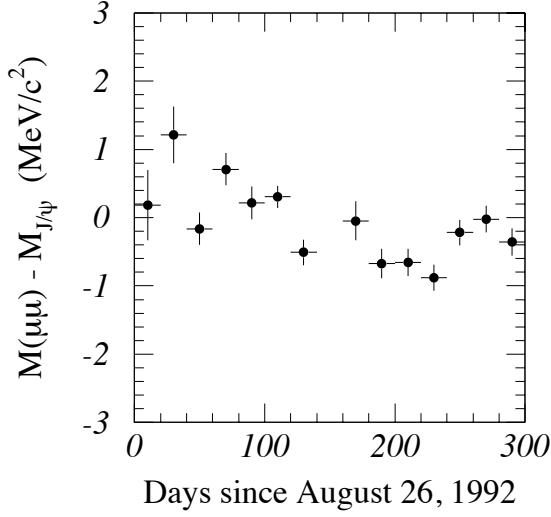


Figure 5.13: Variation of the measured J/ψ mass with time.

Furthermore, constructing the error in the mass due to the errors in $\cot \theta$,

$$\Delta M = \frac{p_{t1}p_{t2}}{M} \left[\left(\frac{\sqrt{1 + \cot^2 \theta_2}}{\sqrt{1 + \cot^2 \theta_1}} \cot \theta_1 - \cot \theta_2 \right) \Delta \cot \theta_1 + \left(\frac{\sqrt{1 + \cot^2 \theta_1}}{\sqrt{1 + \cot^2 \theta_2}} \cot \theta_2 - \cot \theta_1 \right) \Delta \cot \theta_2 \right] \quad (5.5)$$

confirms that at $\Delta \cot \theta = 0$ the error in the mass is zero. This kinematic point, which is independent of an error in $\cot \theta$, is used to extract the J/ψ mass by fitting mass versus $\Delta \cot \theta$ to a quadratic and taking the value at $\Delta \cot \theta = 0$ as the mass.

Time Variation An unexplained time variation of the J/ψ mass is observed over the data-taking period as shown in Figure 5.13. The RMS deviation, $0.5 \text{ MeV}/c^2$, is taken as a systematic uncertainty.

Uncertainty in the World-Average $M_{J/\psi}$ The uncertainty in the world-averaged J/ψ mass [35], $0.1 \text{ MeV}/c^2$, is included in the momentum scale uncertainty.

Extrapolation from $M_{J/\psi}$ to M_W The momentum scale is set using muons from J/ψ decays in which the average muon p_T is ~ 3 GeV/c. On the other hand, the average muon p_T from W decay is ~ 38 GeV/c. This apparent order-of-magnitude difference is misleading, however, since the CTC does not directly measure momentum, but curvature which is proportional to inverse momentum, $1/p_T$. The range of $1/p_T$ available in the J/ψ data, $0.2 - 0.5$ (GeV/c) $^{-1}$, is slightly larger than the difference between the average $1/p_T$ of J/ψ events, 0.3 (GeV/c) $^{-1}$, and those typical of the W , 0.03 (GeV/c) $^{-1}$. This provides a solid lever arm for the extrapolation from the J/ψ to the W , details of which are given in Appendix B. The non-linearity of the momentum scale is quantified using the variation of mass with $1/p_T^2$ (see Appendix B for the derivation of this),

$$\frac{\Delta M}{M} = \epsilon_1 + \epsilon'_3 \frac{1}{p_T^2}. \quad (5.6)$$

Figure 5.14 shows this variation with the average $1/p_T^2$ of the two muons, before and after the scaling of $\cot \theta$ given in Equation 5.1. The slope of this plot is ϵ'_3 and is the non-linearity of the momentum scale. To be conservative, the non-linearity measured before scaling $\cot \theta$ is used. Fitting a line and extrapolating from $\langle 1/p_T^2 \rangle = 0.14$ (GeV/c) $^{-2}$ to zero results in a mass difference of 0.9 MeV/c 2 . Since this is small and since it is possible for other effects to mimic a non-linearity³ it is applied as an uncertainty on the momentum scale rather than a correction to it.

Total The measured value for the J/ψ mass, extracted by fitting the data in Figure 5.8 and applying the radiative correction, is 3097.3 ± 1.7 MeV/c 2 . The momentum scale is corrected by a factor of 0.99986 ± 0.00054 for the J/ψ mass to agree with the world average of 3096.93 ± 0.09 MeV/c 2 [35]. This corresponds to a correction of -11 ± 45 MeV/c 2 at the W mass.

³Incorrectly-modelled energy loss is one source of concern. This type of effect does not scale linearly with momentum and does not affect $W \rightarrow \mu\nu$ the same as $J/\psi \rightarrow \mu\mu$.

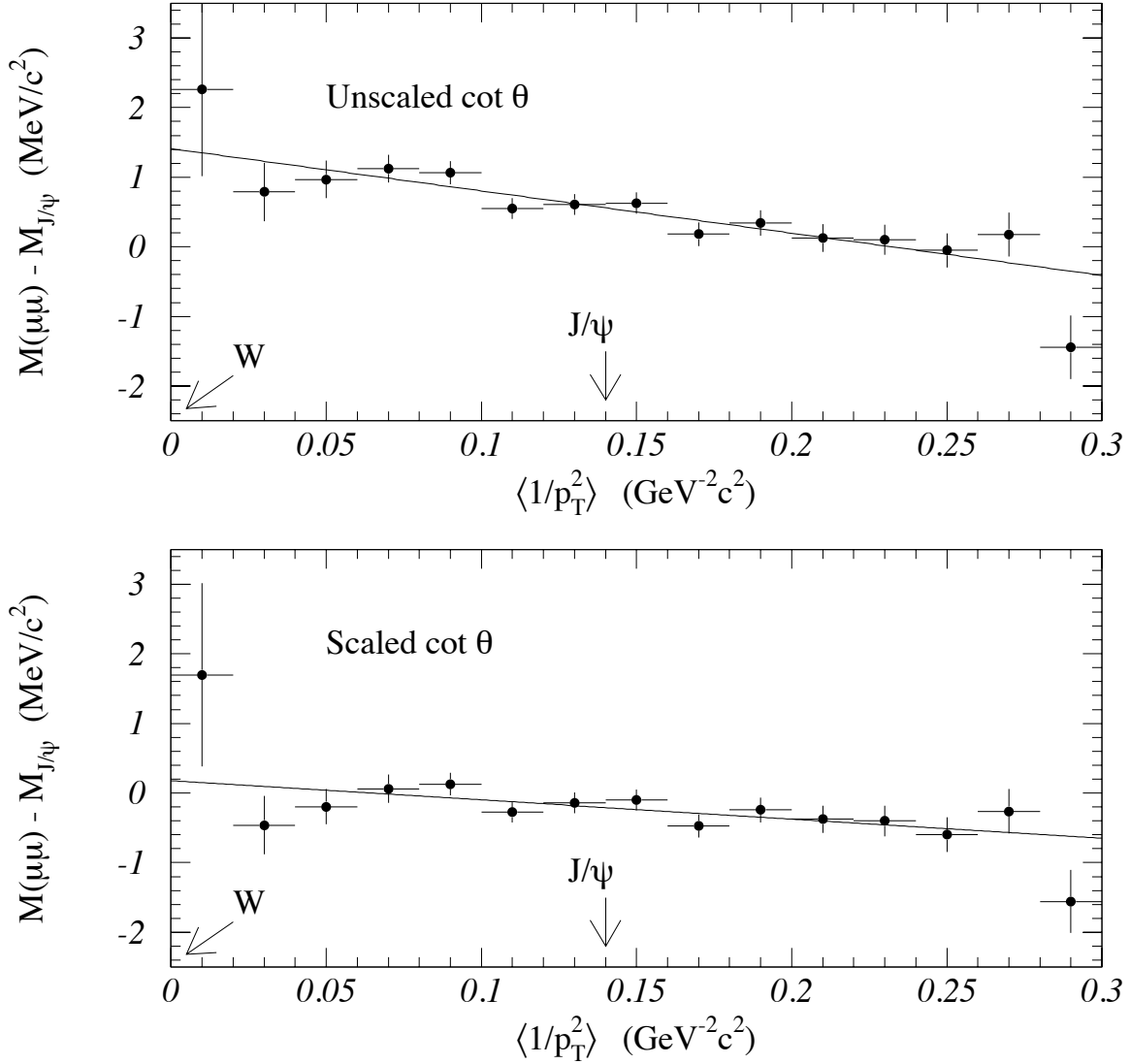


Figure 5.14: Variation of the measured J/ψ mass with the average $1/p_T^2$ of the two muons. The muons from W decays would lie in first bin of this plot (0.001 (GeV/c)⁻²). The average for J/ψ decays is 0.14 (GeV/c)⁻². The upper plot is before the $\cot \theta$ scaling; the lower plot is after. The slope in the lower plot is a factor of two smaller.

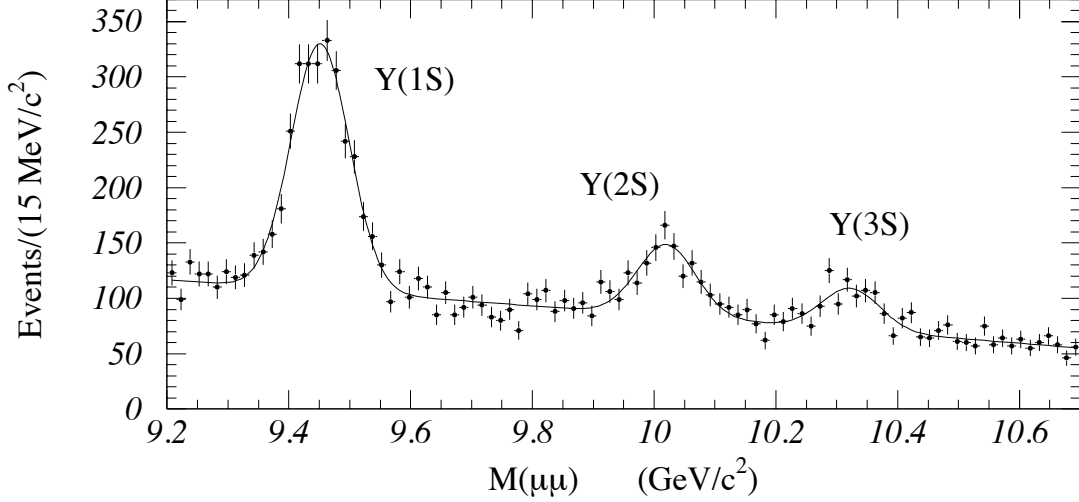


Figure 5.15: Invariant mass distribution of dimuon pairs near the Υ masses. The first three resonances can easily be distinguished. The curve is a sum of three Gaussians and a quadratic background.

5.3.2 Checks of the Momentum Scale

The momentum scale is checked using the first three Υ resonances (Figure 5.15) and the Z mass (Figure 5.16). The $\Upsilon \rightarrow \mu\mu$ decays are used to check the momentum scale using pairs of tracks with larger opening angles than in $J/\psi \rightarrow \mu\mu$ decays. The opening angles of $J/\psi \rightarrow \mu\mu$ decays are small because of the momentum threshold in the trigger. The J/ψ must have significant transverse momentum with which to boost the muons to large enough momenta to satisfy the trigger, resulting in correspondingly small opening angles. The Υ on the other hand, with its larger mass, does not need a transverse momentum to give the muons sufficient momenta to pass the trigger. The measured Υ masses, after the absolute scale determination and the QED radiation correction of $+3 \pm 1$ MeV/c², are shown in Table 5.2.

The mass of the Z boson measured in $Z \rightarrow \mu\mu$ decays is used to check the momentum scale using tracks with curvatures comparable to those used to measure the W mass, but is limited by the finite statistics in the peak. The measurement, in which

Resonance	Corrected Mass (MeV/c ²)	World-Average Mass (MeV/c ²)
$\Upsilon(1S) \rightarrow \mu\mu$	$9460 \pm 2 \pm 5$	9460.3 ± 0.2
$\Upsilon(2S) \rightarrow \mu\mu$	$10029 \pm 5 \pm 5$	10023.3 ± 0.3
$\Upsilon(3S) \rightarrow \mu\mu$	$10334 \pm 8 \pm 6$	10355.3 ± 0.5
$Z \rightarrow \mu\mu$	$91020 \pm 210 \pm 55$	91187 ± 7

Table 5.2: Measured masses of the Υ and Z resonances compared to the published values. The first uncertainty on the corrected value is from statistics. The second is the uncertainty from the momentum scale. The systematic uncertainties were not determined except for the Z where the systematic uncertainty is 50 MeV/c² (see Section 5.4).

the momentum resolution is extracted simultaneously with the mass, is described in detail in the next section.

5.4 Momentum Resolution

To measure the mass of the Z boson and the momentum resolution, Z events are simulated with a leading-order generator that includes the Drell-Yan and Z contributions and a parameterization of the radiative decay, $Z \rightarrow \mu\mu\gamma$, from Berends and Kleiss [37], implemented by R. G. Wagner [38]. The Z in the Monte Carlo is boosted with a transverse momentum selected from the $Z \rightarrow \mu\mu$ data (this is analogous to the W simulation in Chapter 7).

Invariant mass lineshapes are generated at various values of Z mass and momentum resolution, with the Z width fixed to the world average. The mass distribution from the $Z \rightarrow \mu\mu$ data, shown in Figure 5.16, is fitted to each lineshape in the range 76 to 106 GeV/c², using a log-likelihood fit (see Section 9 for details). If the radiative effect had not been included in the Monte Carlo, the shift in the fitted mass would have been 310 MeV/c². Table 5.3 contains a list of the systematic uncertainties on

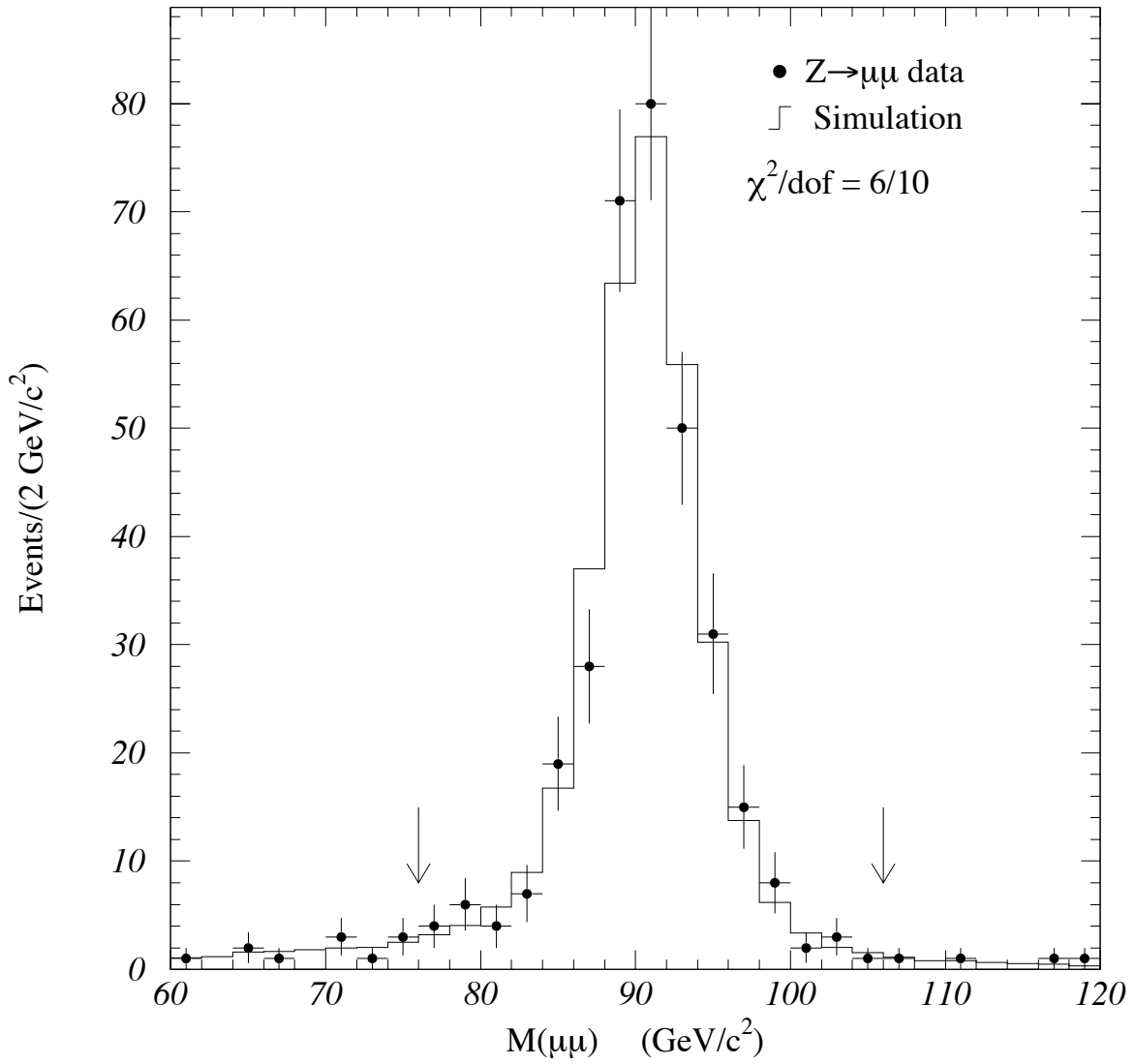


Figure 5.16: The dimuon mass spectrum near the Z mass. The arrows indicate the fit region of 76 to 106 GeV/c^2 .

Effect	ΔM_Z^μ (MeV/c ²)	$\Delta\delta p_T/p_T^2$ (GeV/c) ⁻¹
Statistics	210	0.000085
Momentum Scale	55	—
Radiative Corrections	40	0.000010
Fitting	10	negligible
Structure Function		negligible
Input p_T^Z spectrum		negligible
Total	220	0.000086

Table 5.3: Summary of uncertainties in measuring the Z mass.

the mass and resolution. The largest uncertainty, other than that from the momentum scale, is the effect of radiative decay. It is estimated to be 40 MeV/c², which comes from the differences between the calculation by Berends and Kleiss, and that provided by Baur and Berger [39]. The differences are in the handling of initial state radiation and lepton masses (Section 8.2). The choice of structure function contributes a negligible uncertainty. The uncertainty from the choice of the p_T^Z spectrum is shown to be negligible for variations constrained with the measured p_T^Z spectrum.

The fitted mass is

$$M_Z = 91.02 \pm 0.21(\text{stat.}) \pm 0.05(\text{syst.}) \pm 0.06(\text{scale}) \text{ GeV}/c^2. \quad (5.7)$$

This value is consistent with the LEP value of 91187 MeV/c² [35]. The fitted momentum resolution, extracted from the observed width of the Z , using $\Gamma_Z = 2.490$, is

$$\delta p_T/p_T^2 = 0.000810 \pm 0.000085(\text{stat.}) \pm 0.000010(\text{syst.}) (\text{GeV}/c)^{-1}. \quad (5.8)$$

This resolution is used in the track momentum simulation for the W mass measurement.

5.5 Summary

The calibration of the momentum measurement is described. The momentum scale is determined using $J/\psi \rightarrow \mu\mu$ decays and is found to be 0.99986 ± 0.00054 . The resolution of the momentum measurement is extracted from the width of the $Z \rightarrow \mu\mu$ mass peak and is $\delta p_T/p_T^2 = 0.00081 \pm 0.00009 \text{ (GeV/c)}^{-1}$.

Chapter 6

Recoil Measurement

In this chapter, the measurement of the recoil energy is explained. Since the neutrino is not directly observable, its momentum must be inferred from requiring momentum balance. This means everything else in the event must be added up. The muon momentum measurement has already been discussed which leaves just \vec{u} to be determined.

6.1 W Recoil Detection

The calorimeters are used to measure the transverse projection of the energy flow, \vec{u} , of particles associated with the recoil momentum¹ from the W boson. This transverse recoil energy is calculated only in the region of full azimuthal symmetry of the calorimeters, $|\eta| < 3.6$. Beyond this point accelerator magnets result in gaps in the calorimeters. The recoil energy is calculated as a vector according to

$$\vec{u} = \sum_i E_i^{\text{TOWER}} (\hat{\rho}_i \cdot \hat{n}_i) \hat{\rho}_i \quad (6.1)$$

¹Recoil, recoil energy, and recoil momentum are used interchangeably to describe the net transverse momentum attributed to the particles recoiling against the W , that is, balancing the momentum given the W in the production process (Figure 2.3).

where E_i^{TOWER} is the energy in the i^{th} calorimeter tower (separate terms for the EM and IIAD components), $\hat{\mathbf{n}}_i$ is a unit vector pointing from the interaction vertex to that calorimeter tower, and $\hat{\boldsymbol{\rho}}_i$ is a unit vector in the r - ϕ plane pointing in the ϕ direction of the calorimeter tower. The dot product selects the transverse components of the recoil momentum. The above sum is only for calorimeter towers that are above some threshold. These energy thresholds are set calorimeter-by-calorimeter (CEM, CHA, etc.) several standard deviations above the noise typical of that system, and range from 100 MeV for the central detectors to 800 MeV for the forward hadronic detectors.

The sum in Equation 6.1 includes energy deposited in the calorimeter by the muon which must be subtracted out to determine just the recoil momentum. The corrected form of the recoil energy is

$$\vec{u} = \sum_i E_i^{\text{TOWER}} (\hat{\boldsymbol{\rho}}_i \cdot \hat{\mathbf{n}}_i) \hat{\boldsymbol{\rho}}_i - \sum_{\mu} (E_{\mu}^{\text{TOWER}} - E_u) (\hat{\boldsymbol{\rho}}_{\mu} \cdot \hat{\mathbf{n}}_{\mu}) \hat{\boldsymbol{\rho}}_{\mu} \quad (6.2)$$

where the second summation runs over the towers traversed by the muon. The second term removes the energy contribution from the muon by subtracting all but a small amount of energy, E_u , corresponding to the recoil deposition. This small amount of energy left behind is determined by studying the energy deposited in the surrounding towers which receive no muon energy. Figure 6.1 shows the distribution of the average energy in the neighboring towers. The mean of this distribution, E_u , is (30 ± 2) MeV.

6.2 Recoil Measurement Errors

Recall from Equation 2.14 that M_T is sensitive to errors in u_{\parallel} . The sensitivity of u_{\parallel} to the muon identification and removal procedures is examined by breaking up \vec{u} into its components parallel to, and perpendicular to, the muon direction (u_{\parallel} and u_{\perp}).

The average number of towers the muon traverses is 1.5 (Figure 6.1). Since the direction of these towers is parallel to the muon direction, the error introduced into

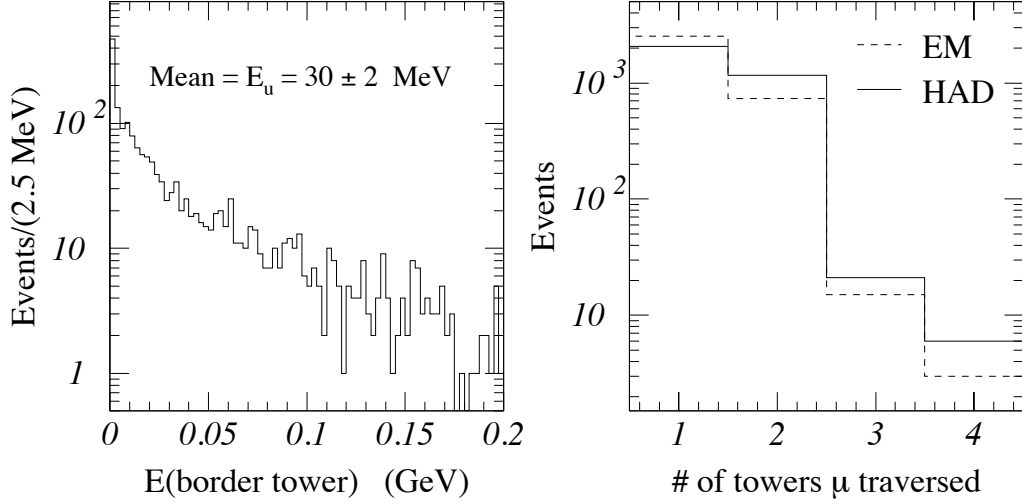


Figure 6.1: Left: The average energy, E_u , in the towers bordering the towers traversed by the muon. Right: The number of towers traversed by the muon. The average is ~ 1.5 .

the mean of u_{\parallel} $\langle u_{\parallel} \rangle$, by the 2 MeV uncertainty in the mean of E_u is $2 \times 1.5 = 3$ MeV. The corresponding error in M_W^2 . is $5 \text{ MeV}/c^2$.

The muon identification requirement ($E^{\text{HAD}} < 6 \text{ GeV}$ and $E^{\text{EM}} < 2 \text{ GeV}$; Section 4.5) may introduce a bias in $\langle u_{\parallel} \rangle$ and in the W mass. For example, if the W decays such that the muon travels in the same direction as the recoil, there is greater opportunity for the recoil particles to cause the muon identification to fail. These effects are investigated by tightening the muon identification requirements and measuring the subsequent shifts in $\langle u_{\parallel} \rangle$ and M_W . If the above energy cuts of 2 GeV and 6 GeV are also applied to the towers bordering the calorimeter tower traversed by the muon, a shift of $30 \text{ MeV}/c^2$ is seen in M_W and a shift of 70 MeV is seen in $\langle u_{\parallel} \rangle$. Dividing by the number of additional towers included in the cut leads to an uncertainty of $10 \text{ MeV}/c^2$ on M_W and 20 MeV on $\langle u_{\parallel} \rangle$. Table 6.1 summarizes the uncertainties from muon identification and removal.

²Shifts in M_W are obtained using the mass fitting algorithm described in Chapter 9

Effect	$\Delta\langle u_{\parallel}\rangle$ (MeV)	ΔM_W (MeV/c ²)
Muon Removal	3	5
Muon Identification	20	10
Total	20	10

Table 6.1: Summary of systematic uncertainties on $\langle u_{\parallel}\rangle$ and M_W incurred from the identification and removal of the muon.

6.3 W Recoil Calibration

Calibrating the response of the calorimeters to the recoil from the W boson is problematic as it depends on details of the flow and energy distributions of the recoil particles. The magnetic field prevents particles with energies below ~ 400 MeV from reaching the calorimeter. In addition, the absolute gains and linearities of these calorimeters (with the notable exception of the CEM) are not known to great precision.

Rather than attempt an understanding of these detectors from “first principles”, the calorimeter response to recoil energy is mapped out using $Z \rightarrow ee$ events. The electrons in $Z \rightarrow ee$ events are measured with a better resolution than the recoil energy. The p_T of the Z is measured from the electrons and thus the recoil response is calibrated for a given p_T^Z . Figure 6.2 is a scatter plot of $|\vec{u}|$ versus p_T^Z . Notice that since \vec{u} should balance \vec{p}_T^Z , the calorimeter measures the true recoil momentum systematically low. By using Z bosons to calibrate \vec{u} , the problem of having to individually model such things as luminosity dependence and jet corrections is avoided. All these effects are reflected in the Z data since it was collected in the same fashion and proportions as the W data. Explicit details of how this calibration is carried out in the simulation are given in Section 7.

Figure 6.3 shows the distributions of $|\vec{u}|$ and its components, u_{\parallel} and u_{\perp} for the data. These distributions will be compared to the simulated distributions in Chapter 7 as a check of both the simulation and the measurement of $|\vec{u}|$ from the data.

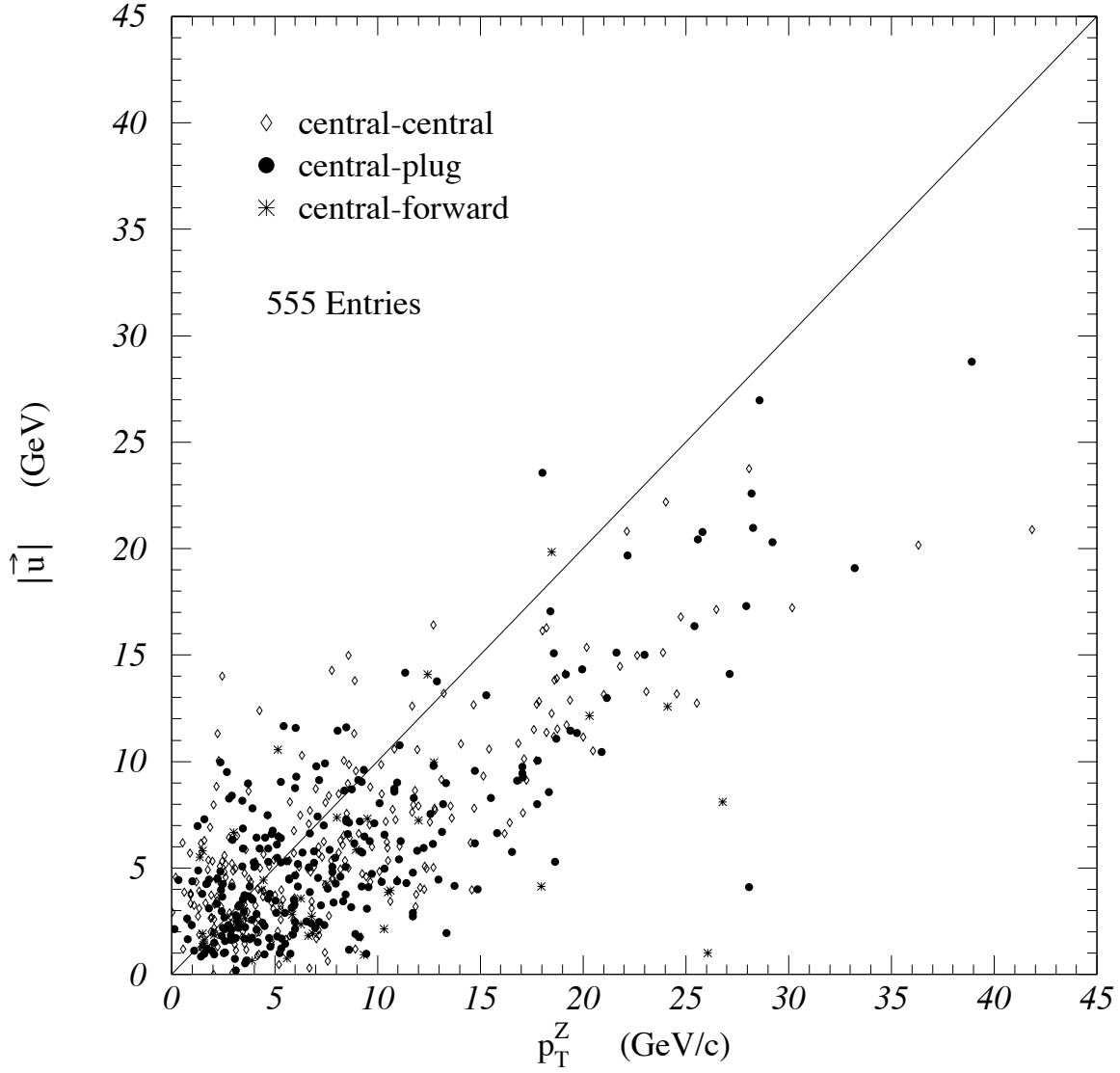


Figure 6.2: Scatter plot of $|\vec{u}|$ versus p_T^Z . The diagonal line is $|\vec{u}| = p_T^Z$ and indicates a systematic undermeasurement of $|\vec{u}|$.

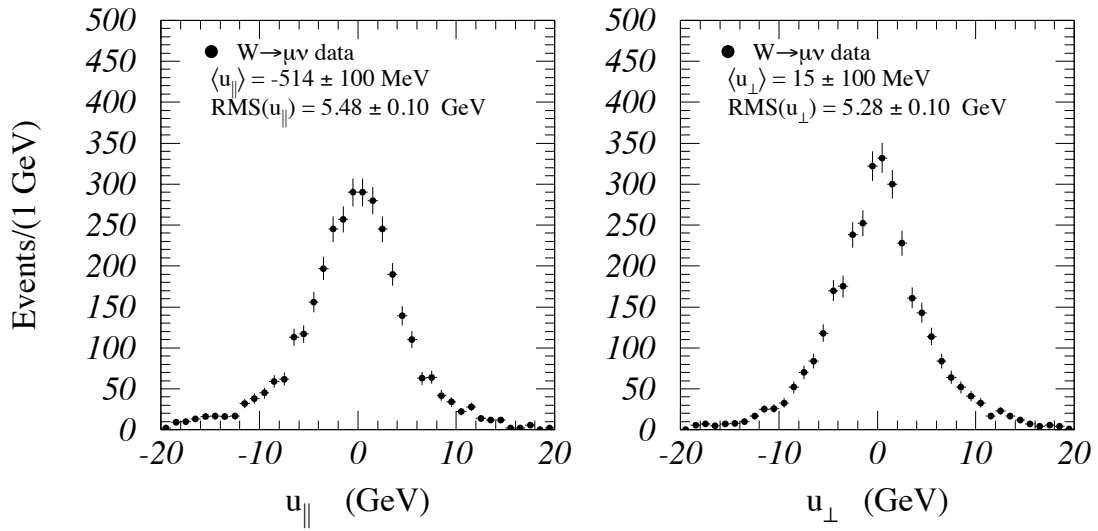
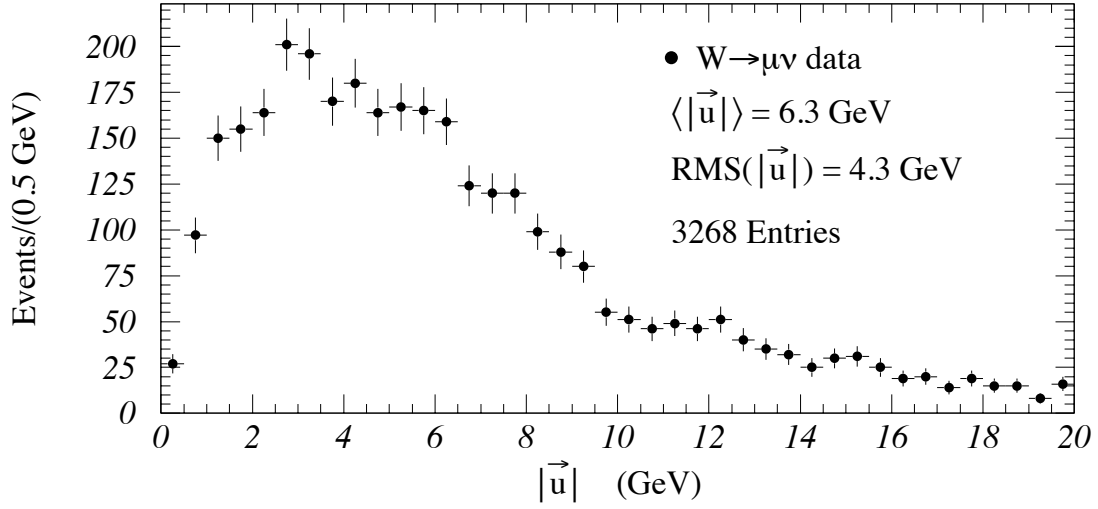


Figure 6.3: Top: The distribution of $|\vec{u}|$ for the data. Bottom: Distributions of u_{\parallel} and u_{\perp} .

6.4 Summary

The identification of muons and their separation from the recoil energy summation affect $\langle u_{\parallel} \rangle$ and thereby the W mass. The combination of these effects contributes an uncertainty on the W mass of $10 \text{ MeV}/c^2$. The recoil is calibrated using $Z \rightarrow ee$ events where the p_T of the boson is relatively well measured from the electrons. This calibration takes place within the simulation described in Chapter 7.

Chapter 7

Monte Carlo Simulation

In the previous chapters, the measurement and calibration of M_T have been discussed. This chapter describes part two of the analysis, the generation of a theoretical M_T distribution to fit to the data. As stated earlier, there is no closed analytical form for M_T , so a Monte Carlo simulation of M_T is used as the theoretical fitting function.

7.1 Event Generation

7.1.1 Leading-order Production and Decay

W events are generated according to a Breit-Wigner invariant mass distribution and a leading-order ($p_T^W = 0$) model of quark-antiquark annihilation (see Chapter 2). Events are randomly selected to have \hat{s} in the region $|\sqrt{\hat{s}} - M_W| < 25 \Gamma_W$. This window is chosen to be large enough such that events generated outside it have an extremely low probability of having an M_T value that would fall within $65 - 100 \text{ GeV}/c^2$. Varying the allowed range of $\sqrt{\hat{s}}$ by several widths produces no effect on the mass determination confirming that 25 widths is large enough. The values of M_W and Γ_W are input to the simulation. The W is produced with a rapidity¹ determined from the longitudinal

¹Rapidity is defined as $y = \ln \frac{E+p_L}{E-p_L}$.

momentum distributions of the initial quarks. The quark momentum distributions are based on MRS D'_- parton distribution functions (PDFs) [40] evaluated at $Q^2 = \hat{s}$. Errors associated with the choice of PDF are discussed in Chapter 10. The W is decayed in the center-of-mass frame with a random $\hat{\phi}$ distribution for the muon, and a $\hat{\theta}$ distribution given by $(1 + P \cos \hat{\theta})^2$ where P is the polarization of the W and is ± 1 depending on the charge of the created W .

7.1.2 W Transverse Momentum

Because a leading-order model is used, the effects of higher-order diagrams on the production of W bosons (Figure 2.3) must be added by hand. The most significant effect² is that the W has a transverse momentum, p_T^W . Unfortunately, the low- p_T part of the p_T^W spectrum, from which most of the events used in this measurement are drawn, is not known at sufficient precision, either experimentally or theoretically, to use in this W mass measurement. A experimental measurement of the p_T^W spectrum [41] has systematic uncertainties greater than 300% in the pertinent region. In addition, the shape of theoretical calculations in this p_T region is also subject to large uncertainties [42, 43]. Rather than using a previous p_T^W measurement or a theoretical calculation, the similarity of the p_T spectra of W and Z bosons observed in direct measurements [41, 44] and in theoretical predictions [45] is used as a starting point. Specifically, an initial guess at the proper p_T^W spectrum is the observed $Z \rightarrow ee$ p_T spectrum measured from the decay electrons.

To get from the observed p_T^Z spectrum to the initial p_T^W spectrum, the p_T^Z spectrum is divided into bins in p_T and a bin-by-bin correction is applied to account for the average shift within that p_T^Z range caused by the electron resolution. This “unsmeared” p_T^Z spectrum is horizontally scaled to account for possible differences between the p_T^W

²Other higher-order effects are discussed in Chapter 10.

r	$\langle u_{\parallel} \rangle$ (MeV)	RMS(u_{\parallel}) (GeV)	RMS(u_{\perp}) (GeV)
DATA	-514 ± 100	5.48 ± 0.10	5.28 ± 0.01
1.05	-295	5.19	5.11
1.08	-323	5.27	5.23
1.11	-377	5.38	$\equiv 5.30$
1.14	-469	5.57	5.47
1.17	-521	5.65	5.55

Table 7.1: Variation of the mean and RMS deviations of u_{\parallel} and u_{\perp} with the p_T^W scale factor, r . The nominal value of r corresponds to the intersection of RMS(u_{\perp}) from the data and RMS(u_{\perp}) from the simulation. The uncertainty corresponds to the point when the difference between data and simulation equals the uncertainty on RMS(u_{\perp}) from the data (0.1 GeV).

and p_T^Z spectra.

$$p_T^W = r \times p_T^Z(\text{unsmearred}) \quad (7.1)$$

where r is the scale factor. The effect of changing the shape of the p_T^Z spectrum as opposed to simply stretching it is also checked (see Chapter 10), but the scaling is sufficient for the desired precision.

The scale factor, r , is determined by the width of the u_{\perp} distribution. Recall that u_{\perp} is not as sensitive to the recoil measurement as u_{\parallel} , so u_{\perp} is chosen to constrain r . The value of r is varied until the the RMS of u_{\perp} from the simulation agrees with the data. The uncertainty on the scale factor corresponds to the uncertainty on the RMS of u_{\perp} from the data. Table 7.1 lists the means and RMS deviations of u_{\parallel} and u_{\perp} as a function of r . A variation of 0.03 in r corresponds to a variation of ~ 0.1 GeV in the simulation's u_{\perp} RMS. Thus r is determined to be 1.11 ± 0.03 .

The resulting p_T^W spectrum, using the best value of 1.11 for r , is shown in Figure 7.1. The decay products of the simulated W are Lorentz-boosted in the center-of-mass frame

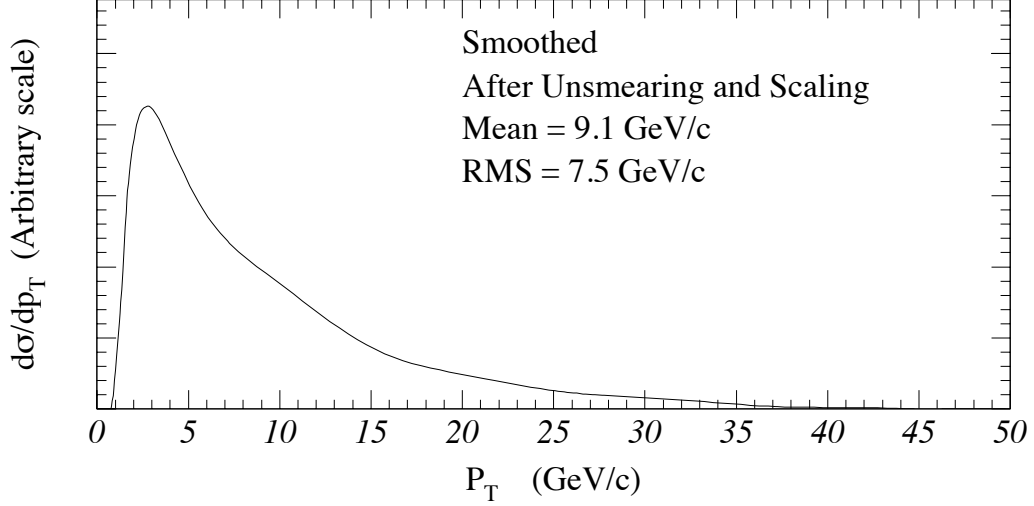


Figure 7.1: The initial p_T^W spectrum used in the W event simulation. The spectrum is derived from 555 $Z \rightarrow ee$ events.

of the quark-antiquark pair with a p_T^W chosen from this distribution and a random $\hat{\phi}$.

7.2 Detector Simulation

After producing and decaying the W boson, the daughter products are Lorentz-boosted from the center-of-mass of the initial quarks to the lab frame where the detector responses to both the muon and the recoil momentum are simulated.

7.2.1 Trigger Simulation

The simulated muon is required to traverse both the CMU and CMP detectors to simulate the trigger logic³. The transverse mass is sensitive to p_T^μ -dependent efficiencies and of the three trigger levels, level-2 is the most sensitive to conditions within the event which may be correlated with p_T . For this reason, the efficiency of the CFT (recall

³This trigger simulation includes the ϕ and η gaps (see Figure 3.4).

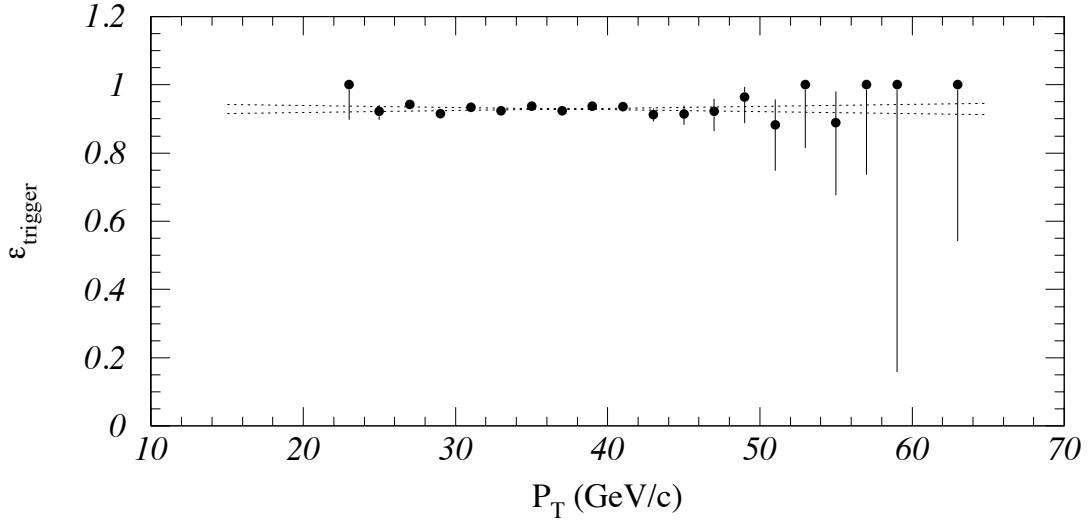


Figure 7.2: The Level-2 muon trigger efficiency as a function of track p_T (GeV/c). The dotted lines indicate $\pm 1\sigma$ uncertainty in the slope of a linear fit.

Section 4.2) is studied using $W \rightarrow e\nu$ events where the electron was not constrained to pass the CFT trigger⁴. $W \rightarrow e\nu$ data is chosen because it reproduces the environment of $W \rightarrow \mu\nu$ events where the recoil direction and backgrounds are correlated with the p_T of the charged lepton. This correlation with the charged lepton is important because the more “stuff” there is in the vicinity of the lepton track, the higher the probability of finding hits to associate with a track and hence the higher the triggering efficiency. Fortunately there is no p_T dependence seen in the $W \rightarrow e\nu$ data (Figure 7.2) so the statistical ability to detect such a dependence is taken as a limit.

7.2.2 Momentum Resolution

The momentum of the muon is smeared using the parameterization of Section 5.4. Because the CTC measures curvature ($\propto 1/p_T$), the resolution function will be Gaussian

⁴Electrons are collected using several triggers which do not involve the CFT, whereas muons always use the CFT.

in $1/p_T$,

$$\delta(1/p_T) = \delta p_T / p_T^2 = 0.00081 \pm 0.00009. \quad (7.2)$$

Therefore $1/p_T$ is smeared by a gaussian of width $(0.081 \pm 0.009)\%$,

$$1/p_T(\text{smeared}) = 1/p_T + G_{\text{RES}} \quad (7.3)$$

where G_{RES} is a gaussian random number with a mean of zero and a width of 0.00081.

7.2.3 Recoil Simulation

In Section 7.1.2, the W is given a transverse momentum, p_T^W . In this section, the calorimeter response to the recoil associated with that p_T^W is modeled using a look-up table of $Z \rightarrow ee$ events. The fact that $Z \rightarrow ee$ events also model p_T^W is convenient but not necessary. This calorimeter modeling works with any p_T^W spectrum. Using Z events to model the recoil response is possible because the energy resolution of electrons is much better than the general recoil resolution of the calorimeters. $Z \rightarrow ee$ events are used, as opposed to $Z \rightarrow \mu\mu$, because the calorimeters, which detect the electrons, have nearly full solid angle coverage. This full coverage enables the “second electron” to reproduce the kinematic distributions of the neutrino (which can go anywhere). The CTC on the other hand, which detects the muons, does not extend as far in η and hence does not quite allow the “second muon” to reproduce the neutrino distributions. $Z \rightarrow \mu\mu$ events are used as a check and they give similar results.

Each entry in the look-up table consists of the transverse momentum of the Z , p_T^Z , as measured from the electrons and the projections of \vec{u} parallel and perpendicular to \vec{p}_T^Z (u_1 and u_2 ; see Figure 7.3). Starting with the p_T^W chosen in the simulation, the look-up table is searched for a p_T^Z within 2 GeV/c of p_T^W . If no p_T^Z is found, the size of the window is increased to ± 3 GeV/c and the table is searched again. The window is increased until a match is found, with each search starting from a random point in the

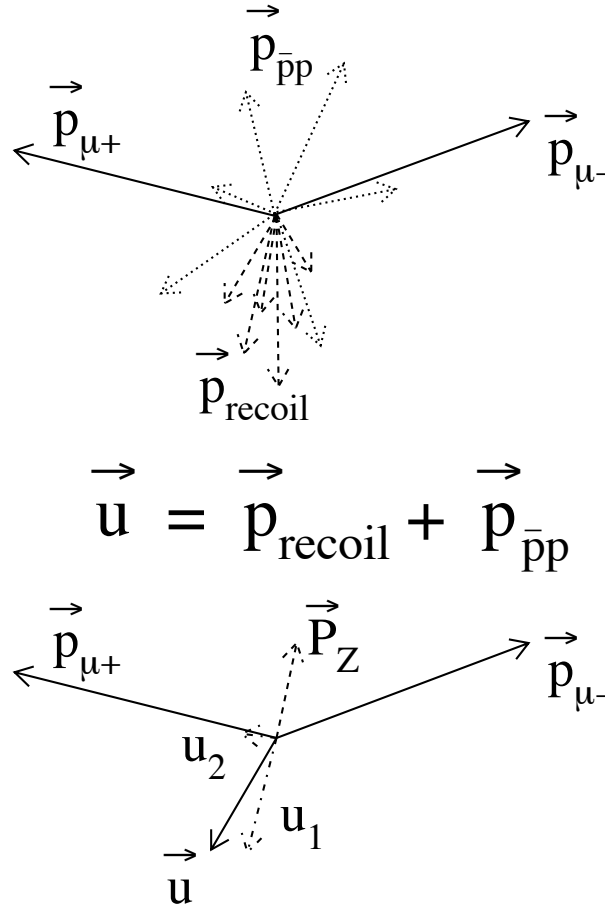


Figure 7.3: Composition in the transverse plane of Z events used in the look-up table. Note that \vec{u} is decomposed relative to \vec{p}_T^Z as opposed to \vec{p}_T^μ as in the case of the W . This is because the muon directions in the Z event and in the W event from the simulation are uncorrelated and it is meaningless to associate them in any way. After the Z event is transferred to the simulation \vec{u} is resplit into u_{\parallel} and u_{\perp} .

table. After a match is found, the corresponding values of u_1 and u_2 are scaled by the ratio p_T^W/p_T^Z . The scaled values of u_1 and u_2 , referenced relative to the simulation's \vec{p}_T^W (this amounts to aligning \vec{p}_T^Z with \vec{p}_T^W from the simulation), are used to construct a simulated \vec{u} . This \vec{u} is decomposed into u_{\parallel} and u_{\perp} components for comparison to data.

The advantage of this method is that there are no parameterizations to adjust. The only assumption is that the response of the detector to the recoil of a W boson of some p_T is the same as the response to the recoil of a Z boson of the same p_T .

7.3 Comparison of Simulation and Data

Figure 7.4 is a comparison between data and simulation of $|\vec{u}|$ and its components u_{\parallel} and u_{\perp} . The lack of smoothness in the simulated distribution of $|\vec{u}|$ reflects the finite number of $Z \rightarrow ee$ events used to model the recoil response. The uncertainties on each point are difficult to determine; however, since it is not used to constrain any part of the model and since the effect of the finite number of $Z \rightarrow ee$ events is dealt with separately, it is not worrisome. Table 7.2 lists further tests of the ability of the simulation to reproduce the data by comparing u_{\parallel} and u_{\perp} as the maximum allowed value of $|\vec{u}|$ is lowered from 20 GeV (Section 4.5; W mass data sample cut) to 3 GeV. The largest bias to u_{\parallel} arises from requiring a minimum p_T for the muon in the event selection; decays of the W boson in which the muon is boosted by the transverse momentum of the W are preferentially kept. This is demonstrated in Figure 7.5 where $\langle u_{\parallel} \rangle$ is plotted against p_T^{μ} . There is a variation of 30 GeV in $\langle u_{\parallel} \rangle$ over the range of muon momenta. As shown in the plot of residuals, the simulation does a good job of reproducing this variation. Similar plots of $\langle u_{\parallel} \rangle$ versus p_T^{μ} also show good agreement. The variation of $\langle u_{\parallel} \rangle$ with the transverse mass of the event is shown in the top half of Figure 7.6. These variations are much smaller than those with p_T^{μ} (which is why the transverse mass is used to extract the W mass), and are well-described by the

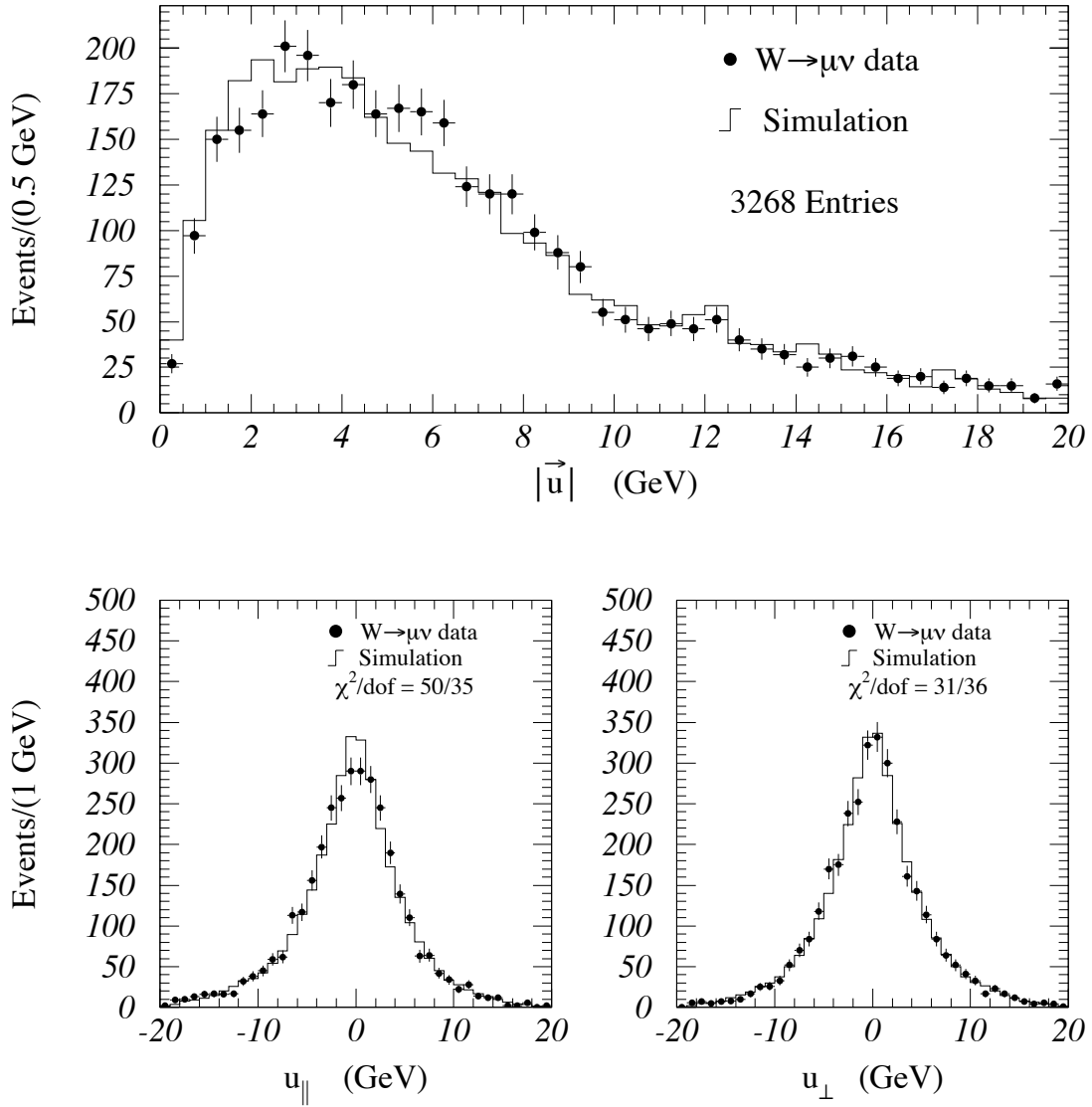


Figure 7.4: Top: The distribution of $|\vec{u}|$ for the data and simulation. The roughness of the simulation is due to the finite number of $Z \rightarrow ee$ events used to model the recoil response. Bottom: Distributions of u_{\parallel} and u_{\perp} . The small discrepancy between data and simulation in u_{\parallel} is only a little over one standard deviation and is covered by the uncertainty in the p_T^W scale factor, r .

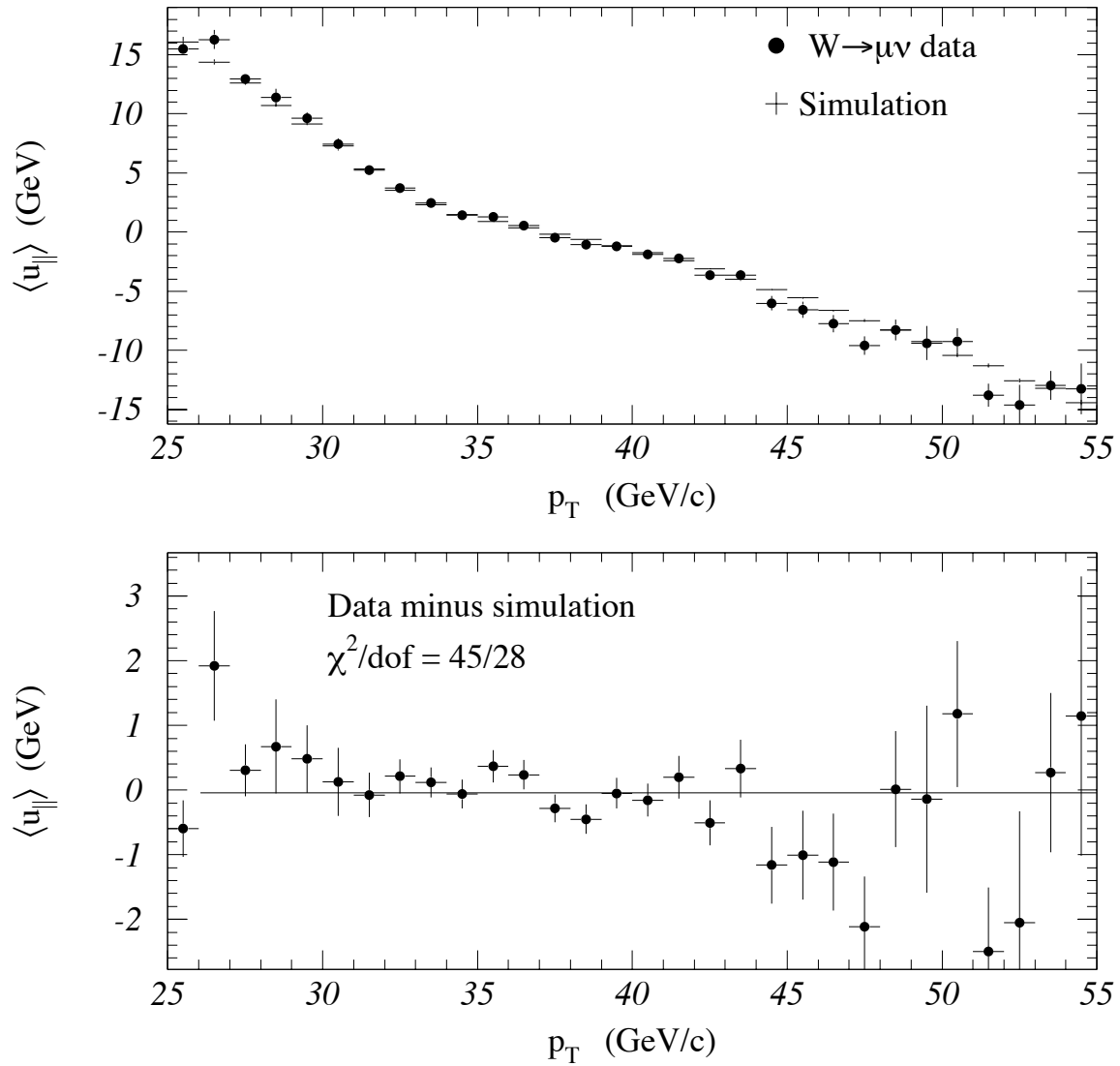


Figure 7.5: Upper: Data and simulation $\langle u_{\parallel} \rangle$ as a function of the muon p_T . Lower: The residuals of the data minus the simulation.

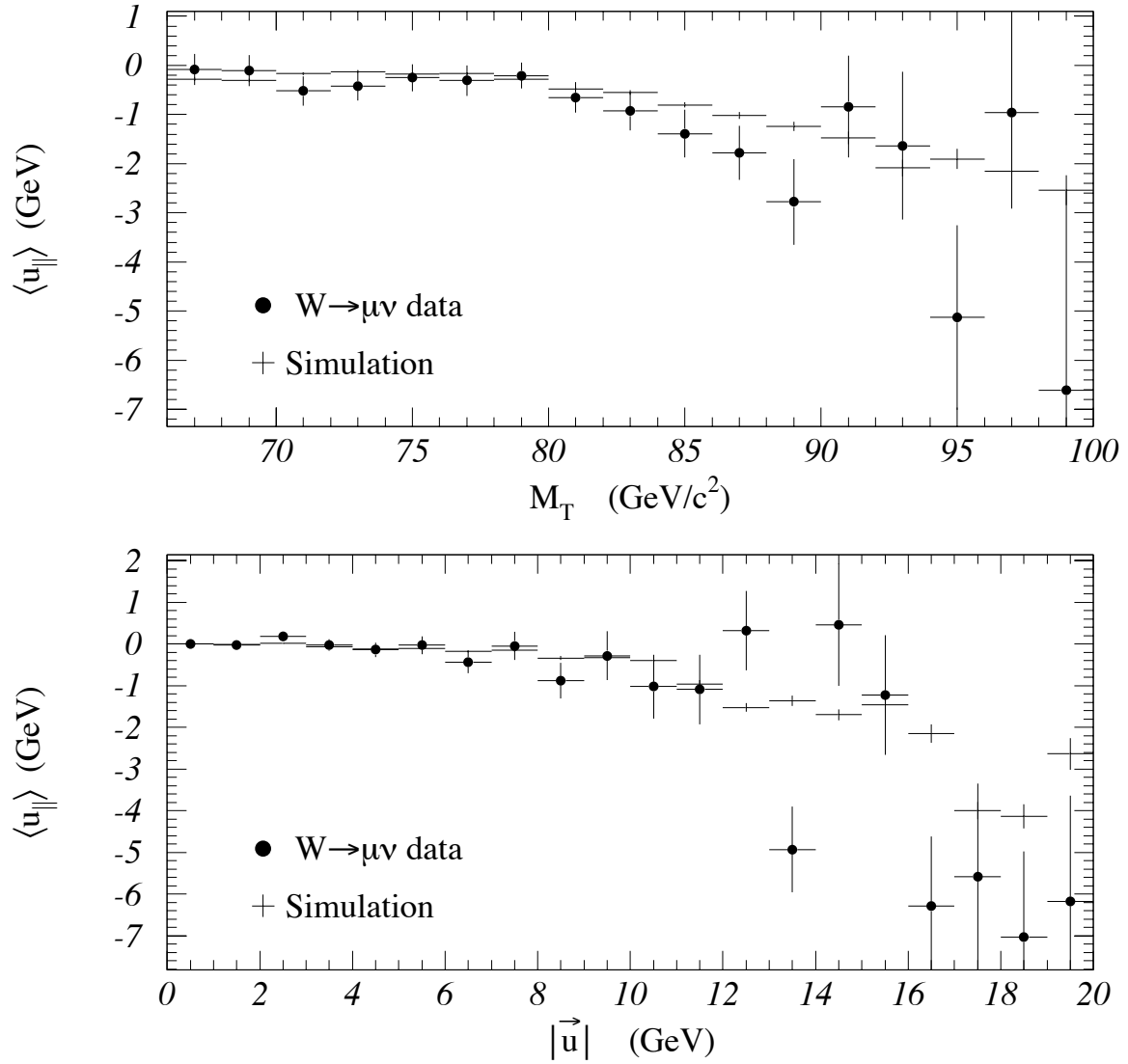


Figure 7.6: Upper: Data and simulation $\langle u_{\parallel} \rangle$ as a function of M_T . Lower: Data and simulation $\langle u_{\parallel} \rangle$ as a function of $|\vec{u}|$.

max $ \vec{u} $ (GeV)	$\langle u_{\parallel} \rangle$ (MeV)		RMS(u_{\parallel}) (GeV)		RMS(u_{\perp}) (GeV)	
	DATA	SIM	DATA	SIM	DATA	SIM
20	-514 ± 100	-377	5.48 ± 0.10	5.38	5.28 ± 0.10	5.30
15	-266 ± 90	-251	4.77 ± 0.09	4.76	4.64 ± 0.09	4.70
10	-128 ± 80	-104	3.77 ± 0.08	3.67	3.74 ± 0.08	3.66
5	$+1 \pm 60$	-42	2.25 ± 0.06	2.18	2.14 ± 0.06	2.16
3	$+74 \pm 50$	+4	1.43 ± 0.05	1.38	1.37 ± 0.05	1.37

Table 7.2: Variation of the means and RMS deviations of u_{\parallel} and u_{\perp} with the maximum allowed $|\vec{u}|$ for data and simulation. The uncertainties are statistical only.

simulation. The behavior of $\langle u_{\parallel} \rangle$ versus $|\vec{u}|$ is a sensitive tests of the quality of the event modeling and exhibits good agreement between data and simulation in the lower half of Figure 7.6.

7.4 Summary

The simulation of W events is described, detailing the parameters involved and comparing some results to data. In the next chapter, the description of the simulation is concluded by adding background processes to the simulation. The uncertainties introduced into the mass measurement by possible errors in the parameters of the simulation are discussed in Chapter 10.

Chapter 8

Backgrounds and Radiative Corrections

The W mass data sample includes processes other than $W \rightarrow \mu\nu$ which alter the observed M_T distribution resulting in an error in the measured W mass. These processes include backgrounds which mimic $W \rightarrow \mu\nu$ decays, and radiative decays of the W , $W \rightarrow \mu\nu\gamma$. Some of these effects are included in the simulation while for others, a correction is applied to the fitted M_W .

8.1 Backgrounds

The relative shapes and sizes of the backgrounds present in the W mass data sample are shown in Figure 8.1.

$Z \rightarrow \mu\mu$ The decay $Z \rightarrow \mu\mu$ is the largest background present in the W mass sample and is included in the simulation. When one of the muons from the Z is not detected by the CTC, the remaining muon causes the event to resemble $W \rightarrow \mu\nu$. This background is large because the CTC has limited η coverage. The coverage extends to $|\eta| < 1.7$, however the efficiency for finding a track falls with increasing $|\eta|$ for $|\eta| > 1.0$

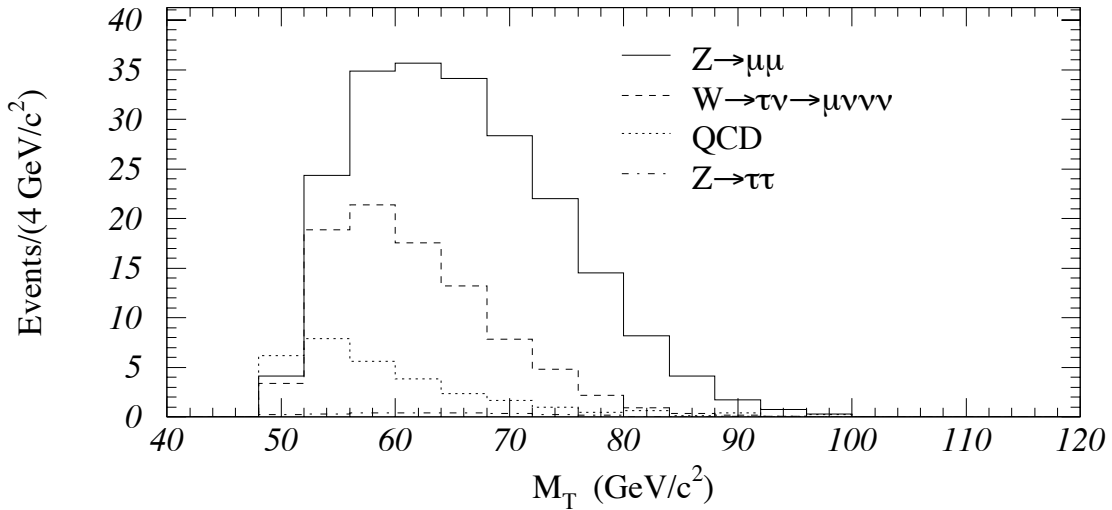


Figure 8.1: Transverse mass distributions of background processes present in the $W \rightarrow \mu\nu$ sample.

(Figure 8.2). This background is calculated using a monte carlo simulation of $Z \rightarrow \mu\mu$ events. The $Z \rightarrow \mu\mu$ background fraction is determined to be $(3.6 \pm 0.5)\%$ and is included in the W mass simulation by adding its M_T , p_T^μ , and p_T^ν distributions to the simulation lineshapes.

The uncertainty in the $Z \rightarrow \mu\mu$ background estimate comes from two sources: the uncertainty in the measured tracking efficiency, and the choice of parton distribution functions. The tracking efficiency of the detector simulation, ϵ_{TRACK} , is varied in the region $1.0 < |\eta| < 1.7$ by a conservative 10%, i.e. $\epsilon_{\text{TRACK}} \pm 0.1$. The resulting uncertainty in the background fraction is 0.5%. In the region $|\eta| < 1.0$, ϵ_{TRACK} is greater than 0.99 translating to a negligible uncertainty.

The size of the $Z \rightarrow \mu\mu$ background potentially has a large dependence on the choice of parton distribution function since it involves one, and only one, muon at high η . Such muons preferentially come from the high-rapidity tail of the Z production cross section, which is sensitive to the small- x behavior of the parton distribution functions.

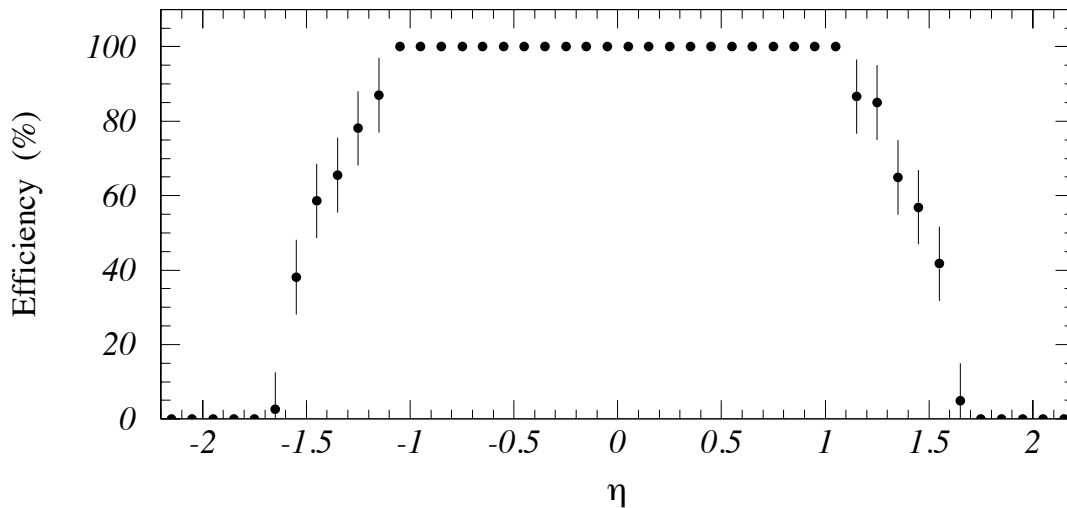


Figure 8.2: The CTC tracking efficiency as a function of η . The uncertainties are $\pm 10\%$, i.e. $\epsilon \pm 0.1$.

The uncertainty in the background fraction due to the choice of parton distribution functions is estimated to be 0.2%.

In addition to the effect on M_T , there is also a bias in $\langle u_{\parallel} \rangle$. This bias is significant because the amount of $Z \rightarrow \mu\mu$ contamination is large and the undetected muon deposits ~ 2 GeV of energy in the calorimeters in the opposite ϕ direction to the found muon. A shift of -36 ± 5 MeV in $\langle u_{\parallel} \rangle$ is estimated and included in the simulation in a similar fashion to the inclusion of M_T .

$W \rightarrow \tau\nu$ The $W \rightarrow \tau\nu$ background involves the further decay of the τ into a muon and two neutrinos. This sharing of the available energy between four final state particles results in a much softer p_T spectrum for the muon (recall that the W selection cuts were designed to remove processes with soft p_T spectra) and hence a smaller background fraction than $Z \rightarrow \mu\mu$. The $W \rightarrow \tau\nu$ background fraction is found to be 0.78% and is included in the simulation. Since $W \rightarrow \tau\nu$ is topologically very similar to $W \rightarrow \mu\nu$ decays, it can be simulated precisely enough to result in a negligible uncertainty. This

background is added to the simulation by randomly decaying the W to a $\tau\nu$ pair and then decaying the τ to a muon and neutrino. The muon is treated just like a direct muon from W decay.

Heavy-Flavor Decays and Fakes The background from jet and heavy-flavor production is estimated using the $W \rightarrow \mu\nu$ data sample. Each event is characterized by Σp_T , the sum of the p_T of tracks with p_T greater than 1.0 GeV/c in a cone ($\sqrt{(\Delta\phi)^2 + (\Delta\eta)^2} < 0.4$) around the muon. A di-jet event¹, where one jet is misidentified as a muon, will likely result in many tracks near the muon giving a large Σp_T . In addition, for the neutrino to pass the selection cuts, one of the jets must be significantly mismeasured causing the neutrino candidate to be preferentially parallel with the jets (and therefore the muon). A heavy-flavor decay such as $b \rightarrow c\mu\nu$ will result in nearby tracks from the hadronization of the charm quark (c). In this case, the b quark, because of its relatively small mass, needs a large transverse momentum to enable the muon and the neutrino to satisfy the p_T requirement. This leads to small opening angles for the decay products causing them to be preferentially parallel. Thus, one characteristic of the background is for the neutrino to be parallel/antiparallel with the jet (or largest if more than one).

A sample of non-isolated muons is made by requiring $\Sigma p_T > 2$ GeV/c, which should contain most of the background. A sample which is more likely to be background-free is made by requiring² $\Sigma p_T < 2$ GeV/c. Distributions of $\phi_{\nu\text{jet}}$ of the two samples are then compared, where $\phi_{\nu\text{jet}}$ is the azimuthal angle between the neutrino direction and the direction of the highest E_T jet with $E_T > 5$ GeV. As stated before, background events tend to have $\phi_{\nu\text{jet}} \sim 0^\circ$ or $\sim 180^\circ$. Normalizing the isolated sample to the non-isolated sample in the range $30 < \phi_{\nu\text{jet}} < 150^\circ$, the non-isolated sample is found to have an excess of 6 events over the isolated sample in the range $\phi_{\nu\text{jet}} < 30^\circ$ or

¹A di-jet event consists of two jets back-to-back in ϕ .

²Even though explicitly requiring this in the data sample results in a cleaner sample, the bias to $\langle u_{\parallel} \rangle$ is difficult to quantify and outweighs the background reduction.

$\phi_{\nu,\text{jet}} > 150^\circ$. Thus the background estimate is 0.2% and because the background is small, the estimate itself is taken as the uncertainty. This background is not included in the model, but is treated by a correction applied to the fitted W mass.

$Z \rightarrow \tau\tau$ Background from the process $Z \rightarrow \tau\tau$ is estimated using HERWIG [46] and a slower but more detailed detector simulation to deal with possible hadronic decays of the other tau meson. Here, as in the case of $W \rightarrow \tau\nu$, the available energy is split among many final-state particles and results in a much smaller background. It is estimated to be $(0.05 \pm 0.05)\%$. Here again a correction is applied to the fitted M_W rather than including the background in the W mass simulation.

Cosmic Rays Cosmic rays traverse the detector at random times with respect to event interaction times. This out-of-time nature makes them difficult to model in any precise way. For this reason, a number of methods are used to search for them. The requirement that no other tracks in the event have $p_T > 10$ GeV/c (see Table 4.1) removes cosmic-ray events where both tracks are found. Most of the cosmic-ray events where only one track is found are removed by the combination of $|z_{\text{vertex}} - z_o| < 2$ cm and $|d_o| < 0.2$ cm. The number of cosmic rays remaining in the final sample is estimated using events which fail the $|z_{\text{vertex}} - z_o| < 2$ cm or $|d_o| < 0.2$ cm criteria, but which pass all the other selection cuts. A control sample of identified cosmic-ray events is formed from these events by visual inspection. The d_o and $z_{\text{vertex}} - z_o$ distributions of this control sample are used to estimate the background in the regions $|z_{\text{vertex}} - z_o| < 2$ cm and $|d_o| < 0.2$ cm. An independent estimation of the remaining cosmic ray background is made looking either for a track in the muon chambers back-to-back in ϕ with the muon candidate or for timing information from the hadron calorimeter indicating an out-of-time particle. This independent study gives a result consistent with the above study. The expected number of cosmic-ray events in the final sample is $0.5_{-0.5}^{+2.0}$ and no correction is applied to the fitted mass.

Background	# of events	(%)
$Z \rightarrow \mu\mu$	118 ± 16	3.6 ± 0.5
$W \rightarrow \tau\nu$	25	0.78
Jets/Fakes	6 ± 6	0.2 ± 0.2
$Z \rightarrow \tau\tau$	1.5 ± 1.5	0.05 ± 0.05
Cosmic rays	$0.5^{+2.0}_{-0.5}$	$0.02^{+0.06}_{-0.02}$
Total	151 ± 17	4.65 ± 0.54
Total (simulation)	143 ± 16	4.38 ± 0.50
Total (correction)	8 ± 7	0.27 ± 0.22

Table 8.1: Summary of backgrounds. The number of events are for the signal region of $65 < M_T < 100$. The separate totals are for backgrounds that are included in the simulation ($W \rightarrow \tau\nu$ and $Z \rightarrow \mu\mu$) and for backgrounds that are applied as a post-fit correction to the W mass (all others).

Table 8.1 summarizes the amount of backgrounds present in the W mass signal region. Figure 8.3 is a plot of the final simulation M_T distribution including the $Z \rightarrow \mu\mu$ and $W \rightarrow \tau\nu$ backgrounds. The effect of the backgrounds on the measured W mass are discussed in Chapter 10.

8.2 Radiative Corrections

The Born-level calculation used in the W mass simulation does not include the radiative-correction diagrams of Figure 8.4. These are simulated using a calculation by Berends and Kleiss [37, 38]. Figure 8.5 contains plots of M_T both with and without radiative diagrams. The change in the shape of M_T affects the fit value and forces a correction to be made to the fitted mass (see Chapter 10 for both the correction and the uncertainty). Including the radiative diagrams in the W mass simulation results in a significantly slower simulation which, because of the nature of the fitting algorithm (see Chapter 9), makes it impossible to use.

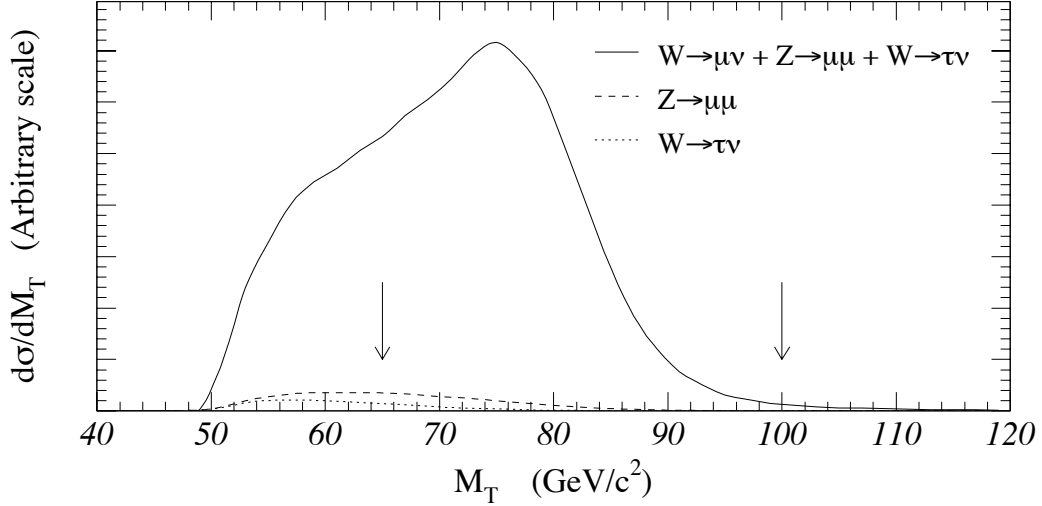


Figure 8.3: Simulated M_T distribution including backgrounds. The $Z \rightarrow \mu\mu$ and $W \rightarrow \tau\nu$ backgrounds are also plotted separately to compare with the $W \rightarrow \mu\nu$ signal. The arrows indicate the fit region.

Uncertainties in the radiative effects on the W mass are estimated from uncertainties both in the theoretical calculation and in the detector response to a photon. The Berends and Kleiss calculation does not include all the radiative Feynman diagrams. It does not include initial-state radiation (t - and u -channel diagrams) and it includes only half of the $W\gamma$ vertex diagram; however, this is not as bad as it may seem. The initial-state radiation, since it is off a quark line, does not directly affect M_W . The $W\gamma$ vertex diagram is split into two components: an on-shell W radiating a photon and decaying into an off-shell W (radiative decay), and an off-shell W radiating and decaying into an on-shell W (radiative production). The latter is not included in the calculation³ because like initial-state radiation, it results in a real W and does not affect M_W . The effects of the missing diagrams are evaluated using a calculation by Baur and Berger [39]. Their calculation includes initial-state radiation, all of the $W\gamma$

³Which diagrams, or parts thereof, to include is based on gauge cancellations between diagrams. The explanation given here is qualitative. For details, read the article ([37]).

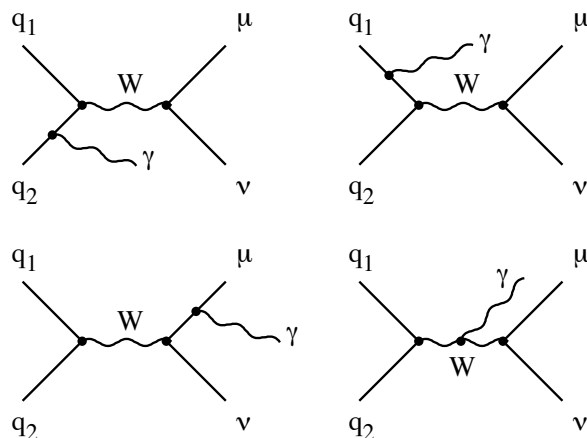


Figure 8.4: Top: Initial-state radiation diagrams. The photon is emitted from an incoming quark and is uncorrelated with the muon direction. Bottom: Final-state radiation and the $W\gamma$ vertex. Final-state radiation is responsible for most of the radiative effects.

vertex diagram, and the final-state radiation, but treats the muon as massless. This massless muon results in errors at small photon energies. A vertex correction diagram, which cancels the infrared divergences in the final-state radiation diagram and alters the energy distribution of the photons, is also not included in the Baur and Berger calculation. Using the complementary nature of these two calculations, one *can* consider kinematic regions where both should be valid and use these regions to establish a normalization point from which to extrapolate to regions where the excluded diagrams are important. These excluded regions are used to determine the uncertainty associated with the missing diagrams (see Chapter 10).

The uncertainty in the detector response to photons is another source of uncertainty and is studied using photons well-separated from the W decay muon. The photon energy threshold, the photon fiducial region, and the photon energy resolution are all varied resulting in nearly negligible effects.

Radiative decays also affect the measurement of \vec{u} . Most photons are from the radiative muon diagram and tend to be collinear with the muon, often impacting the

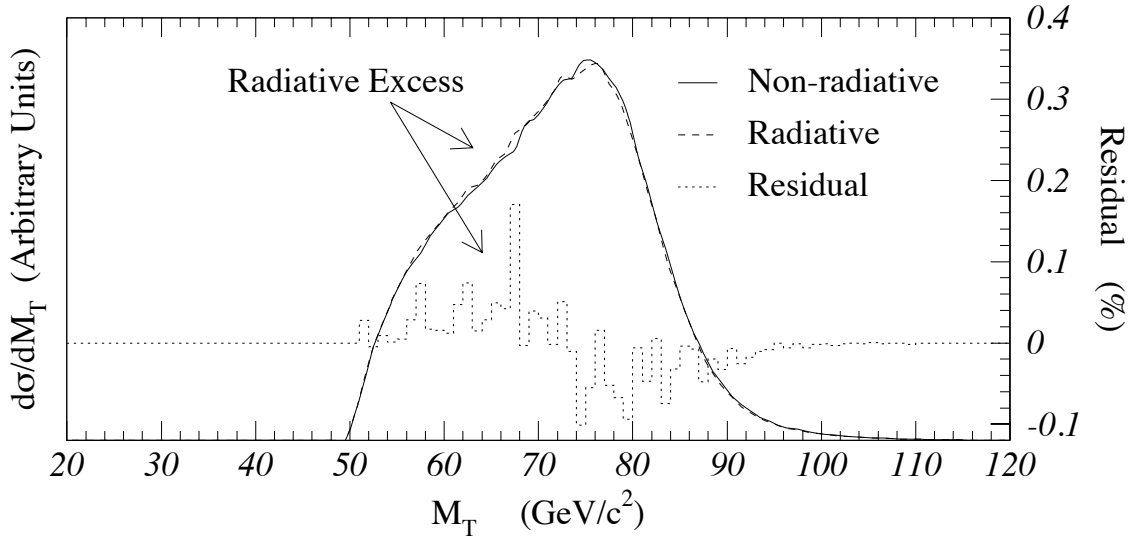


Figure 8.5: Radiative and non-radiative lineshapes and the residual of them in percent. The residual is the difference divided by the area under the radiative distribution.

same calorimeter tower as the muon (see Figure 8.6). Some fraction of these events are removed by the tower energy cut (Section 4.5). In the remaining events, the photon energy is thrown out by the muon removal procedure (Section 6.1). Photons not striking the same calorimeter tower as the muon are not removed and are included in the calculation of \vec{u} , changing $\langle u_{\parallel} \rangle$. The effect is to make $\langle u_{\parallel} \rangle$ more positive since the photon is preferentially aligned with the muon. Photons from the other diagrams are uncorrelated with the muon and while they may affect the measured mass of the W , they do not affect $\langle u_{\parallel} \rangle$. The net effect on $\langle u_{\parallel} \rangle$ from radiative decays is determined to be $\sim +75$ MeV, and is included in the simulation of u_{\parallel} (recall that radiative effects in M_T are handled by a post-fit correction).

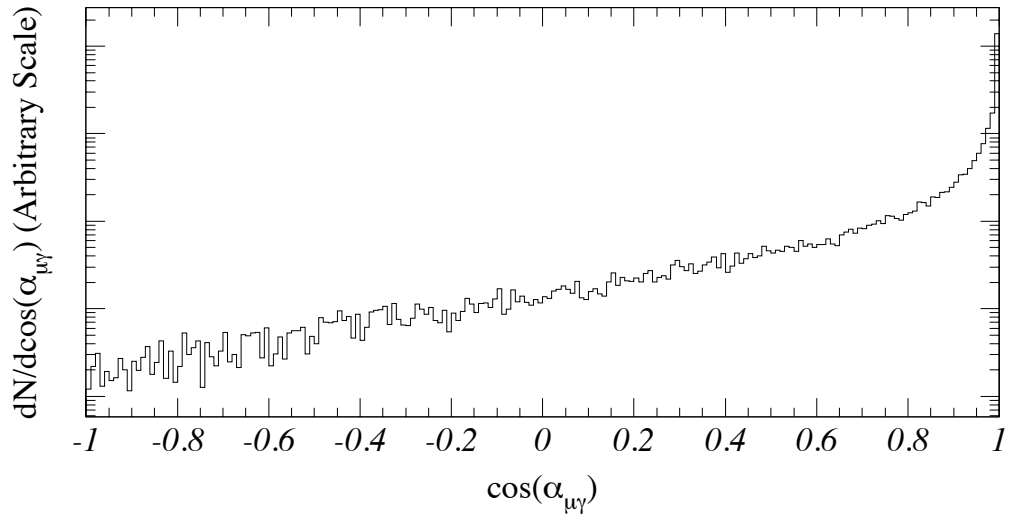


Figure 8.6: The cosine of the angle between the photon and the muon for radiative events. The y-axis is logarithmic.

8.3 Summary

The largest background processes in the W mass data sample are $Z \rightarrow \mu\mu$ and $W \rightarrow \tau\nu$ and are included in the simulation. Corrections are made to the fitted mass to account for those backgrounds which are not added to the simulation and to account for the radiative decay $W \rightarrow \mu\nu\gamma$.

Chapter 9

W Mass Fit

In this chapter, the third part of the measurement, the fitting of the simulated lineshapes¹ to the data, is presented. The fitting procedure is documented and the consistency and robustness of the procedure is verified.

9.1 Fitting Algorithm

The fitting method uses a simulated lineshape (described in Chapters 7 and 8) as the fitting function, \mathcal{F} . This lineshape is a distribution in M_T and is parameterized by M_W and Γ_W (the mass of the W and the intrinsic width of the W ; see Chapter 2); thus, the fitting function takes on the form $\mathcal{F}(M_T; M_W, \Gamma_W)$. This is entirely analogous to fitting a line to a set of data points. A comparison of these two situations reveals

$$\begin{array}{lcl} \text{Line} & \longrightarrow & \mathcal{F} = mx + b = \mathcal{F}(x; m, b) \\ W \text{ Mass} & \longrightarrow & \mathcal{F} = ??? = \mathcal{F}(M_T; M_W, \Gamma_W) \end{array} \tag{9.1}$$

¹The term lineshapes is a throwback to atomic emission spectra, where lineshape referred to the energy (or frequency) distribution of the emitted photons. This is analogous to the emission of muons from the W and so the term lineshape is used.

where the question marks indicate the lack of a simple algebraic expression for \mathcal{F} . In the case of the line, the fitting procedure finds the values of the slope and intercept (m and b). In the W mass case, the fitting procedure finds the values of the mass and width (M_W and Γ_W).

In the traditional least squares fit, the χ^2 between the data and the fitting function is minimized with respect to the parameters of the function (m and b in the linear fit). The χ^2 uses the difference between the function values at each x_i and the corresponding data values, y_i . A consequence of this is that the data has to be in the form of coordinate pairs, (x_i, y_i) . In the case of the W mass fit, the data consists of a single value, M_T . The second coordinate must be artificially constructed by creating bins in M_T resulting in the form (M_{T_i}, N_i) where M_{T_i} is the average value of M_T covered by bin i , and N_i is the number of events that fall within that range. This forced binning may introduce systematic errors into the fit. To avoid these errors, the maximum likelihood method [47], which does not require data binning, is utilized. In a maximum likelihood fit, the likelihood quantity (see below) reaches a maximum value for those values of the parameters which best describe the data being fit (analogous to the χ^2 in a least squares fit which reaches a minimum value). The likelihood is defined as

$$\mathcal{L}(M_W, \Gamma_W) = \prod_i \mathcal{P}(M_{T_i}; M_W, \Gamma_W). \quad (9.2)$$

where the product is over all events and \mathcal{P} is related to the fitting lineshape, \mathcal{F} , by a normalization constant,

$$\mathcal{P}(M_T; M_W, \Gamma_W) = \frac{\mathcal{F}(M_T; M_W, \Gamma_W)}{\int_{\text{FitRegion}} dM_T \mathcal{F}(M_T; M_W, \Gamma_W)}. \quad (9.3)$$

This function, \mathcal{P} , is the probability density for observing a given M_T , which makes the likelihood the joint probability density of observing some unique set of M_T values.

When implementing a likelihood fit, a number of reasons make it more practical to use the negative of the natural log of the likelihood ($\ell = -\ln \mathcal{L}$). First, near the maximum likelihood value, \mathcal{L} is a gaussian function of M_W and Γ_W . Therefore, ℓ is a quadratic function of M_W and Γ_W which simplifies the task of locating the maximum². Second, the minus sign changes the maximum to a minimum which allows the use of commercial software built to find minimums, not maximums. The negative log-likelihood version of Equation 9.2 is

$$\ell = -\ln \mathcal{L}(M_W, \Gamma_W) = -\sum_i \ln \mathcal{P}(M_{T_i}; M_W, \Gamma_W). \quad (9.4)$$

A more detailed description of the maximum likelihood method can be found in reference [47].

The simulation generates lineshapes (fitting functions, $\mathcal{F}(M_T; M_W, \Gamma_W)$) at discrete values of M_W and Γ_W , containing $\sim 800,000$ events each. The range of values for M_W and Γ_W is $79.2 < M_W < 81.0$ GeV/ c^2 in steps of 0.3 GeV/ c^2 and $1.1 < \Gamma_W < 2.9$ GeV/ c^2 also in steps of 0.3 GeV/ c^2 . Because the simulated lineshapes are binned distributions in M_T , a linear interpolation is performed between bins to obtain a continuous function of M_T . To use these continuous lineshapes, \mathcal{F} , as probability densities, \mathcal{P} , they must be normalized over the M_T fitting region, $65 < M_T < 100$ GeV/ c^2 (see Equation 9.3). Figure 9.1 contains plots of $\mathcal{P}(M_T; M_W, \Gamma_W)$ at various values of M_W and Γ_W .

For each simulated lineshape (each (M_W, Γ_W) point), a likelihood value, $\ell(M_W, \Gamma_W)$, is calculated from Equation 9.4 forming a likelihood surface. As stated earlier, ℓ should have a quadratic dependence on M_W and Γ_W near its minimum; however, to allow for small deviations from quadratic behavior³, the ℓ data points are fit via least squares

²Simple polynomials are easier to deal with than gaussian functions.

³ Γ_W is numerically close to zero, thus it produces slightly asymmetric ℓ values. A cubic term absorbs this asymmetry.

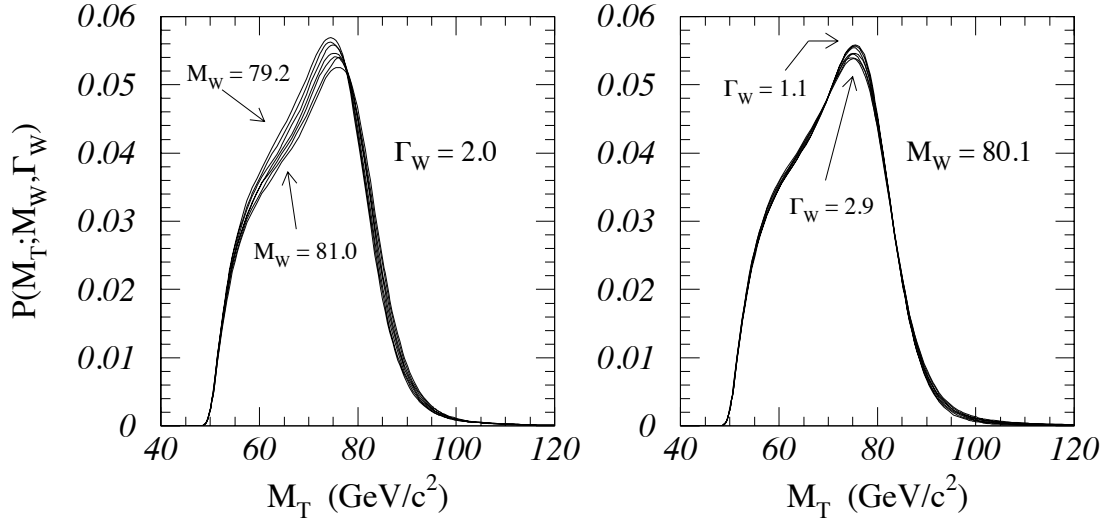


Figure 9.1: Left: Lineshapes at various values of M_W for a fixed Γ_W . Right: Lineshapes at various values of Γ_W for a fixed M_W .

with a third-order polynomial (in M_W and Γ_W),

$$\begin{aligned} \ell(M_W, \Gamma_W) = & a_{30}M_W^3 + a_{20}M_W^2 + a_{10}M_W + a_{03}\Gamma_W^3 + a_{02}\Gamma_W^2 + a_{01}\Gamma_W + \\ & a_{21}M_W^2\Gamma_W + a_{12}M_W\Gamma_W^2 + a_{11}M_W\Gamma_W + a_{00}, \end{aligned} \quad (9.5)$$

where the a_{ij} are determined by the fit and the cross terms handle correlations between M_W and Γ_W . The likelihood surface, ℓ is now a continuous function of M_W and Γ_W .

Once ℓ is determined, the best fit values of M_W and Γ_W (M_W^{FIT} and Γ_W^{FIT}) correspond to the minimum of ℓ ,

$$\frac{\partial \ell}{\partial M_W} = 0 \quad \text{and} \quad \frac{\partial \ell}{\partial \Gamma_W} = 0, \quad (9.6)$$

and are determined by a minimization program, MINUIT [48]. Technically, MINUIT is constrained to search for a local minimum in the region of the ℓ data points because a third-order polynomial has no global minimum. In addition to the values of M_W^{FIT}

and Γ_W^{FIT} , MINUIT also determines the points where ℓ increases by 0.5 above the value at the minimum. These points correspond to the $1\text{-}\sigma$ statistical uncertainty in M_W^{FIT} and Γ_W^{FIT} .

9.2 Tests of the Method

The fitting procedure must satisfy two reliability criteria. First, when the procedure is applied to an ensemble of simulated data samples of a constant size, the average values of the fitted mass and width must be consistent with the mass and width used to simulate the samples. Second, the RMS deviation of the fitted masses and widths of these samples must be consistent with the mean of the statistical uncertainties returned by the fits.

To check these criteria, simulated data samples with 10,000 events are subjected to the fitting procedure. After Fitting 85 of these data samples, the average of the returned masses and widths (Figure 9.2) is seen in to agree with the mass at which they were generated, and their RMS deviations agree with the mean of the statistical uncertainties returned by the fit.

9.3 Fitting the Data

Figure 9.3 shows the polynomial surface, ℓ , and the one and two standard deviation contours in the $M_W\text{-}\Gamma_W$ plane, resulting from the fit to the W mass sample. Recall that the one standard deviation point is where ℓ increases by 0.5 from the minimum value and thus the two standard deviation point corresponds to an increase of 2.0.

To avoid coupling the fitted mass to possible errors in detector resolution modeling, Γ_W is constrained to be 2.064 GeV when obtaining M_W^{FIT} (the dashed line in Figure 9.3). This value of Γ_W is from an indirect measurement using the ratio of W to Z total cross sections [49]. A fitted mass of $M_W^{\text{FIT}} = 80.118 \pm 0.206$ GeV/ c^2 is obtained using this

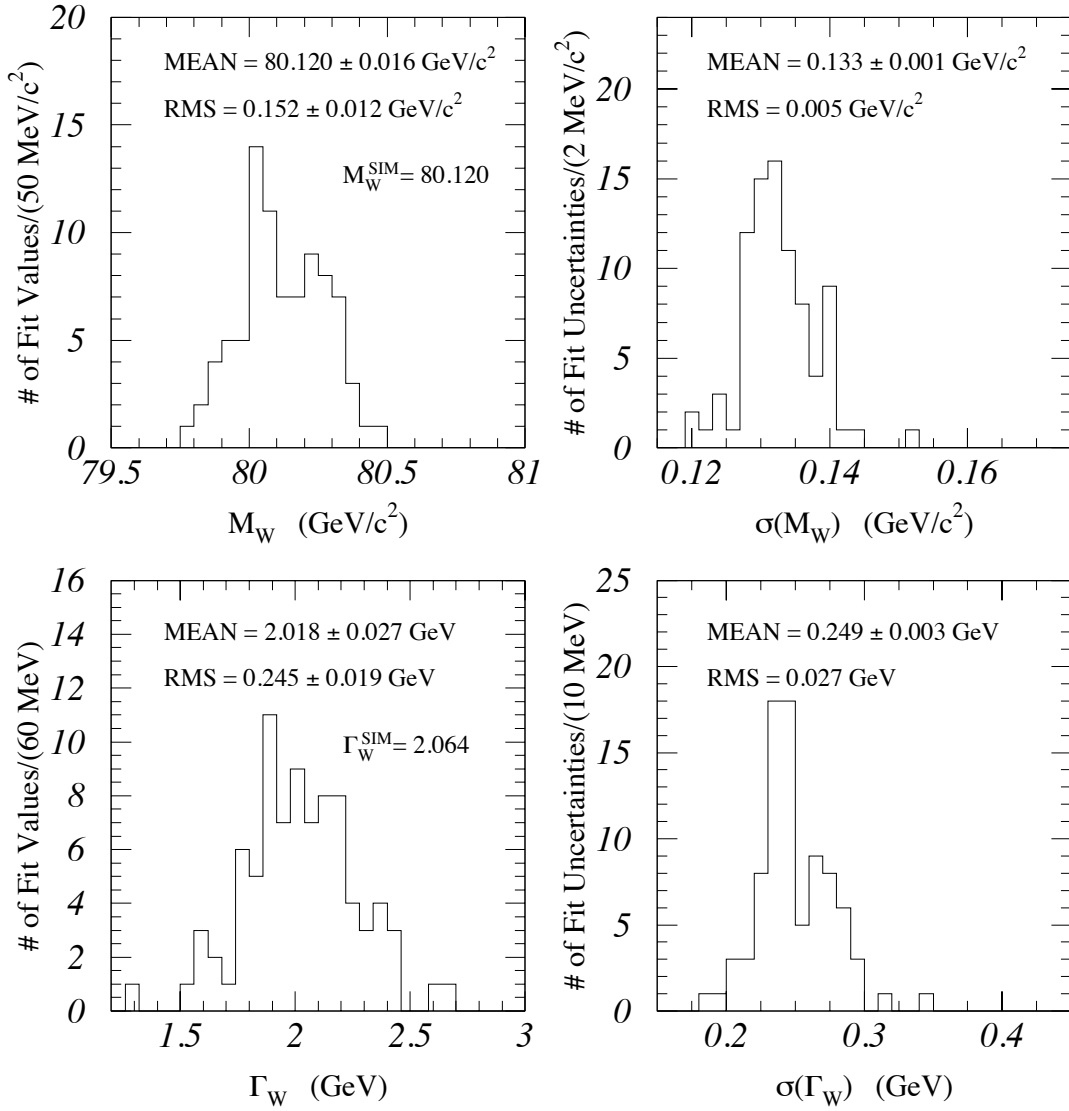


Figure 9.2: The results of fitting simulated data samples of 10,000 events generated at a mass of 80.12 GeV/c² and a width of 2.064 GeV. Top: The distribution of fitted masses (Left) and the distribution of uncertainties (Right). Bottom: The distribution of fitted widths (Left) and the corresponding uncertainties (Right).

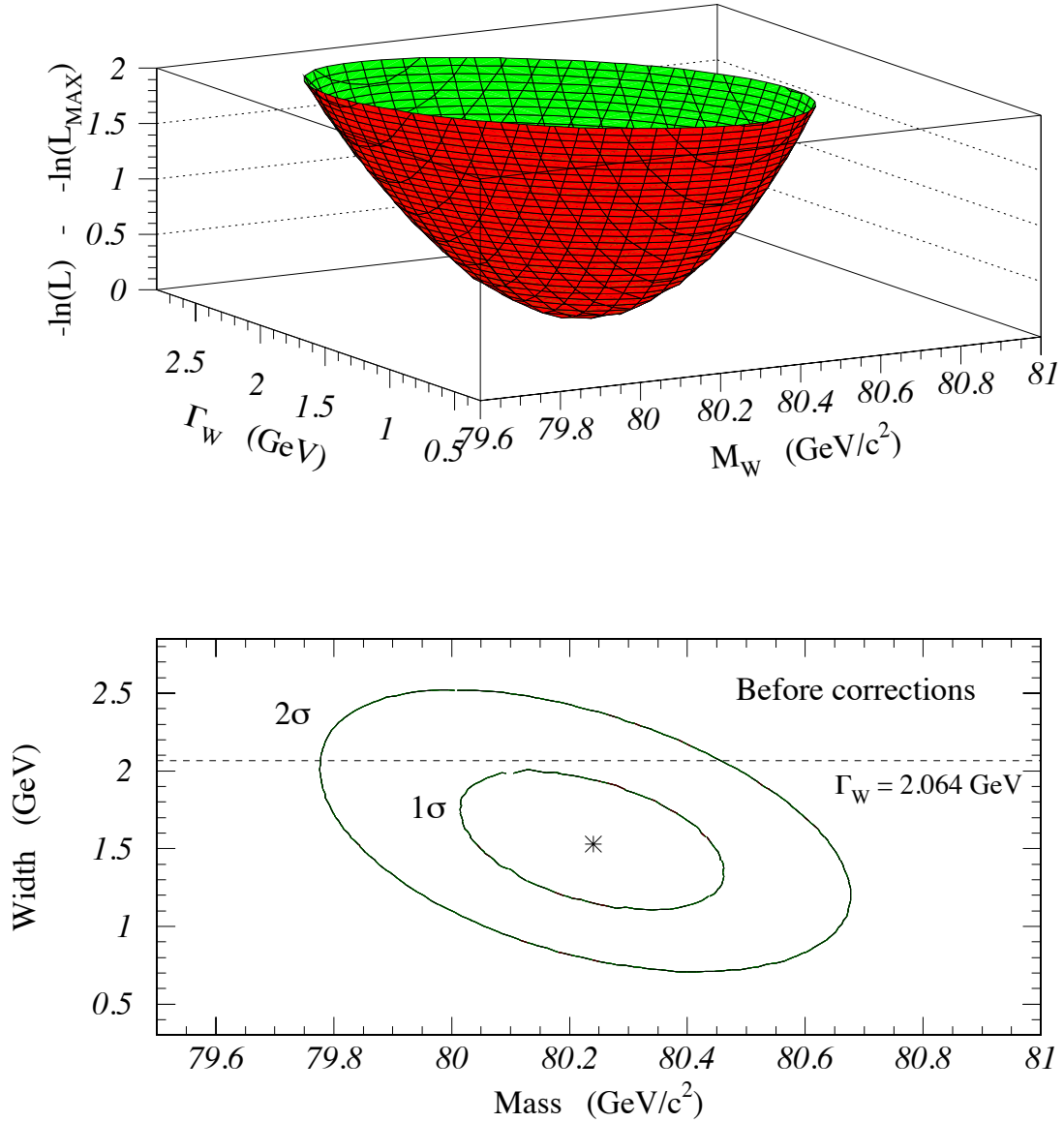


Figure 9.3: Top: The ℓ polynomial surface resulting from the unconstrained fit to the W mass sample. Unfortunately, the ℓ data points cannot be overlaid. Bottom: The $1\text{-}\sigma$ ($\Delta\ell = 0.5$) and $2\text{-}\sigma$ ($\Delta\ell = 2.0$) contours in the M_W - Γ_W plane for the unconstrained fit to the data. The dashed line indicates the constrained fit line. The minimum ℓ on this line is the best fit value, M_W^{FIT} .

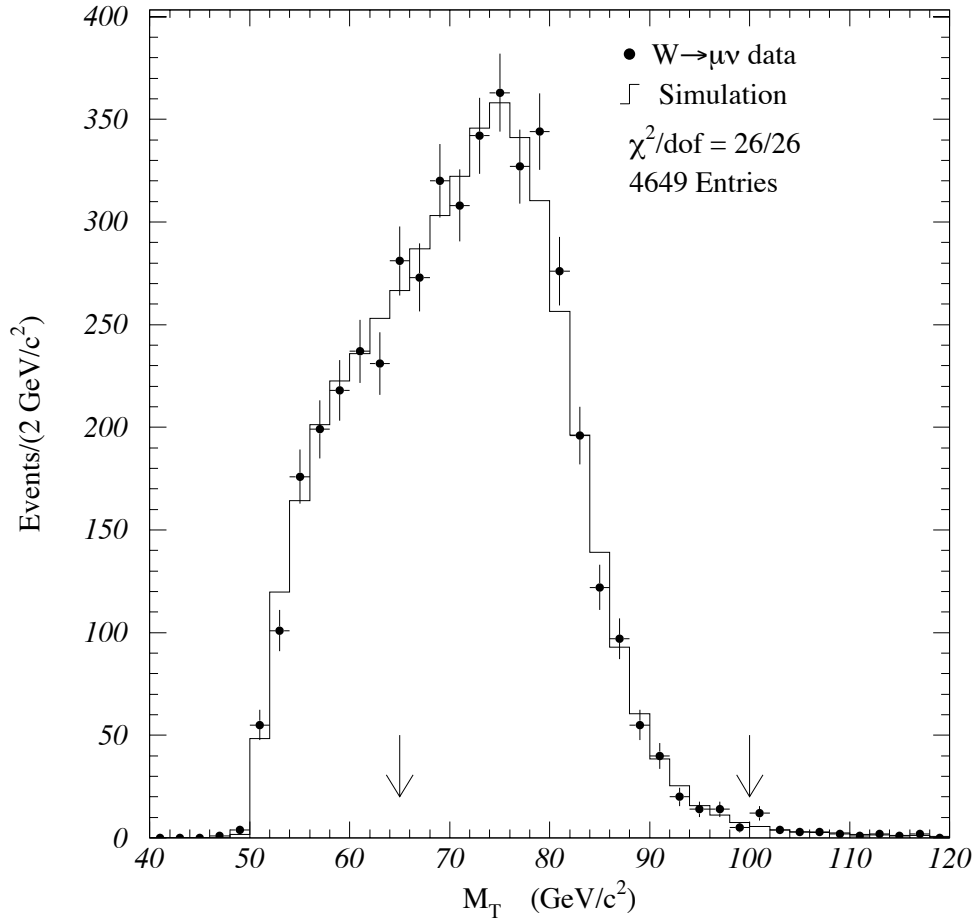


Figure 9.4: The transverse mass distribution for data and simulation. The simulation does not include radiative corrections or small backgrounds. The arrows indicate the fit region.

constrained fit. The values of M_W and Γ_W obtained using the unconstrained fit are discussed in Section 9.5. A comparison of M_T for data and simulation where the simulation is made with the constrained-fit values of mass and width is presented in Figure 9.4. This fitted mass value, M_W^{FIT} , must still be corrected for radiative effects and small backgrounds, neither of which are included in the simulated lineshapes (see Section 9.4).

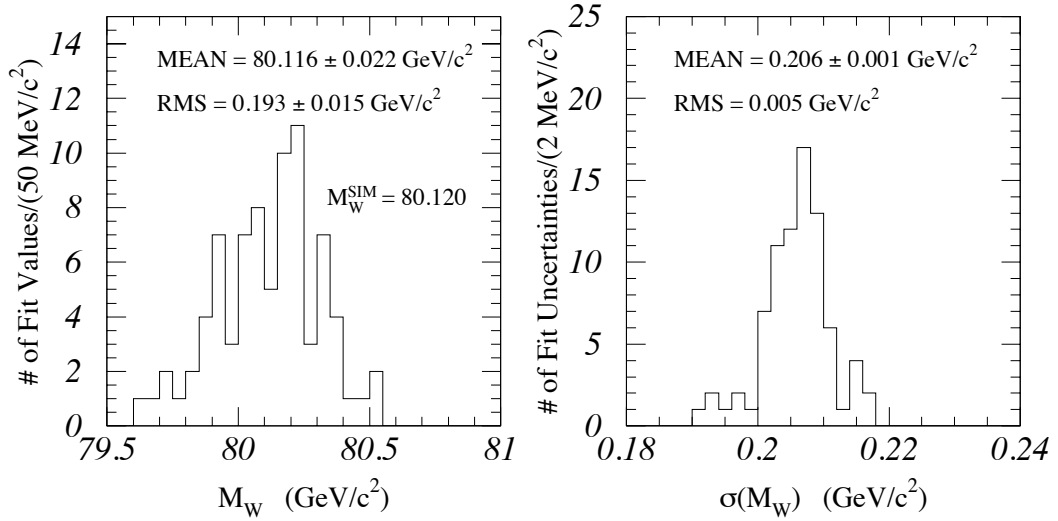


Figure 9.5: The distribution of fitted masses (Left) and uncertainties (Right) for the constrained fit. The mean uncertainty agrees with that returned for the W mass sample.

Since the final fit value is obtained from a constrained fit, this method is checked as in Section 9.2 by fitting simulated data samples. This time the data samples are made with the same number of events as the W mass sample. The results of fitting 80 simulated data samples is shown in Figure 9.5. Note the mean uncertainty returned is consistent with the uncertainty from fitting the W mass sample (206 MeV/c²).

Another test the constrained fitting procedure is to modify the fitting algorithm to use only one parameter, namely the mass. Simulated lineshapes are made with Γ_W always set to 2.064 GeV; thus, Γ_W is no longer a fit parameter. Carrying out this modified fitting procedure yields the ℓ values and polynomial of Figure 9.6. The curve in the figure is actually a parabola as opposed to a cubic polynomial to demonstrate that near the minimum, the ℓ distribution is indeed mostly quadratic. The error bars on the points reflect the finite number of simulated events making up the lineshapes, i.e. the uncertainty in the fitting function. The error this causes in the measured mass is

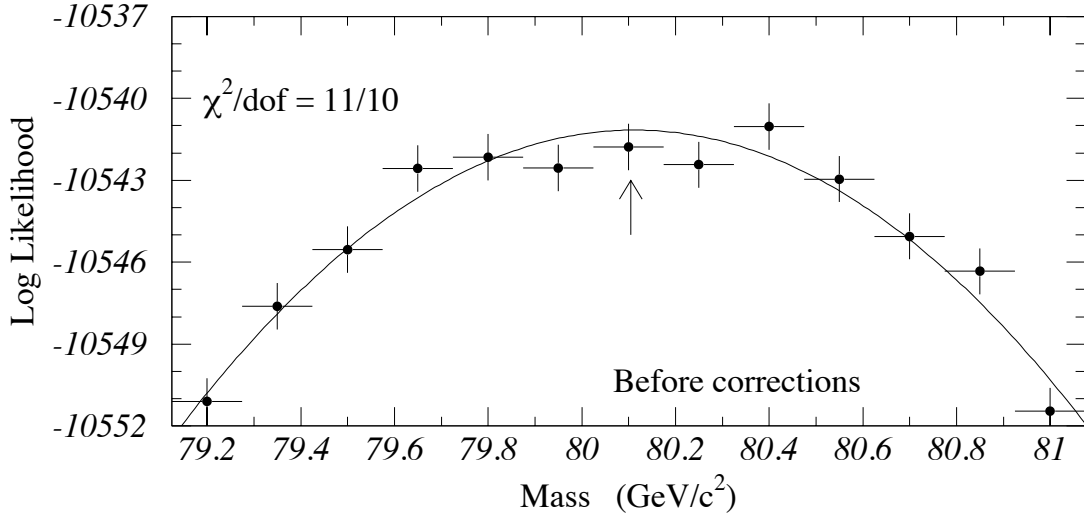


Figure 9.6: The $-\ell$ curve for a one-dimensional fitter. The curve is a quadratic to demonstrate that ℓ fits well to a parabola.

discussed in Chapter 10. The fitted mass value obtained from this fit is consistent with that obtained from the two parameter fit to within the uncertainty in the lineshapes.

9.4 Corrections

The fitted mass, M_W^{FIT} , is corrected for two effects not included in the simulated lineshapes. The first is small backgrounds (see Section 8.1). Fitting simulated data samples that include these backgrounds results in a shift of $-20 \text{ MeV}/c^2$ in the fitted mass. Thus a correction of $20 \text{ MeV}/c^2$ needs to be applied to M_W^{FIT} . The second correction is made to correct for the lack of radiative decay diagrams in the simulation (see Section 8.2). The results of fitting simulated data samples that were made with and without the radiative diagrams (via the calculation of Berends and Kleiss [37, 38]) is summarized in Table 9.1. A correction of $168 \text{ MeV}/c^2$ needs to be applied to the fitted mass. Also included in the table are corrections for use with fitting procedures based on p_T^μ and p_T^ν lineshapes (see Section 9.5). After these corrections are applied, the final

Fit type	ΔM_W^μ (MeV/c ²)	$\Delta \Gamma_W^\mu$ (MeV/c ²)
M_T	$+168 \pm 20$	–
p_T^μ	$+240 \pm 32$	–
p_T^ν	$+45 \pm 30$	–
M_T (Γ_W floating)	$+176 \pm 30$	-36 ± 50

Table 9.1: Corrections to the fitted W mass due to the effects of radiative decays. The last entry is the unconstrained fit to both M_W and Γ_W .

measured mass value is

$$M_W = 80.306 \pm 0.206 \text{ GeV}/c^2. \quad (9.7)$$

9.5 Checks of the Fitting Method

The fitting tests of Section 9.2 check only the internal consistency of the fitting procedure. External checks are made with the W mass sample. The most obvious of these is a comparison of results with Γ_W not constrained in the fit. The fitted mass and width values are correlated because the shape of the transverse mass spectrum is asymmetric. When fitting, the W width behaves like a resolution, i.e. the fitted width compensates for errors in detector resolution modeling; therefore, a comparison of the fitted W width with its expected value serves as a check on the modeling. The measured value for the fitted width after applying the radiative correction in Table 9.1, is

$$\Gamma_W = 1.53 \pm 0.44(\text{stat.}) \pm 0.39(\text{syst.}) \text{ GeV}. \quad (9.8)$$

The systematic uncertainties in the measured width are determined in Chapter 10. The Γ_W measurement is consistent with the indirectly measured value of $2.064 \pm$

M_T (min) (GeV/c ²)	ΔM_W (MeV/c ²)
50	+38 ± 71
55	+47 ± 76
60	+47 ± 60
65	0
70	+63 ± 107

Table 9.2: Variation of the fitted mass as the lower edge of the M_T fitting region is changed. The mass shifts are relative to M_W^{FIT} . The uncertainty is an estimate of the statistical independence between the fitted mass and M_W^{FIT} .

M_T (max) (GeV/c ²)	ΔM_W (MeV/c ²)
90	+42 ± 97
95	-28 ± 49
100	0
105	+37 ± 43
110	+50 ± 46
120	+37 ± 52
150	+22 ± 77

Table 9.3: Variation of the fitted mass as the upper edge of the M_T fitting region is changed. The mass shifts are relative to M_W^{FIT} . The uncertainty is an estimate of the statistical independence between the fitted mass and M_W^{FIT} .

0.085 GeV [49], and also with the directly measured value of 2.040 ± 0.320 GeV [50] and with the Standard Model prediction of 2.067 ± 0.021 GeV [51]. The difference between M_W^{FIT} and the fitted W mass for this unconstrained fit is 123 MeV/c².

Varying the M_T fitting region checks not only the fitting procedure, but also the event modeling and background estimates. The changes in the fitted mass (fitted mass minus M_W^{FIT}) as the M_T fitting region is varied are given in Tables 9.2 and 9.3. Only the transverse mass window is changed for these fits; the event selection is otherwise the same.

An alternative to using the M_T distribution as the fitting lineshape is to use the p_T^μ or p_T^ν distribution as the fitting function. Fits to these distributions are more sensitive to systematic errors in the p_T^W and recoil modeling. The resulting shifts in mass relative to the fitted mass are summarized in Table 9.4. These fits do not have a fit window imposed directly on the distribution other than the indirect requirement⁴

⁴Since M_T , p_T^μ , and p_T^ν are all correlated, a requirement on any one is an indirect requirement on the other two.

Fit Type	ΔM_W (MeV/c ²)
p_T^μ fit	+322 ± 184
p_T^ν fit	-26 ± 143

Table 9.4: Shifts in M_W^{FIT} as the fit type is changed from the transverse mass spectrum to a fit using p_T^μ or p_T^ν . The uncertainties reflect the independent statistical uncertainty between these fits and the M_T fit.

Fit Type	ΔM_W (MeV/c ²)
$ \vec{u} < 5$ GeV fit	+77 ± 240
$5 < \vec{u} < 20$ GeV fit	-80 ± 270

Table 9.5: Shifts in the fitted W mass as the selection cuts are changed from the nominal ($|\vec{u}| < 20$ GeV) to ones covering a different subset of $|\vec{u}|$. The shifts are assigned an uncertainty due to the independent statistical uncertainty. The shifts for the two subsets are expected to be almost completely anti-correlated.

of $65 < M_T < 100$ GeV/c². Even larger deviations than indicated by the statistical estimate might be anticipated since systematic uncertainties increase for these fit types. In Figure 9.7, the p_T^μ and p_T^ν spectra are compared to the Monte Carlo simulation. The simulated distributions use the mass from the M_T fit, M_W^{FIT} , and the constrained width of 2.064 GeV.

The W mass sample can be split into two subsets with $|\vec{u}| < 5$ GeV and $5 < |\vec{u}| < 20$ GeV to further test the simulation and fitting procedure. These two subsets have 1504 and 1764 events respectively. The results of M_T fits to these subsamples is shown in Table 9.5. Although the numbers are split about zero, the shifts are highly anti-correlated so the numbers can be interpreted as only a single check. The M_T distribution for each subset and for the simulation is shown in Figure 9.8.

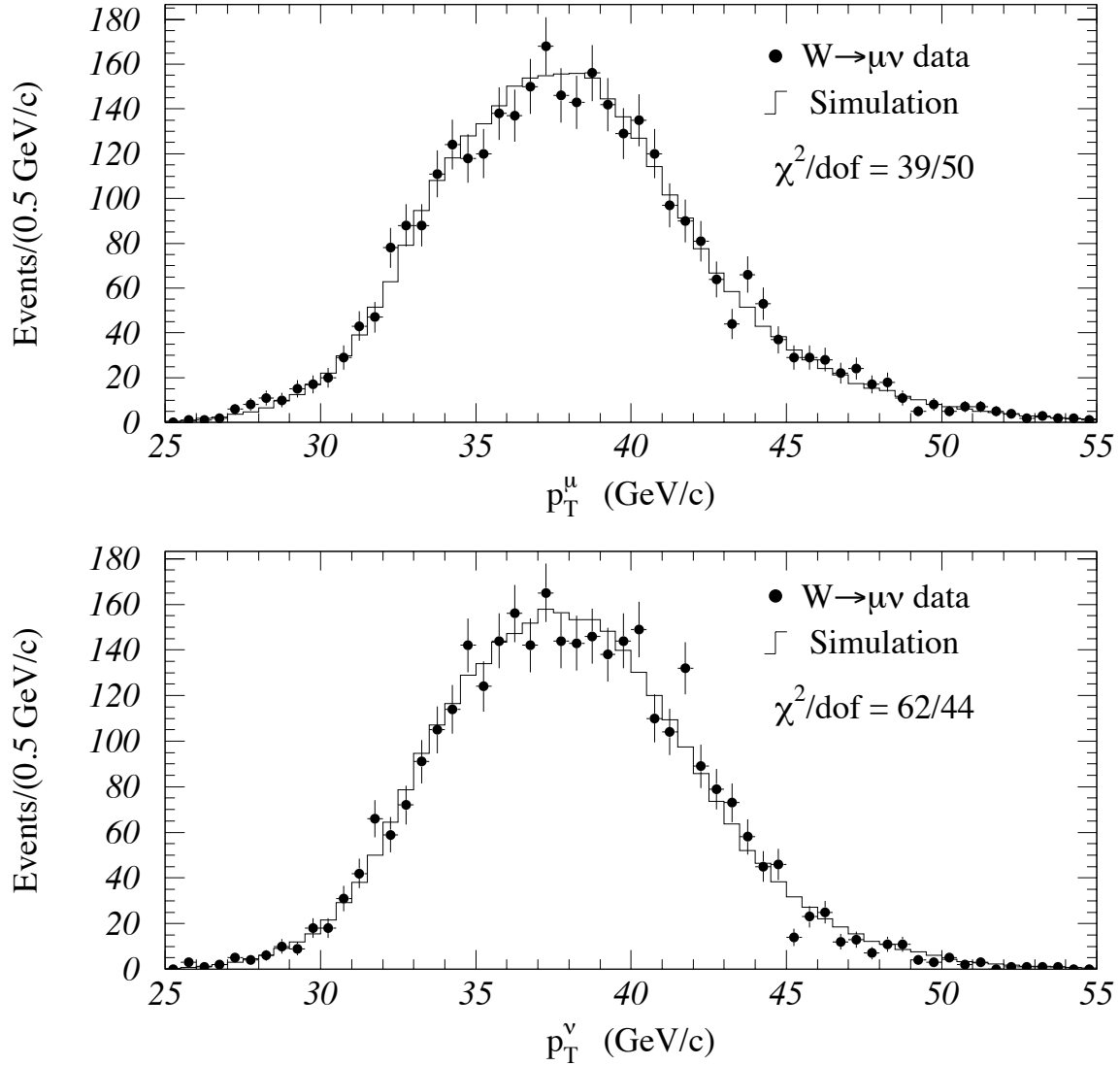


Figure 9.7: Upper: Muon p_T spectrum for the W mass sample compared to simulation. Lower: Neutrino p_T spectrum compared to simulation. The soft edge at ~ 30 GeV/c is due to the M_T window of $65 < M_T < 100$ GeV/c². Note that the mass value used for the simulation comes from a fit to M_T , and not to the distributions shown.

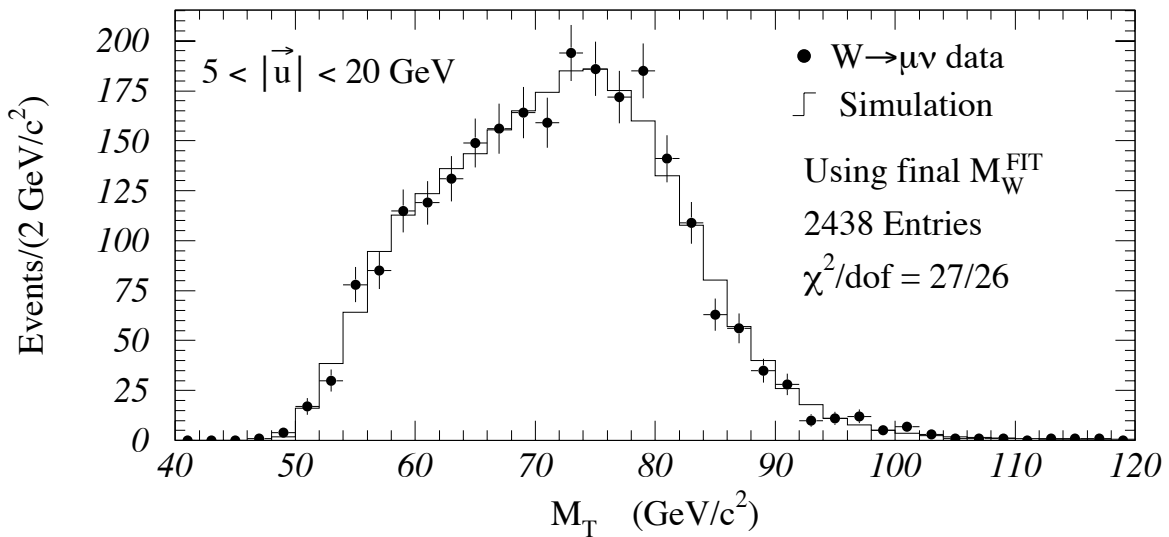
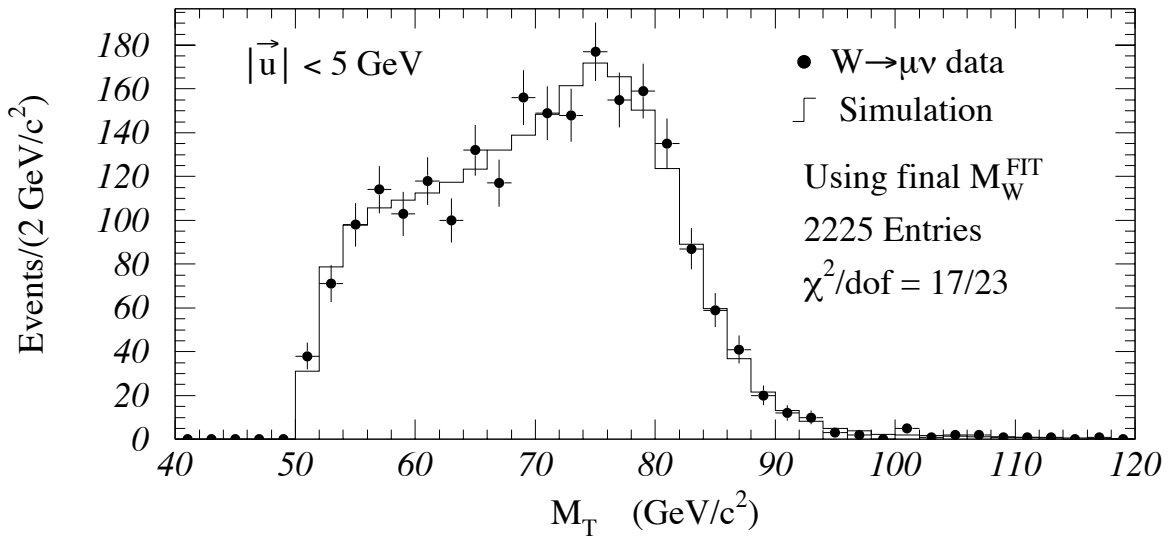


Figure 9.8: Transverse mass spectra of W mass subsamples compared to the Monte Carlo simulation using a mass value of M_W^{FIT} . Upper: $|\vec{u}| < 5 \text{ GeV}$. Lower: $5 < |\vec{u}| < 20 \text{ GeV}$.

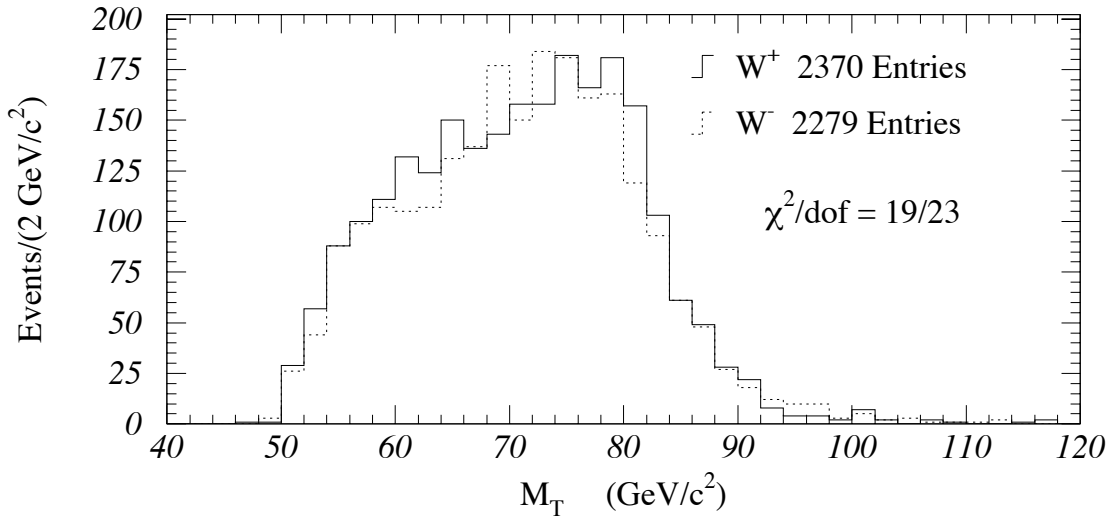


Figure 9.9: The transverse mass spectra of W^+ and W^- .

The W^+ and W^- are expected to have the same mass because of CPT conservation. Indirect tests [52] comparing the decay rates of μ^+ and μ^- are about two orders of magnitude more sensitive to this mass difference than the direct measurement presented here. Dividing the W mass sample by charge, there are 1644 W^+ events and 1624 W^- events (Figure 9.9). The difference between the fitted masses of these two subsets is

$$M_{W^+} - M_{W^-} = +549 \pm 410 \text{ (stat.)} \pm 70 \text{ (syst.) MeV}/c^2, \quad (9.9)$$

where the systematic uncertainty is due to the uncertainty in the alignment of the CTC (see Section 5.2.2.3 and Figure 5.7). The values are consistent within uncertainties.

9.6 Summary

The mass of the W , M_W , is extracted from a maximum likelihood fit to the data. The measured value of M_W after a $168 \text{ MeV}/c^2$ correction for radiative effects and a $20 \text{ MeV}/c^2$ correction for backgrounds is $80.306 \text{ GeV}/c^2$ with a statistical uncertainty

of $0.206 \text{ GeV}/c^2$ determined from the fit. The fitting procedure is checked and passes various tests for consistency and robustness.

Chapter 10

W Mass Uncertainties

In this chapter the final part of the analysis, the determination of the uncertainties in the measured W mass, is described. Where applicable, it contains references to the sections where the source of the uncertainty is discussed.

10.1 Itemization of Uncertainties

The summary of uncertainties in M_W is presented in Table 10.1. The uncertainties associated with the parameters of the simulation are evaluated by fitting simulated data where the parameter under study is varied within its uncertainty. The corresponding shifts in the fitted W mass (using the constrained fit) and the fitted W width (using the unconstrained fit) are taken as the uncertainties due to that parameter. The discussion of each entry in the table of uncertainties follows.

Statistical The statistical uncertainty is obtained from the fitting algorithm (see Chapter 9). The fit to the data returns the uncertainty in the fit parameters. In addition, this uncertainty can be estimated as the average uncertainty returned for simulated data samples with the same number of events as the W mass sample (see Section 9.3; Figure 9.5). The larger of the uncertainties from these two methods is

Uncertainty	ΔM_W^μ (MeV/c ²)	Common (MeV/c ²)
I. Statistical	205	
II. Momentum Scale	50	50
1. J/ψ Normalization	50	50
2. CTC Alignment	15	15
III. Other Systematics	120	90
1. e or μ resolution	60	0
2. p_T^W modeling	45	25
3. Recoil modeling	60	60
4. e or μ ID and removal	10	5
5. Trigger biases	25	0
6. Backgrounds	25	0
7. Radiative correction	20	20
8. W width	20	20
9. Fitting procedure	10	0
10. Parton distribution functions	50	50
11. Higher-order corrections	20	20
TOTAL UNCERTAINTY	240	100

Table 10.1: Summary of systematic uncertainties in the W mass measurement in the muon channel. All uncertainties are rounded to the nearest 5 MeV/c². The uncertainties are added in quadrature to obtain the totals. The last column indicates which uncertainties are common to the electron channel analysis.

$\Delta\delta p_T/p_T^2$ ((GeV/c) ⁻¹)	ΔM_W (MeV/c ²)	$\Delta\Gamma_W$ (MeV)
0.00063	-117 ± 23	-463 ± 45
0.00072	-36 ± 23	-244 ± 45
0.00081	≡ 0	≡ 0
0.00090	+68 ± 23	+220 ± 45
0.00099	+145 ± 23	+430 ± 45

Table 10.2: Variation in the W mass and width as the momentum resolution (see Equation 5.8) is varied from the nominal value by one and two standard deviations. The change in the W width is for the simultaneous fit to both mass and width.

assigned as the statistical uncertainty; however, they happen to be the same in this case.

Momentum Scale The momentum scale uncertainty consists of two parts. First, the J/ψ normalization uncertainty of 50 MeV/c² is extracted from the uncertainty in the measured mass of the J/ψ meson extrapolated to the W mass region (see Section 5.3). Second, an additional uncertainty (CTC Alignment) is incurred from the residual θ -dependent charge splitting of the momentum measurement (Figure 5.6). The charge asymmetry in the muon angular decay distribution (see [53]), when convolved with the above charge splitting, results in a mismeasurement of M_W by 15 MeV/c². Because this is small, it is taken as an uncertainty.

Momentum Resolution The momentum resolution is extracted from the observed width of the $Z \rightarrow \mu\mu$ lineshape (Section 5.4). Table 10.2 lists the variation in fitted mass and width with variation of the momentum resolution from simulated data. The uncertainty in the momentum resolution of 0.00009 leads to an uncertainty in M_W of 60 MeV/c².

r	RMS(u_{\parallel}) (GeV)	RMS(u_{\perp}) (GeV)	ΔM_W (MeV/c ²)	$\Delta \Gamma_W$ (MeV)
1.05	5.19	5.11	-50 ± 23	-114 ± 43
1.08	5.27	5.23	-14 ± 23	-66 ± 43
1.11	5.38	$\equiv 5.30$	$\equiv 0$	$\equiv 0$
1.14	5.57	5.47	$+38 \pm 23$	$+75 \pm 43$
1.17	5.65	5.55	$+90 \pm 23$	$+226 \pm 43$

Table 10.3: Variation of the RMS of u_{\parallel} and u_{\perp} and the fitted mass and width shifts with the scale factor, r . The mass shift is for the fixed-width fit. The width shift is for a simultaneous fit to both the mass and width.

W Transverse Momentum The p_T^W spectrum used as input to the simulation is derived from the p_T spectrum of $Z \rightarrow cc$ events (Section 7.1.2). This spectrum undergoes a linear transformation, $p_T^W(\text{scaled}) = r \times p_T^W$, where r is determined from the width of the u_{\perp} distribution. The uncertainty in r of 0.03 produces an uncertainty in the W mass of 35 MeV/c² and an uncertainty in the fitted width of 95 MeV as shown in Table 10.3.

Additional distortions which change the shape of p_T^W beyond a simple scale factor are studied using two transformations. First, the shape of the p_T^W spectrum is skewed with its mean (9.1 GeV/c) held constant using

$$p_T^W(\text{distorted}) = 9.1 \text{ GeV/c} + s \times (p_T^W - 9.1 \text{ GeV/c}), \quad (10.1)$$

where s is the skew parameter. Second, an alternate distortion of the p_T^W spectrum is investigated by changing the shape of the p_T^W spectrum according to

$$p_T^W(\text{distorted}) = r \times (p_T^W + t \times (p_T^W)^2), \quad (10.2)$$

where l parameterizes this distortion and r is chosen so that the RMS of u_{\perp} agrees with the data (analogous with the simple scale factor r). The bounds on s and l are likewise determined from the data. The results of these distortions are that, within statistical uncertainties, the data are consistent with just the simple scaling. The allowed range of distortions to the shape is taken as an uncertainty of 25 MeV/c² in the fitted mass and 40 MeV in the fitted width.

Recoil Modeling Uncertainties in the recoil modeling result from using $Z \rightarrow ee$ events to calibrate the detector response to the recoil energy (Section 7.2.3). Two effects are investigated: statistical fluctuations arising from the finite size of the Z sample and the effect of electron energy resolution on the measured p_T^Z .

The effect of statistical fluctuations in the Z sample is studied using ~ 20 look-up tables made from simulated $Z \rightarrow ee$ events and a crude recoil model. These simulated tables have the same number of events as the data look-up table and are statistically independent. Simulated data samples are made with each table and fitted. The spread in fitted W mass values using the simulated tables has an RMS deviation of 50 MeV/c² after subtracting out the individual fit uncertainty. The fitted W width values have an RMS deviation of 150 MeV.

An alternative method is to generate simulated data samples which use fewer $Z \rightarrow ee$ recoil calibration events, i.e. a random subset of the look-up table. Fitting these artificial data and using the fact that statistical uncertainties should scale with $1/\sqrt{N}$, where N is the number of events, shows that the finite number of Z events leads to a 50 MeV/c² uncertainty in M_W , consistent with the first method.

The effect of the energy resolution of the electrons on the recoil model is investigated by degrading the electron energy resolution by a factor of two in the p_T^Z measurement and altering the look-up table appropriately. The study results in a shift in the fitted W mass of 35 MeV/c², common to the electron and muon channels. The corresponding uncertainty on the W width is 200 MeV, also common to both analyses. These un-

certainties are checked by comparing results from simulated look-up tables both with the electron energy resolution turned on and with it turned off. Consistent results are observed.

Parton Distribution Functions Recall from Section 7.1.1 that the rapidity of the W is determined from the longitudinal momentum distributions of the initial quarks based on MRS D' parton distribution functions (PDFs) [40]. Varying the parton distribution functions of the proton varies the distribution of the W longitudinal momentum, and therefore, through acceptance effects, alters the lineshape of the transverse mass spectrum. Due to the missing neutrino, the W longitudinal momentum is not directly measurable in W decays. The longitudinal momentum distribution cannot be constrained by the Z data either, since Z production is sensitive to different parton distributions ($u\bar{u} + d\bar{d}$ is different from $u\bar{d}$). However, the longitudinal momentum distribution *can* be constrained using the CDF measurement of the forward-backward charge asymmetry in W decay [53]. This charge asymmetry gets larger as the longitudinal momentum distribution broadens. The asymmetry measurement is directly sensitive to those components of the PDFs which influence W production at the Tevatron, and provides discrimination among parton distributions. The MRS D' set [40] is chosen as the default PDF since it is favored by both the CDF charge asymmetry measurement and deep inelastic scattering experiments [54].

To quantify how well the various PDFs reproduce the data, the weighted mean of the charge asymmetry [53] in the region $0.2 < |\eta| < 1.7$, (A_{PDF}), is calculated for each PDF in Table 10.4. This is compared to the measurement (A_{DATA}) to yield a significance,

$$\zeta = \frac{A_{\text{PDF}} - A_{\text{DATA}}}{\delta A_{\text{DATA}}}, \quad (10.3)$$

where δA_{DATA} is the uncertainty in the mean charge asymmetry measurement. The values of ζ and ΔM_W , ($= M_W^{\text{PDF}} - M_W^{\text{MRS D}'}$) are listed in Table 10.4 and their corre-

PDF	ζ	ΔM_W^μ (MeV/c ²)
CTEQ 2M	+ 4.56	+ 20
CTEQ 2MF	+ 3.76	+ 10
CTEQ 2ML	+ 3.51	+ 14
GRV	+ 3.04	+ 52
CTEQ 2MS	+ 2.94	- 11
CTEQ 1M	+ 2.09	- 1
CTEQ 1MS	+ 1.51	- 24
MRS A (Prelim.)	+ 0.87	- 26
MRS D'_-	+ 0.50	$\equiv 0$
MRS II	- 0.05	- 6
MRS D'_0	- 0.94	- 17
HMRS B	- 1.20	- 35
MT B1	- 3.21	- 76
KMRS B ₀	- 3.59	- 89
MRS B'	- 4.10	- 68
MRS E'	- 4.89	- 96
MRS B		- 45

Table 10.4: Dependence of the W charge asymmetry and the W mass on the PDF [40] choice. The Monte Carlo statistical uncertainty is ~ 15 MeV/c². MRS D'_- is the default choice of the current analysis. MRS B is the default choice of the previously published CDF W mass measurement [9].

lations are shown in Figure 10.1. These correlations between the fitted W mass and the charge asymmetry are expected since a larger charge asymmetry (a larger mean W longitudinal momentum) leads to a smaller average M_T , and hence a larger fitted W mass [55, 56]. The uncertainty in M_W due to the choice of PDF is taken as half the mass difference between points A and B in Figure 10.1, corresponding to $|\zeta| < 2$. This is 50 MeV/c² for the region $65 < M_T < 100$ GeV/c².

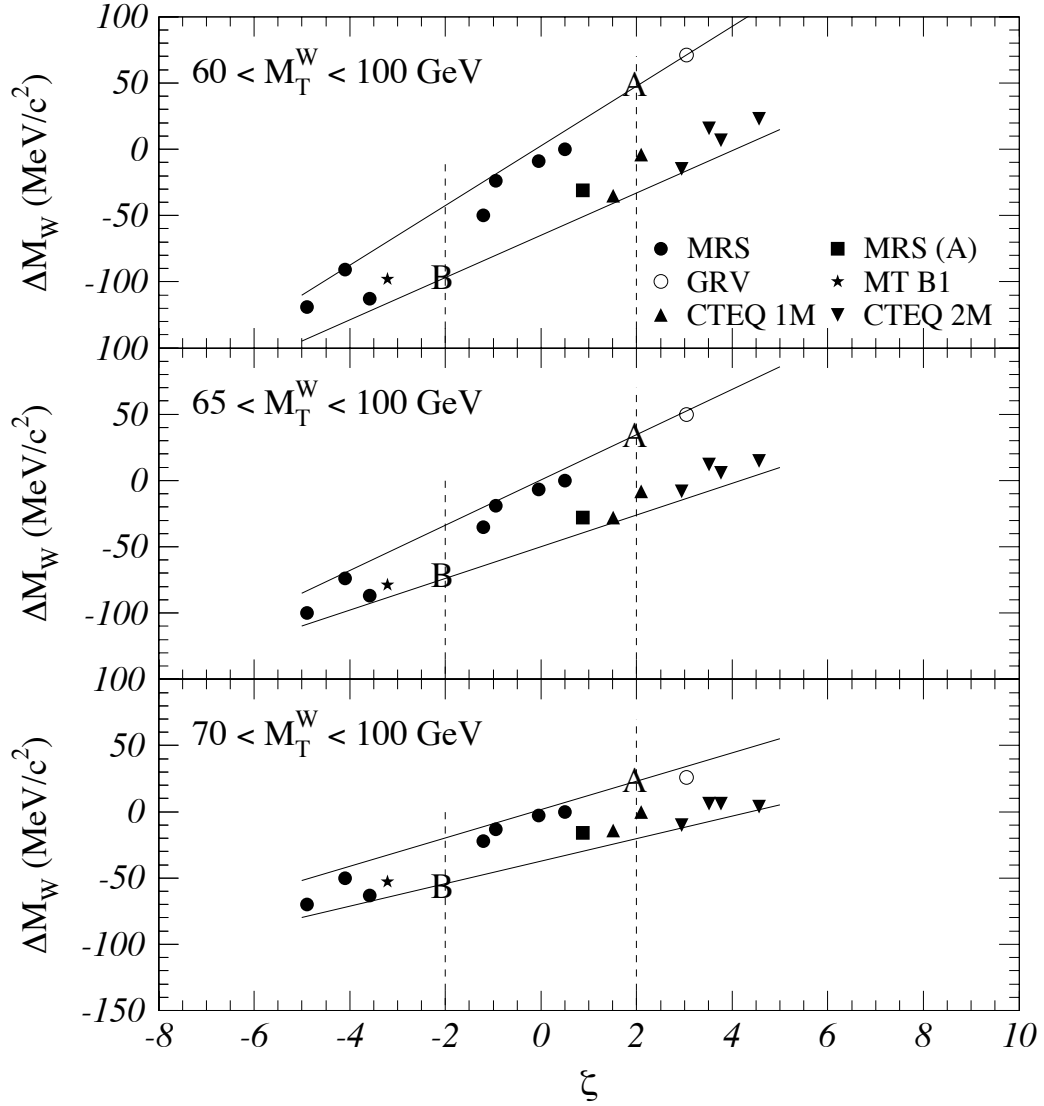


Figure 10.1: The correlation between ΔM_W (MeV/c²) and ζ using various PDFs, where $\Delta M_W = M_W^{\text{PDF}} - M_W^{\text{MRS D}'}$. Three M_T regions are chosen for fitting, Top: $60 < M_T^W < 100$ GeV/c², Middle: $65 < M_T^W < 100$ GeV/c², and Bottom: $70 < M_T^W < 100$ GeV/c². The nominal fitting region is $65 < M_T^W < 100$ GeV/c² (Middle). The solid lines are bounds of different behavior between PDFs. The dashed lines indicate $|\zeta| = 2$. The uncertainty on the W mass is half of ΔM_W between points A and B.

Γ_W (GeV)	ΔM_W (MeV/c ²)
1.664	-102 ± 10
1.864	-50 ± 10
2.064	≡ 0
2.264	+48 ± 10
2.464	+94 ± 10

Table 10.5: Variation in the fitted W mass as the W width is constrained to other than the nominal value. The entries correspond to the ~ 2.5 and ~ 5.0 standard deviation points in Γ_W .

Muon Identification and Removal The muon identification requirements and the act of removing the muon from the calculation of \vec{a} , result in uncertainties in \vec{a} , and therefore M_W (Section 6.2). These effects are small and amount to 10 MeV/c².

Trigger The level-2 trigger (CFT) efficiency as a function of p_T shows no significant p_T dependence (Section 7.2.1; Figure 7.2). The one standard deviation limits on this slope are taken as the uncertainty and data are simulated at these limits and fit to the lineshapes. The corresponding shifts in M_W lead to a 25 MeV/c² uncertainty.

Radiative Corrections The fitted W mass is corrected for the effects of radiative diagrams (Sections 8.2 and 9.4). This correction to M_W is 168 MeV/c². The uncertainty on this number is estimated from uncertainties in the theoretical calculations and in the detector response to the photons from these diagrams. The result is a 20 MeV/c² uncertainty in M_W of which the detector response contribution is negligible.

W Width The measured value of M_W is obtained from a fit where the width of the W , Γ_W , is constrained to the measured value of 2.064 ± 0.085 GeV/c² [49]. Table 10.5 shows the variation in the fitted W mass as the W width is varied in simulated data. Note that the variation in the table is for the ~ 2.5 and ~ 5.0 standard deviation points. The resulting uncertainty in M_W is 20 MeV/c².

Higher-Order Effects The W produced in the simulation is assumed to have no transverse momentum (Section 7.1.1) and, as such, its polarization, P , is parallel/anti-

parallel to the z axis (± 1). With a transverse momentum, the angular distribution of the muons from the decay changes slightly. Chiappetta and Le Bellac [57] have shown that higher-order QCD corrections modify the $\hat{\theta}$ distribution of the muon such that when averaged over charge,

$$(1 + \cos^2 \hat{\theta}) \rightarrow (1 + \cos^2 \hat{\theta}) + a (1 - 3 \cos^2 \hat{\theta}), \quad (10.4)$$

where the coefficient a is always positive. For our W events, a is calculated to be typically 0.007, and is usually less than 0.03. Fitting simulated data with a varied to its limit of 0.03 leads to a 10 MeV/ c^2 uncertainty on the W mass for this effect.

Another higher-order effect is the correlation between the rapidity of the W and the transverse momentum of the W (p_L vs. p_T). In other words, the p_T^W distribution may vary with the longitudinal momentum of the W . This uncertainty is estimated by using a theoretical double-differential spectrum of W production in p_T and rapidity provided by Arnold and Kauffman [42]. This p_T^W spectrum is constrained using the same procedure as used to constrain the spectrum derived from the $Z \rightarrow ee$ data, resulting in an r factor of 0.977. First, as a check, this p_T^W spectrum is used without the rapidity correlation and the fitted W mass shifts by $+20 \pm 10$ MeV/ c^2 . This shift is smaller than the systematic uncertainty due to the uncertainty in r (see above). Turning on the rapidity correlation results in a shift in the fitted mass of 13 ± 14 MeV/ c^2 . Although the shift is consistent with no effect, a 15 MeV/ c^2 systematic uncertainty is assigned.

As stated in Section 7.1.1, the parton distribution functions are evaluated at a Q^2 equal to the generated W mass squared, \hat{s} . The value of Q^2 should reflect not just the mass, but the total center-of-mass energy, including any transverse momentum of the W . To study this, the parton distribution functions are evaluated at $Q^2 = \hat{s} + (p_T^W)^2$ and the effect is found to be negligible.

The total uncertainty from higher-order effects is 20 MeV/ c^2 .

Background	(%)	# of events	ΔM_W (MeV/c ²)
$Z \rightarrow \mu\mu$	3.6 ± 0.5	118 ± 16	-120 ± 20
$W \rightarrow \tau\nu$	0.78	25	-57
Jets/Fakes	0.2 ± 0.2	6 ± 6	-15 ± 15
$Z \rightarrow \tau\tau$	0.05 ± 0.05	1.5 ± 1.5	-5 ± 5
Cosmic rays	$0.02^{+0.06}_{-0.02}$	$0.5^{+2.0}_{-0.5}$	± 5
Total	4.65 ± 0.54	151 ± 17	-197 ± 25
Total (simulation)	143 ± 16	4.38 ± 0.50	-177
Total (correction)	8 ± 7	0.27 ± 0.22	-20

Table 10.6: Summary of backgrounds. The number of events are for the signal region of $65 < M_T < 100$. The separate totals are for backgrounds that are included in the simulation ($W \rightarrow \tau\nu$ and $Z \rightarrow \mu\mu$) and for backgrounds that are applied as a post-fit correction to the W mass (all others).

Backgrounds The largest background processes ($Z \rightarrow \mu\mu$ and $W \rightarrow \tau\nu$) are included in the simulation (Section 8.1). The smaller remaining backgrounds are dealt with as a correction to the fitted W mass (Section 9.4). The uncertainty in M_W is determined from the fractional uncertainty in the background times the shift in the fitted M_W resulting from the presence of the background (or, in the case of $Z \rightarrow \mu\mu$ and $W \rightarrow \tau\nu$, the shift that would have resulted had they not been included in the simulation). The mass shifts and uncertainties are summarized in Table 10.6.

The total $Z \rightarrow \mu\mu$ background uncertainty consists of a contribution from the tracking efficiency, leading to a 20 MeV/c² uncertainty on the W mass, and a contribution from the choice of PDF, giving an uncertainty 10 MeV/c² on the W mass. The $W \rightarrow \tau\nu$ background is precisely simulated resulting in a negligible uncertainty. The background from heavy-flavor decays and fakes is estimated at 0.2%, leading to a shift in the fitted mass of -15 ± 15 MeV/c² assuming an exponentially decreasing p_T spectrum for this background. An upper limit on the number of cosmic rays left in the

data sample is ~ 2 , resulting in a shift of $5 \text{ MeV}/c^2$, which is taken as the uncertainty on M_W . The total uncertainty in M_W from all backgrounds is $25 \text{ MeV}/c^2$.

Fitting Algorithm The fitting function used to fit the data is a Monte Carlo simulation of the M_T lineshape and consists of a finite number of events (Section 9.1) resulting in statistical fluctuations in the lineshapes. This effect is studied by using independent sets of lineshapes and by altering the number of events comprising them. A previous incarnation of this effect was termed “fitter jitter”. An uncertainty of $10 \text{ MeV}/c^2$ is attributed to this jitter.

10.2 Summary

The total uncertainty in the W mass measurement is $240 \text{ MeV}/c^2$ of which $205 \text{ MeV}/c^2$ is statistical, $50 \text{ MeV}/c^2$ is from the momentum scale, and $120 \text{ MeV}/c^2$ is from other systematic uncertainties.

Chapter 11

Conclusion

The mass of the W vector boson was determined from $W \rightarrow \mu\nu$ data taken during the 1992-1993 collider run at Fermilab's tevatron accelerator. The data were fit with a Monte Carlo simulation that included the largest backgrounds. This chapter summarizes the results of this analysis and discusses future prospects.

11.1 Results

The W mass measurement was extracted from a fit to the transverse mass distribution of 3268 $W \rightarrow \mu\nu$ events from 19.7 pb^{-1} of data. The fitted mass value was corrected for the effects of radiative decay diagrams and for the effects of small backgrounds, neither of which were included in the Monte Carlo simulation. The final W mass value is

$$M_W^\mu = 80.310 \pm 0.205 \text{ (stat.)} \pm 0.120 \text{ (syst.)} \pm 0.050 \text{ (scale) GeV}/c^2, \quad (11.1)$$

where “scale” indicates the uncertainty in the absolute momentum scale. This result can be combined with a similar measurement from the $W \rightarrow e\nu$ decay channel [26, 27],

$$M_W^c = 80.490 \pm 0.145 \text{ (stat.)} \pm 0.130 \text{ (syst.)} \pm 0.120 \text{ (scale) GeV}/c^2, \quad (11.2)$$

resulting in

$$M_W = 80.410 \pm 0.180 \text{ GeV}/c^2, \quad (11.3)$$

where the two decay channels have been combined keeping track of the common uncertainties in Table 10.1.

A world-average value for the W boson mass can be calculated by combining this measurement with the previous CDF [11] and UA2 [12] measurements (see Figure 11.1). The value is

$$M_W^{\text{World}} = 80.33 \pm 0.17 \text{ GeV}/c^2, \quad (11.4)$$

where the parton distribution function is assumed to be the only source of common uncertainty¹.

Values for the W mass can be inferred from measurements at the Z pole and from experiments measuring charged currents at low momentum transfer ($Q^2 \ll M_W^2$) under the assumption that there are no new phenomena outside of the Standard Model. Fits to properties of the Z measured at LEP [58] give a value $M_W^{\text{LEP}} = 80.28 \pm 0.07 \text{ GeV}/c^2$. The left-right asymmetry of the Z boson, measured at SLAC [59], is used to infer $M_W^{\text{SLAC}} = 80.79 \pm 0.19 \text{ GeV}/c^2$. Deep-inelastic neutrino scattering measurements are used to infer $M_W^{\text{DIS}} = 80.24 \pm 0.25 \text{ GeV}/c^2$ [54]. Figure 11.1 shows a comparison of the present values for the direct and indirect determinations of the W mass.

¹The largest PDF uncertainty of the three measurements is used as a common uncertainty in combining the numbers.

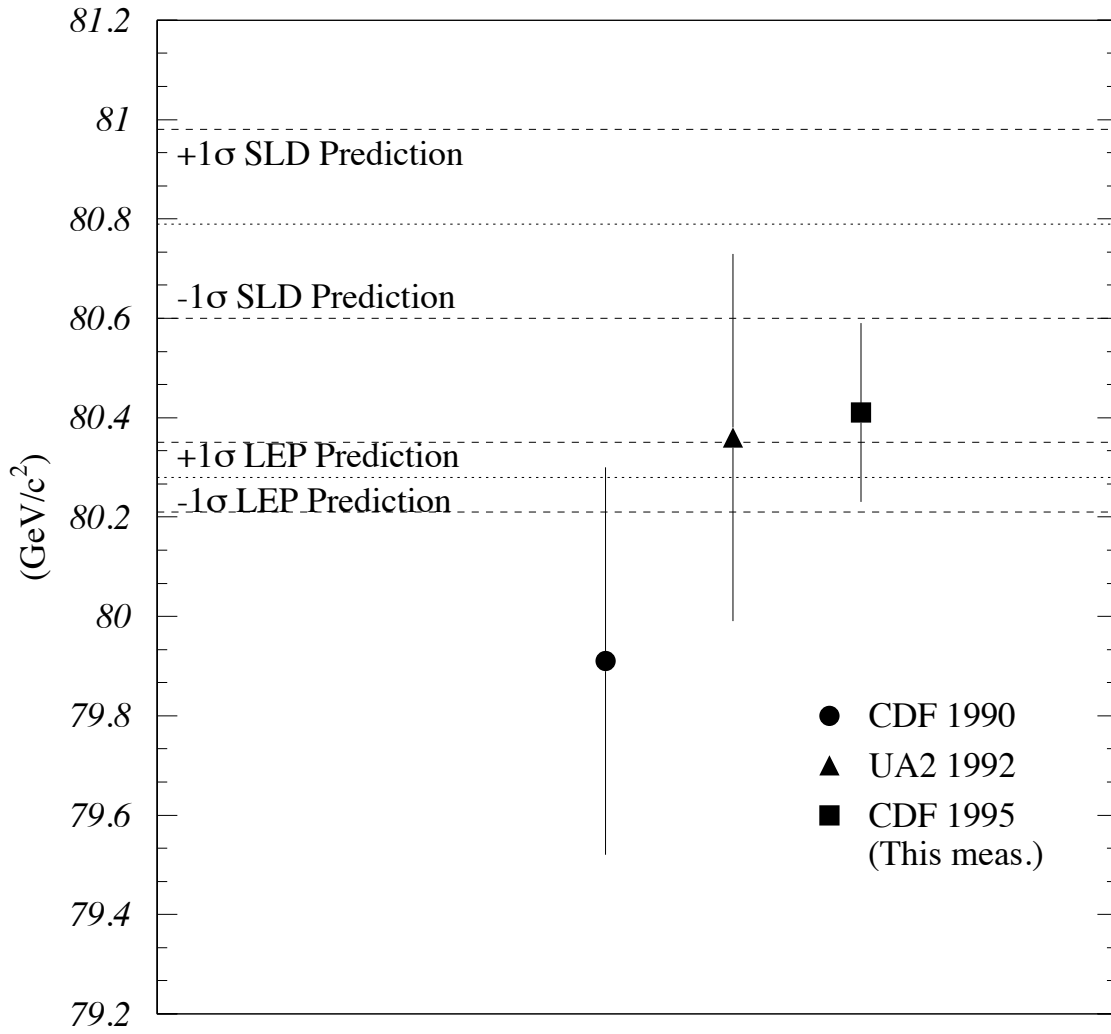


Figure 11.1: Previously published W masses and this measurement compared to the LEP and SLAC predictions.

The direct measurement of the W boson mass can be combined with the top quark mass measurement and other electroweak data to test the consistency of the Standard Model. Figure 11.2 shows a top quark mass of 176 ± 13 GeV/ c^2 [60] and the CDF W mass measurement. Also shown are theoretical predictions [14] of the regions in the M_W - M_{top} plane allowed in the Standard Model for different values of the mass of the Higgs boson. The bands include uncertainties in, among other things, the values of α and α_s at the Z pole [15]. Unfortunately, as this plot shows, the Standard Model is *very* consistent.

11.2 Future Prospects

Currently, CDF is collecting a new data sample with an estimated final size of ~ 100 pb $^{-1}$. This offers a factor of two improvement in the statistical uncertainty of the mass measurement. An additional gain will be made if the CMX muon system is included in the analysis, resulting in greater angular coverage. The present analysis did not use the CMX because it suffered from a high rate of accidental triggers necessitating additional trigger requirements to be imposed which made modeling for the W mass analysis difficult. Thus CMX muons were not used in this analysis.

The advantage of this analysis, or disadvantage depending on your viewpoint, is that all the systematic uncertainties are constrained by data; therefore, as the data sample size increases, not only does the statistical uncertainty decrease, but the systematic uncertainties decrease also. The disadvantage² is that the analysis becomes more and more difficult. As the systematic uncertainties decrease, effects that were ignored previously because they were small, must now be dealt with. One aspect that should be dealt with in the next analysis is the Monte Carlo simulation. The simulation used in the current analysis is a piecewise (and hopefully continuous) combination of

²The use of the word “disadvantage” only reflects the feelings of those projecting this measurement into the future.

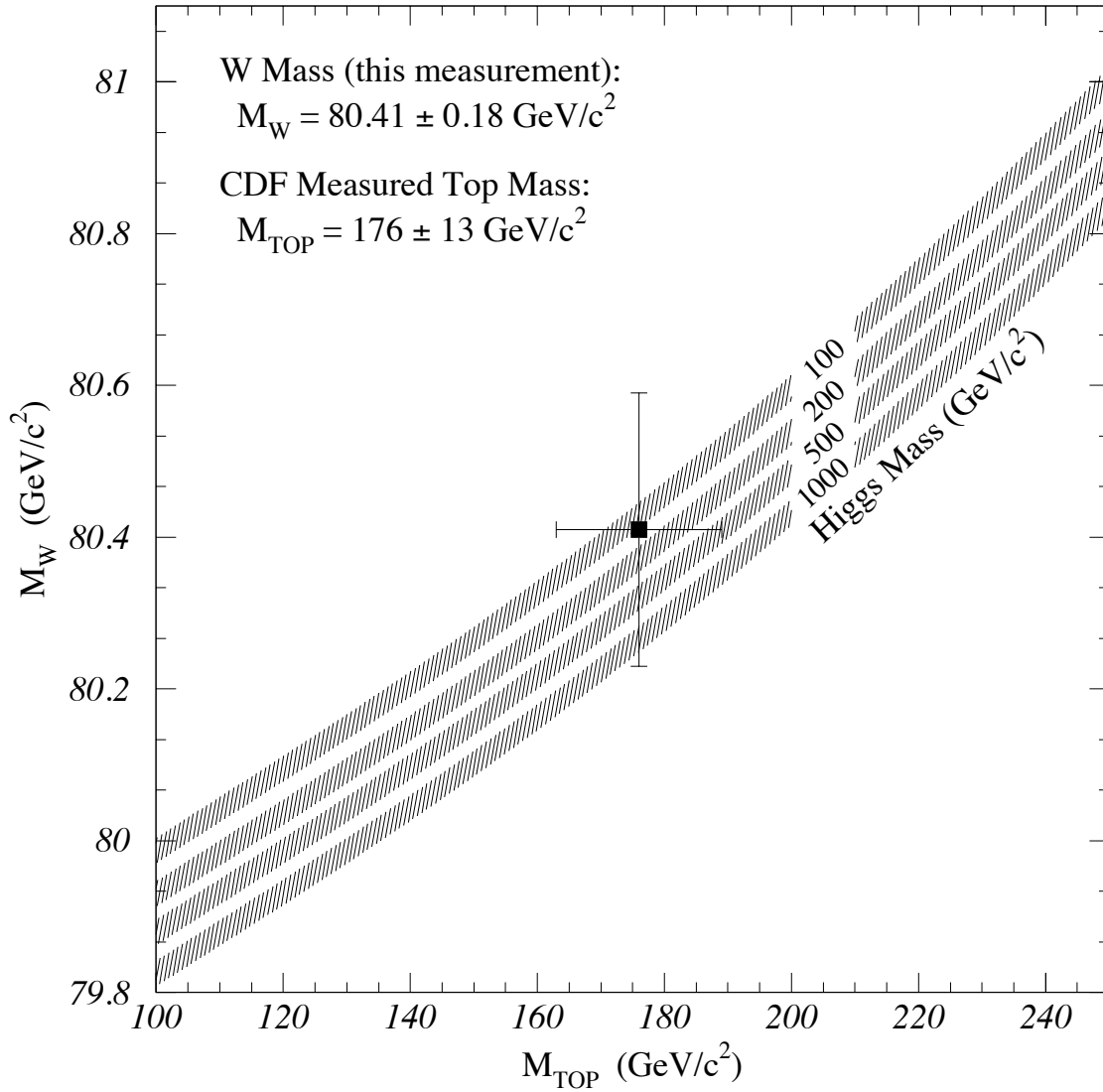


Figure 11.2: The data point is the combined CDF W mass measurement of $80.41 \pm 0.18 \text{ GeV}/c^2$ and a top quark mass of $176 \pm 13 \text{ GeV}/c^2$ [60]. The curves are from a calculation [14] of the dependence of the W boson mass on the top quark mass in the minimal Standard Model using several Higgs masses. The band on each curve is the uncertainty obtained by folding in quadrature uncertainties on $\alpha(M_Z^2)$, M_Z , and $\alpha_s(M_Z^2)$.

various effects. An obvious improvement is to create a fast simulation that includes all the QED radiative diagrams. Including higher-order QCD effects is another possibility, though more difficult than the QED diagrams.

Given that the measurement can be carried out, the uncertainties should scale by $1/\sqrt{N}$ leading to an uncertainty of 90 MeV/ c^2 in the combined muon and electron mass measurement. Of course this is a lower limit barring some new and novel approach to the mass measurement. More likely, it will be a battle to reach 100 MeV/ c^2 in the next analysis.

Appendix A

Construction and Testing of the CMP

The Central Muon Upgrade (CMP) was built to enable CDF to keep pace with the increase in luminosity of the Tevatron collider. The CMP is another set of muon chambers, outside of the CMU, and behind an additional 60 cm of steel. The CMP is used in coincidence with the CMU and thus, because of the additional steel, serves to reduce the trigger rate and enhance the muon identification capabilities of the CMU. The raw trigger rate of the CMU alone is dominated by hadronic punch through. This rate, while manageable at the typical luminosities of $10^{30} \text{ cm}^{-2}\text{s}^{-1}$ experienced in the 1988-1989 run, would have become excessive when the luminosity increased beyond $10^{30} \text{ cm}^{-2}\text{s}^{-1}$ in the 1992-1993 run. Furthermore, in the offline environment, the punch through would have made identification of muons in jets difficult and would therefore have limited the study of semi-leptonic decays of B mesons. Requiring muon candidates to penetrate the additional 60 cm of steel reduced background rates, both at the trigger and at the offline level, by approximately a factor of 20 and enabled CDF to take full advantage of the physics potential of the Tevatron operated at higher luminosities. This appendix documents the design, construction, and testing of the CMP.

A.1 Principle of Operation

Charged particles traversing a gas filled drift chamber such as a CMP chamber ionize the gas and produce electrons, which drift to the anode wire at some velocity, and ions, which drift to the cathode. Upon reaching the wire, the increasing electric field near the wire causes a multiplication of the number of electrons through ionizing collisions between the existing electrons and the gas. This amplified signal becomes available for detection at the end of the wire. An important point is that the velocity at which the electrons drift saturates at some value of the electric field which varies with the type of gas. Knowing this saturated drift velocity makes position measurements possible ($d = vt$). For an in-depth discussion see [34].

A.2 Design

The CMP chambers are rectangular extruded aluminum tubes, 2.54 cm by 15.24 cm in cross section and 6.4 m long, with 2.6 mm thick walls (Figure A.1). This thin, wide shape is necessary because of space limitations on top of the detector. Four of these chambers are glued into a stack with alternate layers staggered by half a cell to eliminate left-right ambiguities.

The chambers have a single 50 μm diameter, gold-plated, tungsten, anode wire down the center and field-shaping cathode pads on top and bottom (Figure A.2). The chambers run in proportional mode, using 50%/50% Ar-C₂H₆ bubbled through isopropyl alcohol at a temperature of -7°C , with the anode at +5400 V and the central shaping strip at +2800 V. Eight shaping strips on either side of the central one have voltages decreasing in equal steps of 350 V towards the outside giving a uniform electric field in the drift volume (Figures A.3 and A.4). The shaping voltages are stepped down by a $20\text{ M}\Omega \times 8$ hybrid divider resistor and are fed through the endplate to the pads by gold plated Cu/Be contact pins inserted in the endplate at

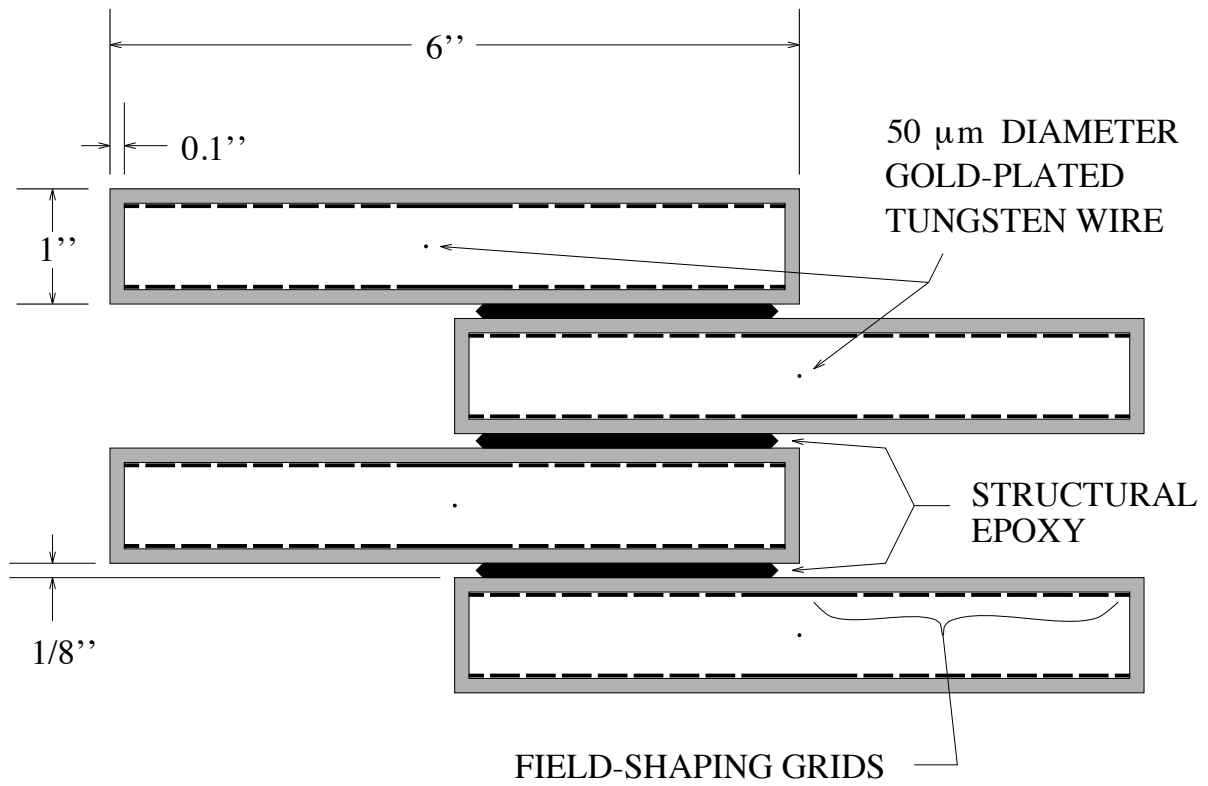


Figure A.1: Cross section of a single stack of chambers showing dimensions and major features.

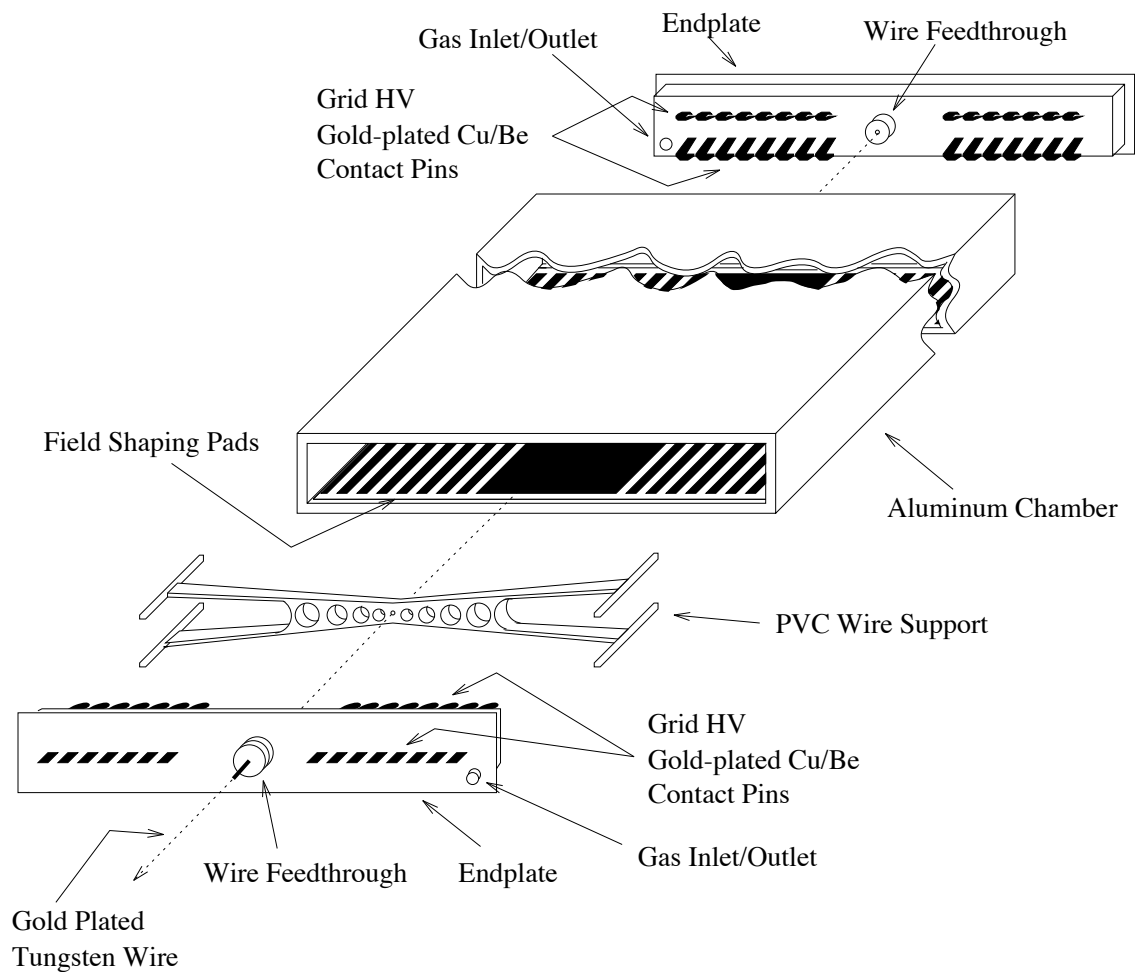


Figure A.2: An exploded view of a CMP chamber showing the endplates, wire support, and field-shaping pads. The scale is not exactly correct in this figure.

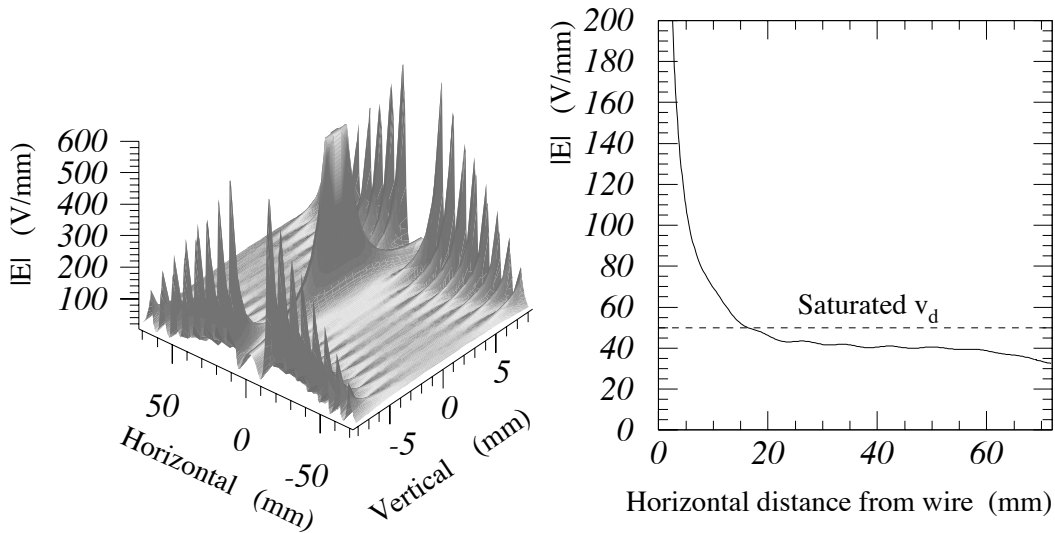


Figure A.3: Left: The electric field values within the chamber. Horizontal specifies the long direction and vertical the short direction. Right: The electric field values along the horizontal at the center of the chamber. The values are from a solution of the potential problem, using a simultaneous over-relaxation method.

molding. The divider resistor is mounted on a printed circuit board that is soldered to the gold plated contact pins on the outside of the endplate. The edge shaping strips are grounded to the aluminum tube by conductive epoxy and are half the width of the rest of the strips to keep the equipotential lines at the edge of the chamber the same shape as those for the rest of the strips (Figure A.4).

Both positive and negative pad voltages were experimented with. The negative version however, required a separate shaping pad on the side wall which had a tendency to arc to the corner of the extrusion and so this version was discarded in favor of positive voltage on the pads. The choice of 2800 volts gives a nearly saturated drift velocity¹ while keeping the wire voltage at a manageable level. With the pads at 2800 V and the wire at 5400 V, the chambers have a measured gain of about 6×10^4 while

¹The drift velocity saturates for an electric field of greater than ~ 50 V/mm (refer to Figure A.3).

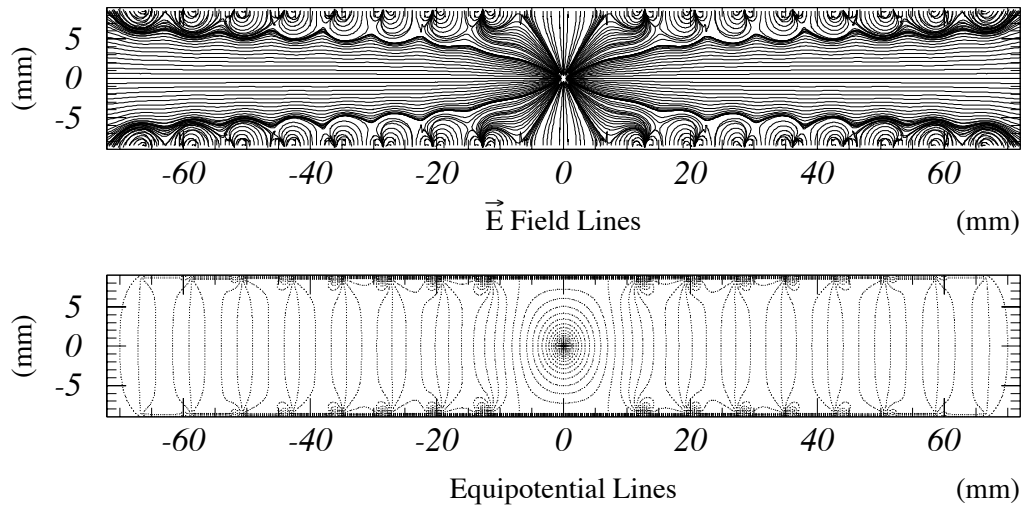


Figure A.4: Top: The electric field lines within a CMP chamber.
Bottom: The equipotential lines within the chamber.

staying several hundred volts away from streamer mode² Avoiding streamer mode is important because part of the upgrade will be hit by spray particles from the overhead bypass of Fermilab’s Main Ring. These particles produce large currents in streamer mode chambers which can cause the high voltage power supplies to sag or trip. The 6.4 m length of the chambers necessitates the use of a wire support (Figure A.2) in the center of the chamber to protect against electrostatic wire instability. The wire support consists of a PVC main body and 5 cm long PVC legs which vary in size by up to $\sim 200 \mu\text{m}$ allowing a custom fit to each chamber and using friction to keep the wire support in place.

²Streamer mode refers to a process where high amplification takes place at the wire.

A.3 Electronics

The wire signals are taken out through a 2200 pF blocking capacitor and fed through a pre-amp. The blocking capacitor and preamp assembly are mounted on a board that is attached to a stack by delrin standoffs which are screwed into the endplates. The board contains all the end electronics for the 4 chambers of a stack (Figure A.5). From there, the signals travel via 100 Ω shielded, twisted-pair cable to an isolation-transformer board attached to an Amplifier-Shaper-Discriminator (ASD) card. Both the preamp and the ASD card, which has been slightly modified for the upgrade, were designed for and used in other CDF tracking chambers [22]. From the ASD, differential ECL signals are sent to LeCroy 1879 TDCs, which feed the trigger electronics and the data acquisition system. The drift time measured by the TDCs gives the coordinate transverse to the beam direction only.

A.4 Chamber Construction

The CMP chambers were built at the University of Illinois over a period of a year and a half. Construction was done by several graduate students (myself included), a couple of postdocs, a professor, several technicians, and a large compliment of undergraduate students. For roughly six months during the construction period, chamber building took place for 16 hours a day with two shifts of people. Chamber construction consisted of four major steps: making the field-shaping pads, gluing the pads into the aluminum extrusions, gluing four chambers into a stack, and stringing wires through the chambers of a stack. The progress of chamber construction from day one is shown in Figure A.6.

The making of the field-shaping pads involved many steps. The pads are 14.5 cm wide sheets of copper-clad Glasteel, a fiberglass-like material. They were purposefully delivered in oversize rolls because the company that produced them couldn't maintain

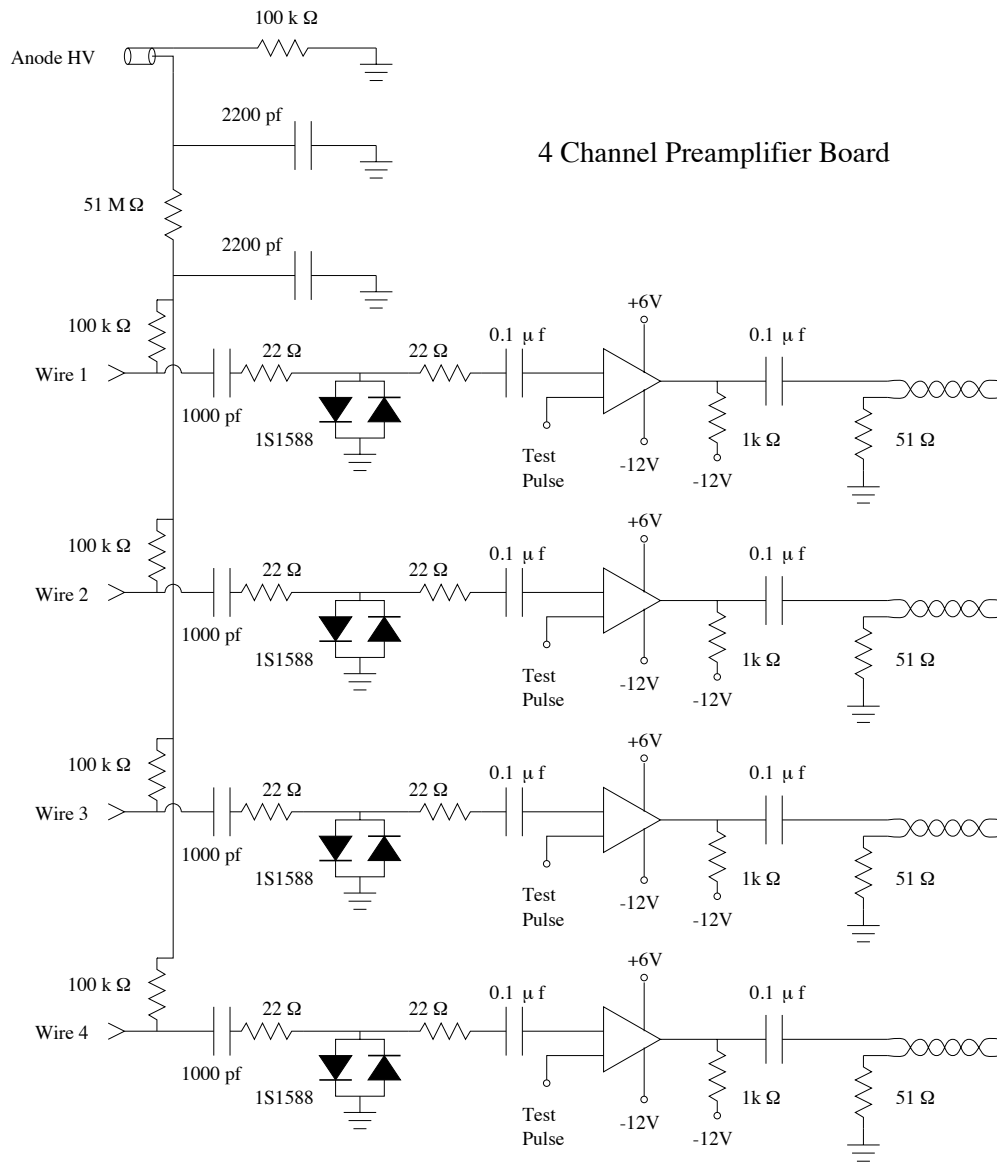


Figure A.5: The pre-amplifier electronics for a CMP chamber. This corresponds to four chambers (one stack).

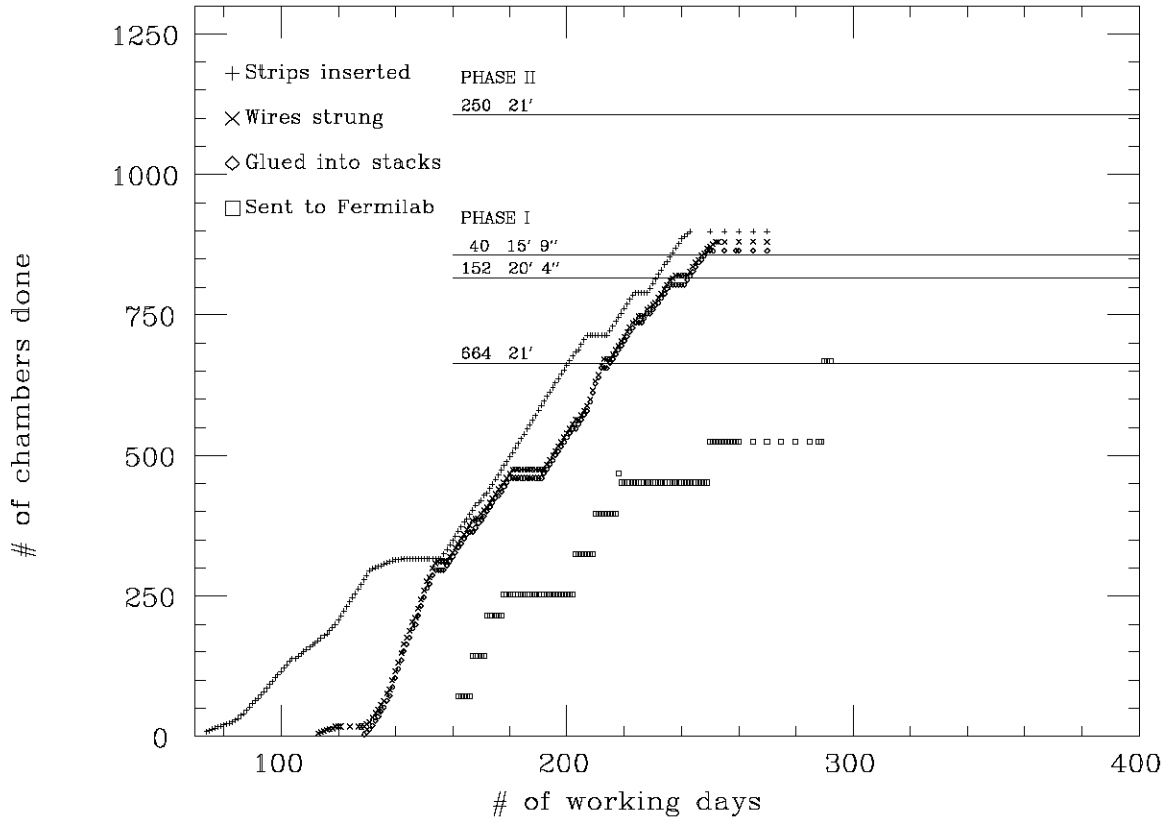


Figure A.6: Chamber production progress up through the first stage of construction.

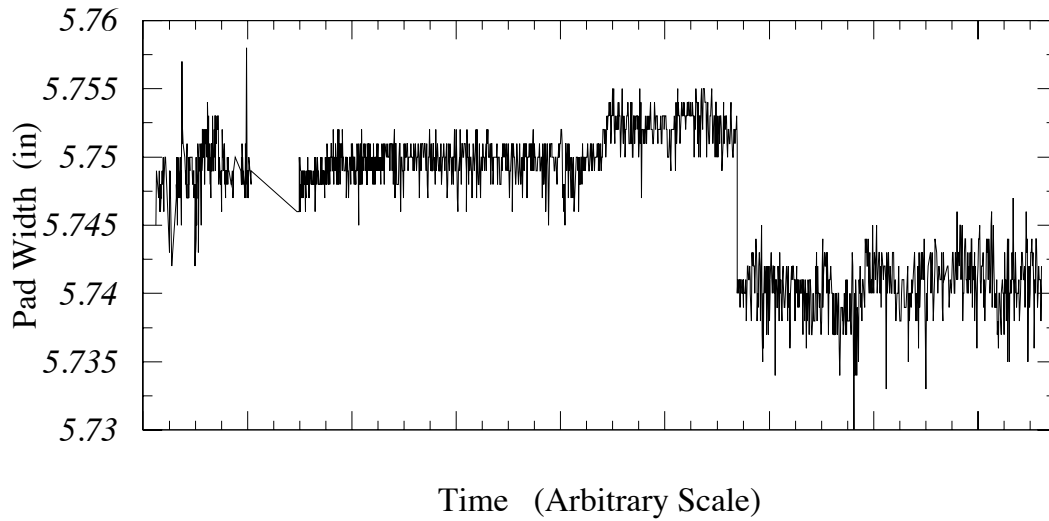


Figure A.7: The variation of the width of finished field-shaping pads. The step in the middle reflects the replacement of the cutting blades.

the required tolerance on the width. These rolls were cut to the correct width using a custom made, twin diamond-wheel saw complete with a vacuum housing to keep the amount of fiberglass dust to a minimum. The variation of the width of the finished pads is shown in Figure A.7. Once cut to width, individual high-voltage strips had to be formed on each pad. This was done using another custom-made device utilizing spring loaded Xacto blades to score the copper. The copper between the desired strips was peeled off the pad leaving the high-voltage strips behind.

After being high-voltage tested (see Figure A.8), the pads were glued into the aluminum chambers using a custom epoxy with a four hour cure time. These chambers were then glued into a stack of four chambers using a custom-made gluing jig. The jig used air cylinders, with a compressed air system, and 12 pairs of steel brackets, all mounted on an inch thick steel-plate support, to hold the chambers in the final shape while the glue dried for eight hours. The wire stringing took place after the stack had been made and typically took one to one-and-a-half hours to accomplish. Finally, the tensions of the wires were measured (Figure A.9) and the chambers were tested for

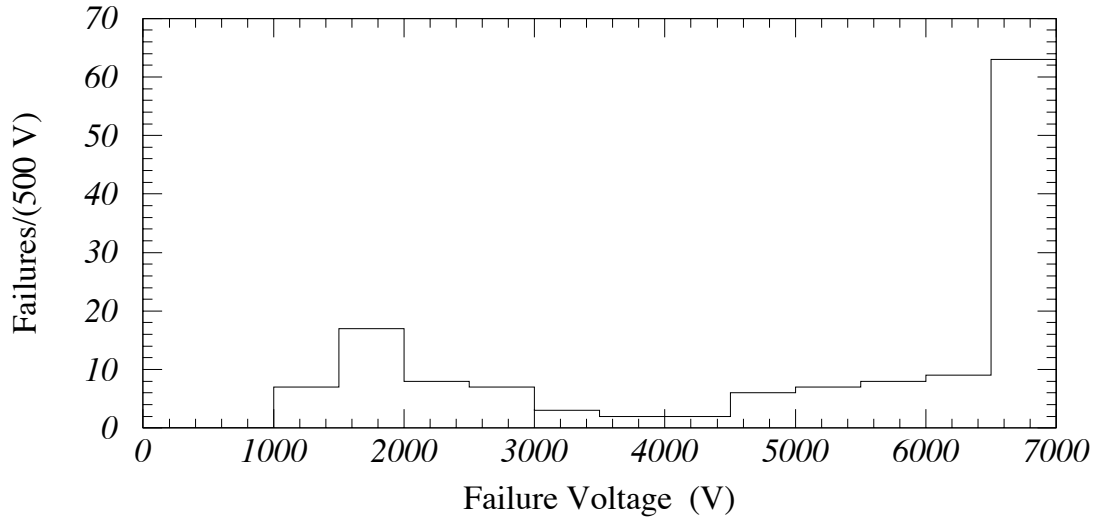


Figure A.8: Distribution of breakdown voltages for the field-shaping pads. The pads are tested by applying a voltage between the copper strips and an aluminum plate to which the pad is pressed against. The pad is designed to nominally hold $\sim 10,000$ Volts in this configuration. The peak at ~ 2000 V is due to flawed pads, while the peak at 7000 V is due in part to some amount of integration beyond the last bin. The pads

gas leaks and underwent performance studies using cosmic-ray muons. At the height of production, a rate of two stacks (8 chambers) a day was achieved. About 1000 chambers were built over the total construction period.

A.5 Testing and Performance

The chambers had both their gas leak-rates and their operating-voltage dark currents measured. The distributions of these are shown in Figure A.10. In the cosmic-ray test stand, both the efficiency and the position resolution of the chambers were measured. These were obtained by using three of the four chambers to determine the path of the cosmic-ray muon and extrapolating to the chamber under study. Plots of the

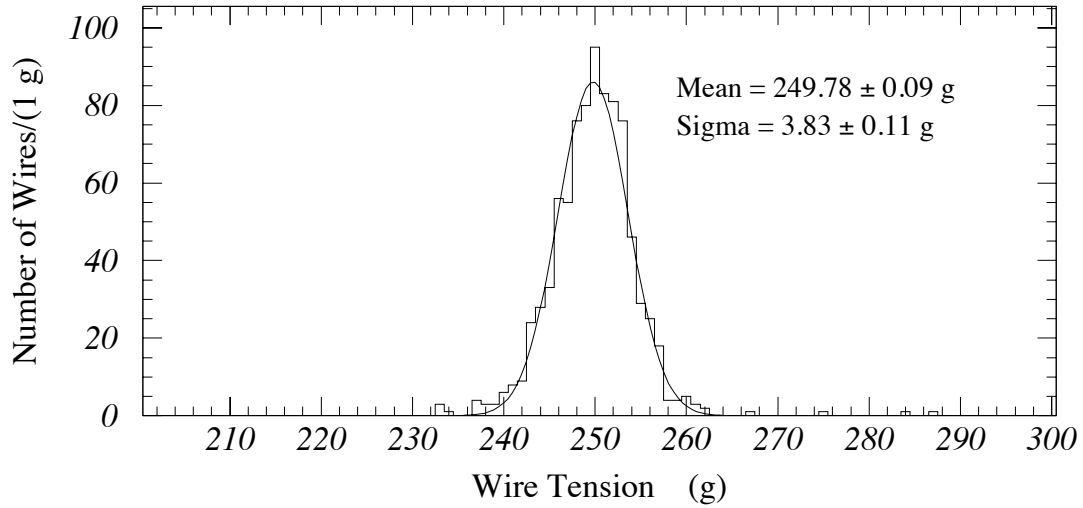


Figure A.9: The measured wire tensions in CMP chambers. The nominal tension was 250 g.

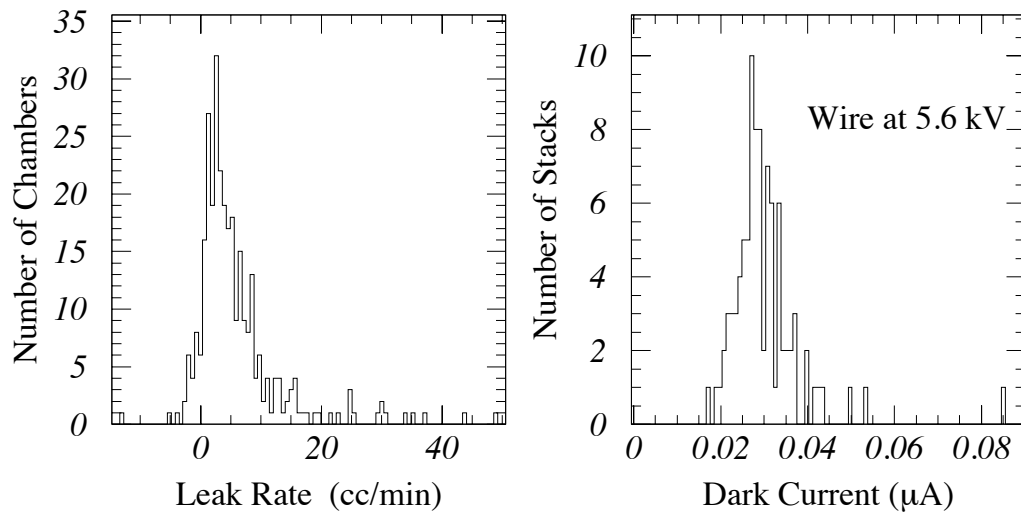


Figure A.10: Left: Gas leak rates at the test pressure of 2 PSI above atmosphere. The operating pressure is a small fraction of a PSI (~ 0.01 PSI). Right: Anode dark currents at a voltage of 5600 V (200 V above operating voltage).

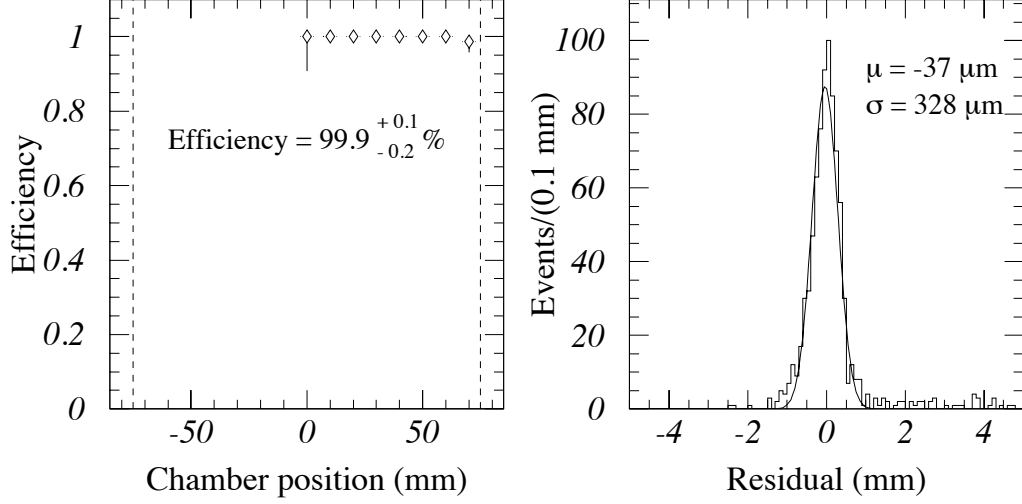


Figure A.11: Left: Efficiency of one half of a CMP chamber. Only half the chamber overlaps the rest of the stack. Right: Position resolution of a chamber.

efficiency and the resolution of a typical chamber are shown in Figure A.11. The position resolutions for all the constructed chambers are shown in Figure A.12. The drift velocity can be calculated from the drift times of three chambers, by using

$$v_{drift} = \frac{a}{bt_1 + ct_2 + dt_3}, \quad (\text{A.1})$$

where a , b , c , and d are constants that depend on the relative positions of the wires and t_1 , t_2 and t_3 are the 3 drift times. This distribution (Figure A.13) peaks where expected at $\sim 47 \text{ mm}/\mu\text{s}$.

The performance of the CMP during the data-taking period at Fermilab can be summed up in one plot. The CMP was designed to reduce the rate of fake triggers occurring in the CMU from hadronic punch-through. The punch-through is characterized by large amounts of energy in the same calorimeter tower traversed by the supposed muon. In Figure A.14 are plots of the hadronic energy in the tower traversed by the

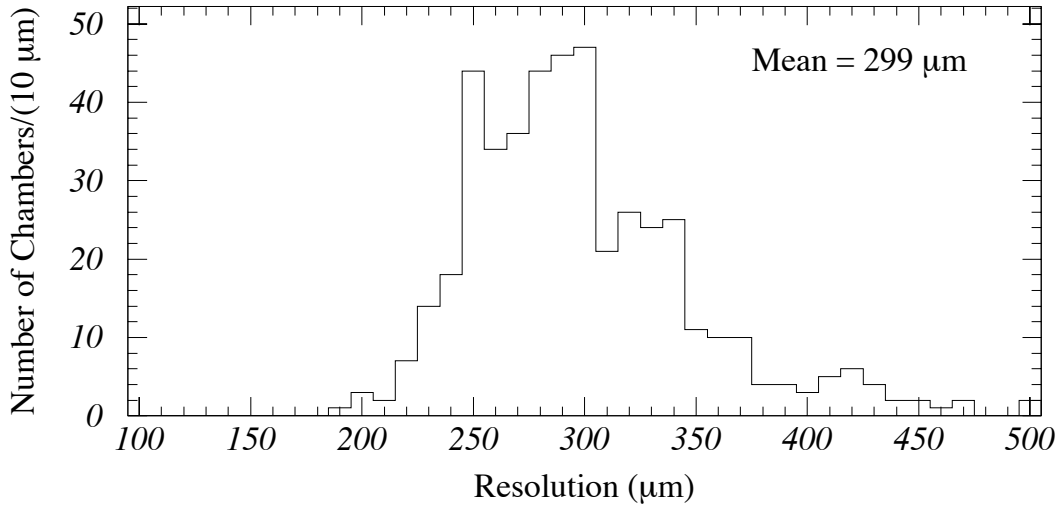


Figure A.12: The measured position resolutions for all the constructed chambers.

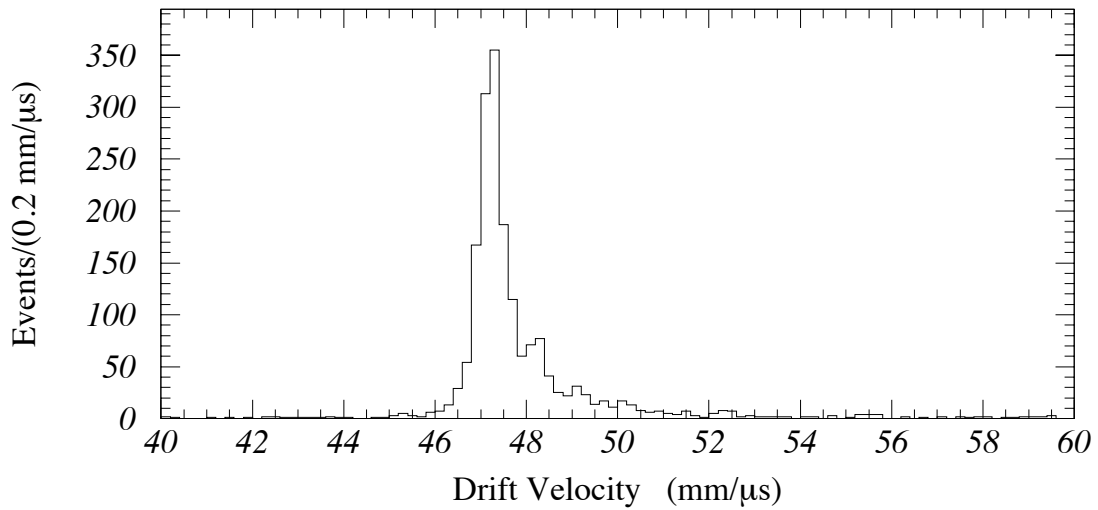


Figure A.13: The measured drift velocity for a typical chamber. The expected drift velocity is between 45 and 50 $\text{mm}/\mu\text{s}$.

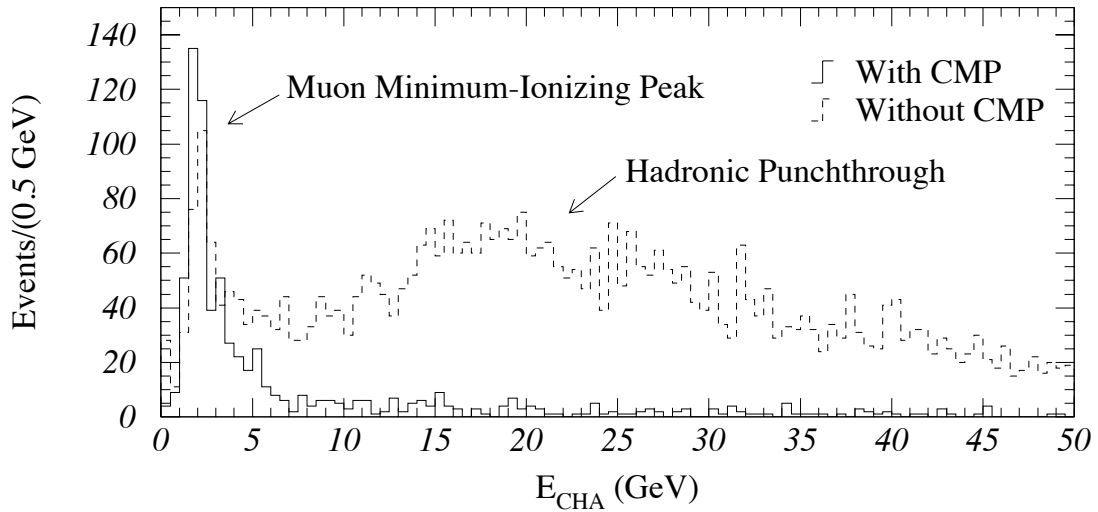


Figure A.14: The energy in the tower traversed by the muon for those with a CMP coincidence required (SOLID), and those without a CMP coincidence (DASHED). The later clearly shows the hadronic contamination (a real muon should peak at ~ 2 GeV).

“muon” for triggers requiring only CMU and for those requiring both CMU and CMP. The difference is striking.

If that is not enough to convince one of the CMP performance, one can also look at the position resolution from W data or the Δx match between the CTC and the CMP (Figure A.15). These plots confirm that the CMP is functioning as intended.

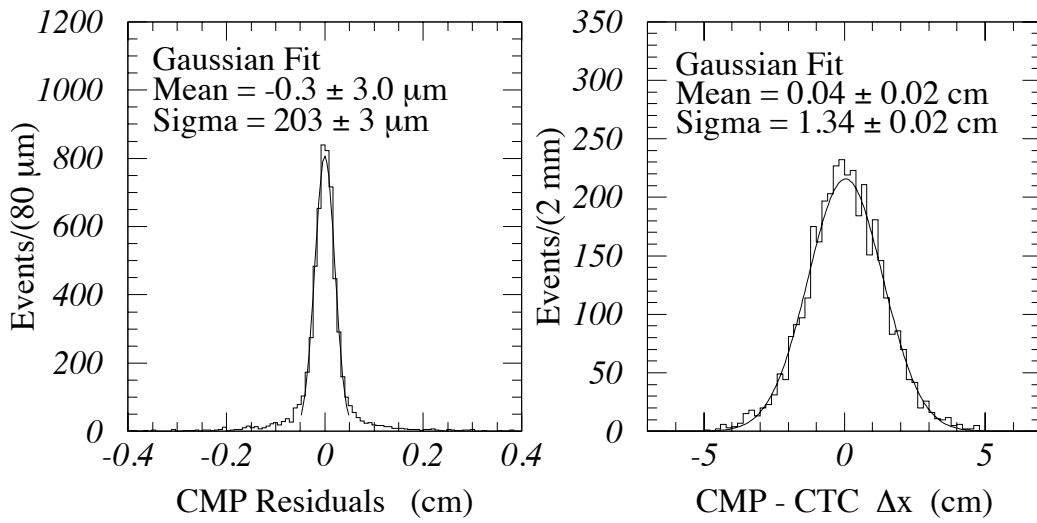


Figure A.15: Left: The position resolution of the CMP chambers as measured in W events. Right: The CMP-CTC matching distribution from the W mass sample. This width is consistent with that expected from multiple coulomb scattering.

Appendix B

Extrapolation from $M_{J/\psi}$ to M_W

In Section 5.3.1, all the contributions to the error on the J/ψ mass are discussed except curvature. In this appendix, the discussion of curvature error is combined with that of the extrapolation of the momentum scale by making use of the expansion

$$\Delta c = \sum_{i=0}^{\infty} c_i c^i, \quad (\text{B.1})$$

where Δc is the curvature error. Here the error in the curvature has been written in terms of the curvature, which lends itself well to an extrapolation in curvature space. Once the coefficients, c_i , have been determined, both the error and the extrapolation are completely specified. Since there is no practical way to determine an infinite number of coefficients, knowledge of the possible sources of curvature error is used to simplify the number to be determined.

B.1 Curvature Error

The curvature of a track is determined from drift distances and wire positions providing three possible sources of curvature error: error in the r position of a wire, error in the ϕ position of a wire, and error in the calculated drift distance. To quantify these, the

effect of each on a fitted track is investigated. As discussed in Section 5.1, a helical track is described by five parameters. The formula for the circular projection of a helix on the r - ϕ plane is

$$\phi = \phi_o + \arcsin\left(\frac{cr}{1+2cd_o} + \frac{d_o(1+cd_o)}{r(1+2cd_o)}\right) \quad (\text{B.2})$$

where c is the curvature¹, d_o is the impact parameter, ϕ_o is the initial azimuth of the track, and r is measured in centimeters. For particles with momenta above 1 GeV/ c ($c < 2 \times 10^{-3}$), and typical impact parameters ($d_o < 1\text{mm}$), the equation reduces to

$$\phi = \phi_o + cr \quad (\text{B.3})$$

which is linear in everything.

Error in ϕ Using Equation B.3, consider an error in the ϕ position of a wire.

$$c = \frac{\phi - \phi_o}{r} \quad \rightarrow \quad c' = \frac{(\phi + \Delta\phi) - \phi_o}{r} = c + \frac{\Delta\phi}{r} \quad (\text{B.4})$$

The resulting curvature offset, $\frac{\Delta\phi}{r}$, is what the layer alignment of Section 5.2.2 removes.

Error in r An error in the r position of a wire is equivalent to an error in ϕ except it varies with curvature. Again, using Equation B.3,

$$\Delta\phi = \frac{d\phi}{dr}\Delta r = c\Delta r \quad ; \quad c' = \frac{\phi + c\Delta r - \phi_o}{r} = c + c\frac{\Delta r}{r}. \quad (\text{B.5})$$

This curvature dependent error, $c\frac{\Delta r}{r}$, is absorbed into the momentum scale normalization.

¹Recall that curvature is a signed quantity and has the same sign as the charge of the particle.

Error in Drift Distance Errors in the drift model that are not curvature-dependent look like the previously discussed ϕ position errors, and are removed by the wire alignment. The only curvature dependent part of the drift model is the correction for aspect angle, i.e. the angle at which the particle enters a given wire layer with respect to the normal. For zero curvature, the aspect angle is zero and there is no correction. Since the tracks of concern here have small aspect angles ($< 10^\circ$), and since the aspect angle correction is explicitly calibrated, the error from this effect is expected to be small; but, nonetheless, some curvature dependence will be allowed.

Comparing Equation B.1 with the above results indicates that only the lowest-order terms should be relevant. It is also important to note that for small c , i.e. large p_T , there is no $1/c$ behavior in any of the above contributions to curvature error.

B.2 Curvature Expansion

The extrapolation by inverting invariant mass (Equation 5.4),

$$\frac{1}{M^2} = K c_+ c_- F(\theta_+, \theta_-, \Delta\phi) \quad (\text{B.6})$$

where K includes the conversion from momentum to curvature and F contains all the angular dependences. Writing the error in $1/M^2$ in terms of the curvature error gives

$$M^2 \Delta \left(\frac{1}{M^2} \right) = \frac{\Delta c_+}{c_+} + \frac{\Delta c_-}{c_-} + \frac{\Delta c_+ \Delta c_-}{c_+ c_-}. \quad (\text{B.7})$$

Expanding Δc using Equation B.1 and dropping terms above ϵ_3 in the first part and above ϵ_1 in the product leaves

$$\frac{2\Delta M}{M} = \epsilon_0 \left(\frac{1}{c_+} + \frac{1}{c_-} \right) + 2\epsilon_1 + \epsilon_2 (c_+ + c_-) + \epsilon_3 (c_+^2 + c_-^2) + \frac{c_0^2}{c_+ c_-}$$

$$+\epsilon_0\epsilon_1\left(\frac{1}{c_+} + \frac{1}{c_-}\right) + \epsilon_1^2 \quad (\text{B.8})$$

Averaging over all events gives

$$\left\langle\frac{\Delta M}{M}\right\rangle = \epsilon_0\left\langle\frac{1}{c}\right\rangle + \epsilon_1 + \epsilon_2\langle c\rangle + \epsilon_3\langle c^2\rangle - \frac{1}{2}\epsilon_0^2\left\langle\frac{1}{c^2}\right\rangle + \epsilon_0\epsilon_1\left\langle\frac{1}{c}\right\rangle + \frac{1}{2}\epsilon_1^2 \quad (\text{B.9})$$

where $\langle \rangle$ indicate an average. As shown in Section 5.2.2.3, the residual misalignment of the CTC results in a curvature offset, ϵ_0 , of $< 10^{-7}$. Combining this with the mean values of $1/c$ and $1/c^2$ leads to an error on the mass of $< 50 \text{ keV}/c^2$. The first-order coefficient, ϵ_1 , is the scale term and is obtained from the final J/ψ mass uncertainty. An upper limit on ϵ_2 is set from the width of the J/ψ peak. Conservatively assuming that the entire width of $\sim 15 \text{ MeV}/c^2$ is from this term², then $\epsilon_2 < 20$ (given that the RMS width of $c_+ + c_-$ is $\sim 4 \times 10^{-4}$) and again the error on the mass is less than $< 80 \text{ keV}/c^2$. Table B.1 lists the evaluations of the terms in Equation B.9 for both the J/ψ and W . The remaining coefficient, ϵ_3 , is the term from which the nonlinearity of the momentum measurement will be extracted. Recall that systematic errors on the J/ψ were $> 0.1 \text{ MeV}/c^2$. Looking at Table B.1, all but the scale and nonlinearity terms can safely be ignored. Ignoring all but these, Equation B.9 reduces to

$$\left\langle\frac{\Delta M}{M}\right\rangle = \epsilon_1 + \epsilon_3\langle c^2\rangle, \quad (\text{B.10})$$

and hence a nonlinearity should manifest itself as a linear variation of the J/ψ mass with c^2 . For convenience, the mass variation is written in terms of $1/p_T^2$

$$\frac{\Delta M}{M} = \epsilon_1 + \epsilon_3' \frac{1}{p_T^2}. \quad (\text{B.11})$$

²The width of the J/ψ is due in part to resolutions. Assuming all of it is from a systematic curvature error is clearly an overestimate.

		ϵ_0	ϵ_1	ϵ_2	ϵ_3
		$< 10^{-7}$	ϵ_1	< 20	ϵ_3
	$\langle \frac{1}{c} \rangle$	$\langle c \rangle$	$\langle c^2 \rangle$	$\langle \frac{1}{c^2} \rangle$	
J/ψ	1.1	1.3×10^{-6}	1.3×10^{-6}	7.0×10^6	
W	130	3×10^{-7}	3×10^{-9}	3×10^8	

	$J/\psi \Delta M/M$	$J/\psi \Delta M(\text{MeV}/c^2)$	$W \Delta M/M$	$W \Delta M(\text{MeV}/c^2)$
$\epsilon_0 \langle \frac{1}{c} \rangle$	1.1×10^{-7}	0.0003	1.3×10^{-5}	1.0
ϵ_1	ϵ_1	$3100.0\epsilon_1$	ϵ_1	$80000.0\epsilon_1$
$\epsilon_2 \langle c \rangle$	2.6×10^{-5}	0.08	6×10^{-6}	0.5
$\epsilon_3 \langle c^2 \rangle$	$\epsilon_3 \langle c^2 \rangle$	$3100.0\epsilon_3 \langle c^2 \rangle$	$\epsilon_3 \langle c^2 \rangle$	$80000.0\epsilon_3 \langle c^2 \rangle$
$\frac{1}{2}\epsilon_0^2 \langle \frac{1}{c^2} \rangle$	3.5×10^{-8}	0.0001	1.5×10^{-6}	0.1
$\epsilon_0\epsilon_1 \langle \frac{1}{c} \rangle$	$\epsilon_1(1.1 \times 10^{-7})$	$0.0003\epsilon_1$	$\epsilon_1(1.3 \times 10^{-5})$	$1.0\epsilon_1$
$\frac{1}{2}\epsilon_1^2$	$\frac{1}{2}\epsilon_1^2$	$1550.0\epsilon_1^2$	$\frac{1}{2}\epsilon_1^2$	$40000.0\epsilon_1^2$

Table B.1: Table of curvature error terms and their contributions the error on the J/ψ and W masses. Top: The values of the four lowest-order coefficients. The value of ϵ_1 will be obtained from the momentum scale normalization and is expected to be small ($< 10^{-3}$). The value of ϵ_3 is extracted from this exercise. Middle: The average values of curvature terms in the expansion for both the J/ψ and W . Bottom: Term-by-term evaluation of Equation B.9 both in fractional mass error and in MeV/c^2 for the J/ψ and W .

Bibliography

- [1] S. Glashow, Partial-Symmetries of Weak Interactions, Nucl. Phys. **22**, 579 (1961); S. Weinberg, A Model of Leptons, Phys. Rev. Lett. **19**, 1264 (1967); A. Salam, *Elementary Particle Theory*, page 367, Almqvist & Wiksell, Sweden, 1968.
- [2] P.W. Higgs, Broken Symmetries and the Masses of Gauge Bosons, Phys. Rev. Lett. **13**, 508 (1964).
- [3] G. Arnison *et al.* (UA1 Collaboration), Phys. Lett. B **122**, 103 (1983).
- [4] M. Banner *et al.* (UA2 Collaboration), Phys. Lett. B **122**, 476 (1983).
- [5] G. Arnison *et al.* (UA1 Collaboration), Phys. Lett. B **134**, 469 (1984).
- [6] G. Arnison *et al.* (UA1 Collaboration), Europhys. Lett. **1**, 327 (1986).
- [7] R. Ansari *et al.* (UA2 Collaboration), Phys. Lett. B **186**, 440 (1987).
- [8] C. Albajar *et al.* (UA1 Collaboration), Z. Phys. C **44**, 15 (1989).
- [9] F. Abe *et al.* (CDF Collaboration), Phys. Rev. Lett. **62**, 1005 (1989).
- [10] J. Alitti *et al.* (UA2 Collaboration), Phys. Lett. B **241**, 150 (1990).
- [11] F. Abe *et al.* (CDF Collaboration), Phys. Rev. Lett. **65**, 2243 (1990); F. Abe *et al.* (CDF Collaboration), Phys. Rev. D **43**, 2070 (1991).
- [12] J. Alitti *et al.* (UA2 Collaboration), Phys. Lett. B **276**, 354 (1992).

- [13] A. Sirlin, Radiative Corrections in the $SU(2) \times U(1)$ Theory: A Simple Renormalization Framework. *Phys. Rev. D* **22**, 971 (1980).
- [14] The theory curves are calculated using a FORTRAN program from F. Halzen and B.A. Kniehl (private communication), described in *Nucl. Phys.* **B353**, 567 (1991). The M_W - M_{top} relation is calculated in the modified resummation scheme, and includes the $\mathcal{O}(\alpha)$, $\mathcal{O}(\alpha\alpha_s)$ and $\mathcal{O}(\alpha^2)$ contributions to Δr . The program has been modified to include the effect of higher-order M_{top} -dependent QCD corrections to $\Delta\rho$ (See e.g. B.H. Smith and M.B. Voloshin, Minnesota preprint UMN-TH-1241/94 (HEP-PH9401357) and also A. Sirlin, HEP-PH-9403282). The values used to calculate the curves are $\alpha_{em} = 1/137.0359895 \pm 0.0000061$, $G_F = 1.16639 \pm 0.00002 \times 10^{-5} \text{ GeV}^{-2}$, $M_Z = 91.187 \pm 0.007 \text{ GeV}/c^2$, $\alpha_s(M_Z^2) = 0.117 \pm 0.005$, and $\Delta\alpha_{had}(M_Z^2) = 0.02666 \pm 0.00075$ (See Ref. [15] below). For additional discussions, see e.g. S. Franchiotti, B.A. Kniehl and A. Sirlin, *Phys. Rev. D* **48**, 307 (1993) and references therein.
- [15] M. L. Swartz, SLAC-PUB-6710, Nov. 1994. See also A. Martin and D. Zeppenfeld, UW preprint, MAD-PII-855, Nov. 1994.
- [16] For recent reviews, see W. Hollik and W. Marciano, in *Precision Tests of the Standard Electroweak Model*, ed. by P. Langacker (World Scientific, Singapore, 1994), and B. A. Kniehl, KEK preprint KEK-TII-412, Sept. 1994, submitted to *Int. J. Mod. Phys. A*.
- [17] F. A. Berends, *Z Physics at LEP 1*, CERN Report 89-08, Volume 1, (1989).
- [18] V. Barger and A.D. Martin, Perpendicular $\epsilon\nu$ Mass From W Decay, *Z. Phys. C* **21**, 99 (1983).
- [19] F. Abe *et al.* (CDF collaboration), The CDF Detector: An Overview, *Nucl. Instrum. Methods Phys. Res. A* **271**, 387 (1988).

- [20] D. Amidei *et al.*, The Silicon Vertex Detector of the Collider Detector at Fermilab, Nucl. Instrum. Methods Phys. Res. A **350**, 73 (1994). For a related article see D. Amidei *et al.*, Nucl. Instrum. Methods Phys. Res. A **342**, 251 (1994).
- [21] F. Snider *et al.*, The CDF Vertex Time Projection Chamber System. Nucl. Instrum. Methods Phys. Res. A **268**, 75 (1988). This is the reference for the previous generation of the device. The replacement for the 1992-93 data-taking period has more modules, each with a shorter drift length, but is otherwise similar.
- [22] F. Bedeschi *et al.*, Design and Construction of the CDF Central Tracking Chamber, Nucl. Instrum. Methods Phys. Res. A **268**, 50 (1988).
- [23] L. Balka *et al.*, The CDF Central Electromagnetic Calorimeter, Nucl. Instrum. Methods Phys. Res. A **267**, 272 (1988). For related material see S. R. Hahn *et al.*, Nucl. Instrum. Methods Phys. Res. A **267**, 351 (1988); K. Yasuoka *et al.*, Nucl. Instrum. Methods Phys. Res. A **267**, 315 (1988); R. G. Wagner *et al.*, Nucl. Instrum. Methods Phys. Res. A **267**, 330 (1988); T. Devlin *et al.*, Nucl. Instrum. Methods Phys. Res. A **267**, 24 (1988).
- [24] S. Bertolucci *et al.*, The CDF Central and Endwall Hadron Calorimeter, Nucl. Instrum. Methods Phys. Res. A **267**, 301 (1988).
- [25] Y. Fukui *et al.*, Nucl. Instrum. Methods Phys. Res. A **267**, 280 (1988); W. C. Carithers *et al.*, *Proceedings of the Gas Sampling Calorimetry Workshop II*, Batavia, Illinois, 54 (1985); S. Cihangir *et al.*, Nucl. Instrum. Methods Phys. Res. A **267**, 249 (1988); G. Brandenburg *et al.*, Nucl. Instrum. Methods Phys. Res. A **267**, 257 (1988). The \vec{u} calculation uses the calorimeters inside the range $|\eta| < 3.6$.
- [26] F. Abe *et al.* (CDF Collaboration), Measurement of the W Boson Mass, to be submitted to Phys. Rev. D; F. Abe *et al.* (CDF Collaboration), to be submitted to Phys. Rev. Lett.

- [27] D. P. Saltzberg, Ph. D. dissertation, University of Chicago, 1994.
- [28] G. Ascoli *et al.*, CDF Central Muon Detector, Nucl. Instrum. Methods Phys. Res. A **268**, 33 (1988). For a related article see G. Ascoli *et al.*, Nucl. Instrum. Methods Phys. Res. A **268**, 41 (1988).
- [29] For discussions of the CMP, see Appendix A in this thesis; M. Vondracek, Ph. D. dissertation, University of Illinois, 1995; A. J. Martin, Ph. D. dissertation, University of Illinois, 1995. Also look for an article to be submitted to Nucl. Instrum. Methods Phys. Res. A
- [30] D. Amidei *et al.*, A Two Level Fastbus Based Trigger System for CDF, Nucl. Instrum. Methods Phys. Res. A **269**, 51 (1988).
- [31] T. Carroll *et al.*, Nucl. Instrum. Methods Phys. Res. A **263**, 199 (1988).
- [32] G. Ascoli *et al.*, CDF Central Muon Level-1 Trigger Electronics, Nucl. Instrum. Methods Phys. Res. A **269**, 63 (1988). This is the reference for the previous generation of the trigger before the existence of the CMP. For a description of the level-1 trigger for the 1992-1993 data-taking period, see A. J. Martin, Ph. D. dissertation, University of Illinois, 1995, and M. Krasberg, Ph. D. dissertation, University of Michigan, 1995.
- [33] G. W. Foster *et al.*, A Fast Hardware Track-Finder for the CDF Central Tracking Chamber. Nucl. Instrum. Methods Phys. Res. A **269**, 93 (1988).
- [34] F. Sauli, Principles of Operation of Multiwire Proportional and Drift Chambers, CERN Report 77-09 (1977), also reprinted in *Experimental Techniques in High Energy Physics*, page 79, Addison-Wesley, 1987. This reference contains a brief description of energy loss by ionization plus related references.
- [35] M. Aguilar-Benitez *et al.* (PDG), *Review of Particle Properties* from Phys. Rev. D **45**, (1992); Phys. Rev. D **50**, (1994). The W mass analysis was completed

before the 1994 edition of this review, and so used the 1992 numbers; the numbers in the text have been updated to the 1994 values where appropriate. The differences for the numbers used in this thesis are completely insignificant.

- [36] C. Newman-Holmes, E. E. Schmidt, and R. Yamada, Nucl. Instrum. Methods Phys. Res. A **274**, 443 (1989).
- [37] F. A. Berends and R. Kleiss, Hard Photon Effects in W^\pm and Z^0 Decay, Z. Phys. C **27**, 365 (1985).
- [38] R. G. Wagner, Comput. Phys. Commun. **70**, 15 (1992).
- [39] U. Baur and E. L. Berger, Phys. Rev. D **41**, 1476 (1990).
- [40] For a description of the MRS D'_0 , D'_- and II global fits, see A.D. Martin, R.G. Roberts and W.J. Stirling, RAL-92-099 (1993). For a description of the CTEQ global fits, see J. Botts *et al.*, Phys. Lett. B **304**, 159 (1993). For a description of the GRV set, see Z. Phys. C **53**, 127 (1992). For a description of the MT sets, see J. Morfin and W.K. Tung, Z. Phys. C **52**, 13 (1991). The MRS A set uses the CDF charge asymmetry measurement in the fit; all the others are evaluated independently of the CDF measurement.
- [41] F. Abe *et al.* (CDF Collaboration), Phys. Rev. Lett. **66**, 2951 (1991).
- [42] P. B. Arnold and R. P. Kauffman, Nucl. Phys. **B349**, 381 (1991). Generated with $\Lambda_{QCD} = 300$ MeV, $S_{np} = 1.36$ GeV $^2b^2$, and $b_{\max} = (2 \text{ GeV})^{-1}$.
- [43] G. Altarelli, R. K. Ellis, M. Greco, and G. Martinelli, Nucl. Phys. **B246**, 12 (1984).
- [44] F. Abe *et al.* (CDF Collaboration), Phys. Rev. Lett. **67**, 2937 (1991).
- [45] M. H. Reno, University of Iowa preprint UIOWA-94-01 (1994).
- [46] G. Marchesini and B. Webber, Nucl. Phys. **B310**, 461 (1988).

- [47] The maximum likelihood estimation method is documented in many places. See for instance L. Lyons, *Statistics for Nuclear and Particle Physicists*, Cambridge University Press, 1986; W. T. Eadie, D. Drijard, F. E. James, M. Roos, and B. Sadoulet, *Statistical Methods in Experimental Physics*, North-Holland, 1971.
- [48] F. James and M. Roos. *Function Minimization and Error Analysis*, 1983. CERN Program Library Documentation.
- [49] F. Abe *et al.* (CDF Collaboration), Phys. Rev. Lett. **73**, 220 (1994).
- [50] F. Abe *et al.* (CDF Collaboration), submitted to Phys. Rev. Lett. (1994).
- [51] J. Rosner, M. Worah, and T. Takeuchi, Phys. Rev. D **45**, 1363 (1994).
- [52] G. Bardin *et al.*, Phys. Lett. B **137**, 135 (1984).
- [53] F. Abe *et al.* (CDF Collaboration), Phys. Rev. Lett. **74**, 850 (1995).
The forward/backward charge asymmetry in W decays is defined as: $A(\eta) = \frac{(d\sigma^+/d\eta)-(d\sigma^-/d\eta)}{(d\sigma^+/d\eta)+(d\sigma^-/d\eta)}$, where $d\sigma^\pm/d\eta$ is the cross section for W^\pm decays as a function of lepton pseudorapidity, η .
- [54] C. Arroyo *et al.* (CCFR Collaboration), Phys. Rev. Lett. **72**, 3452 (1994).
- [55] A. D. Martin and W. J. Stirling, Phys. Lett. B **237**, 551 (1990).
- [56] E. L. Berger, F. Halzen, C. S. Kim, and S. Willenbrock, Phys. Rev. D **40**, 83 (1989).
- [57] P. Chiappetta and M. Le Bellac, Z. Phys. C **32**, 521 (1986).
- [58] The LEP Electroweak Working Group, CERN preprint CERN/PPE/94-187, Nov. 1994 (unpublished).
- [59] K. Abe *et al.* (SLD Collaboration), Phys. Rev. Lett. **73**, 25 (1994). The W mass prediction is from M. Swartz, private communication, April 25, 1994.

- [60] F. Abe *et al.*, Fermilab preprint FERMILAB-PUB-95/022-E, submitted to Phys. Rev. Lett.

Vita

Randy Michael Keup [REDACTED]. At the tender age of two, he assisted his parents in building their house. Sixteen years later, it came time to go to college. Having an interest in astronomy, Randy chose to attend the University of Wisconsin – Oshkosh, despite the fact that Oshkosh had no astronomy major. He decided he would major in physics and then go to graduate school in astronomy. All this changed when he discovered computers. Astronomy was out and in its place was an instrumentation degree in physics coupled with a minor in computer science. After half a dozen programming courses, it became obvious to Randy that the sum total of computer science is sorting and searching. Consequently, the minor switched to math, and to conserve momentum, the physics degree flopped back to the professional track in preparation for graduate study in physics. Upon receiving his degree in 1987, Randy headed south to study particles in Urbana. Of course Randy knew nothing about experimental particle physics and thus was the ideal candidate when he signed on with Lee Holloway and the CDF contingent. Immediately upon signing, Randy was drafted by an expansion team headed by Tony Liss who immediately set him to work designing muon drift chambers; and drift chambers is what he did for the next four years until lo and behold a W popped out of the CDF detector. Randy wasted no time (well, only enough to get married) in measuring the mass of it and threw together a thesis in time to complete the 8-year plan.